

Janne P. Aikio

FREQUENCY DOMAIN
MODEL FITTING AND
VOLTERRA ANALYSIS
IMPLEMENTED ON TOP OF
HARMONIC BALANCE
SIMULATION

FACULTY OF TECHNOLOGY,
DEPARTMENT OF ELECTRICAL AND INFORMATION ENGINEERING,
UNIVERSITY OF OULU



ACTA UNIVERSITATIS OULUENSIS
C Technica 272

JANNE P. AIKIO

**FREQUENCY DOMAIN MODEL
FITTING AND VOLTERRA ANALYSIS
IMPLEMENTED ON TOP OF
HARMONIC BALANCE SIMULATION**

Academic dissertation to be presented, with the assent of
the Faculty of Technology of the University of Oulu, for
public defence in Raahensali (Auditorium L10), Linnanmaa,
on May 4th, 2007, at 12 noon

OULUN YLIOPISTO, OULU 2007

Copyright © 2007
Acta Univ. Oul. C 272, 2007

Supervised by
Professor Timo Rahkonen

Reviewed by
Professor José Carlos Pedro
Ph.D. Stephen A. Maas

ISBN 978-951-42-8419-9 (Paperback)
ISBN 978-951-42-8420-5 (PDF)
<http://herkules oulu.fi/isbn9789514284205/>
ISSN 0355-3213 (Printed)
ISSN 1796-2226 (Online)
<http://herkules oulu.fi/issn03553213/>

Cover design
Raimo Ahonen

OULU UNIVERSITY PRESS
OULU 2007

Aikio, Janne P., Frequency domain model fitting and Volterra analysis implemented on top of harmonic balance simulation

Faculty of Technology, University of Oulu, P.O.Box 4000, FI-90014 University of Oulu, Finland,
Department of Electrical and Information Engineering, University of Oulu, P.O.Box 4500, FI-90014 University of Oulu, Finland

Acta Univ. Oul. C 272, 2007

Oulu, Finland

Abstract

The modern wireless communication techniques are aiming on increasing bandwidth and the number of carriers for higher data rate. This sets challenging linearity requirements for RF power amplifiers (PAs). Unfortunately, high linearity can only be obtained at the cost of efficiency. In order to improve the performance of the PA, in-depth understanding of nonlinear behaviour is mandatory. This calls for techniques that can give componentwise information of the causes of the distortion. The aim of this thesis is to develop a technique that can provide such information.

This thesis proposes a detailed distortion analysis technique that is based on frequency domain fitting of polynomial models. Simulated large-signal spectra are used for fitting as these contain the necessary information about the large-signal bias point and amplitude range. Moreover, in the frequency domain the delays are easy to compensate, and detailed analysis to any fitted tone can be performed. The fitting procedure as such is simple but becomes difficult in multi-dimensional nonlinearities if the controlling voltages correlate strongly. In this thesis the solvability and reliability of the fitting procedure is increased by numerical operations, model-degree reduction and by using different excitations.

A simplified Volterra method is used to calculate the distortion contributions by using the fitted model. The overall distortion is analysed by calculating the voltage response of the contributions of each nonlinearity to the terminal nodes of the device by the use of linear transfer functions of the circuit. The componentwise analysis is performed by phasor presentation enabling the cancelling mechanisms to be seen.

The proposed technique is implemented on top of harmonic balance simulation in an APLAC circuit simulator in which extensive distortion simulations are performed. The technique relies on the existing device model and thus the fitted model can be only as accurate as the particular simulation model. However, two different RF PAs are analysed that show a good agreement between measurements and simulations.

The proposed technique is verified with several test cases including amplitude dependent amplitude and phase distortion, intermodulation distortion sweet spots, bandwidth dependent memory effects and impedance optimization. The main finding of the detailed analysis is that the distortion is a result of several cancelling mechanisms. In general, cubic nonlinearity of transconductance is dominating the in-band distortion but is cancelled by the 2nd-degree nonlinearity that is mixed to the fundamental band from envelope and 2nd harmonic bands that is usually the main cause of memory effects.

Keywords: distortion analysis, memory effects, nonlinear modelling, polynomial device model, RF power amplifiers, Volterra analysis

Acknowledgements

This thesis is based on research work carried out at the Electronics Laboratory of the Department of Electrical and Information Engineering, University of Oulu during the years 2003-2006.

I wish to express my deepest gratitude to Professor Timo Rahkonen, who supervised this work. His encouragement and guidance in the difficult times has been extraordinary. I wish to thank also Dr. Joel Vuolevi, who introduced and inspired me to become a researcher in the first place. His contribution and support towards this work has been significant. I am also grateful for the support and assistance I received from my colleagues Markku Kyllönen and Antti Heiskanen as well as Taisto Tinttunen and Dr. Jaakko Juntunen from AWR-APLAC corp.

I would also like to thank all my colleagues in the Electronics Laboratory for pleasant and inspiring working atmosphere. My former colleagues in Elektrobit Ltd. deserve a thankful notion.

I wish to thank Professor Jose Carlos Pedro and Dr. Steve Maas for reviewing this thesis. It is a great honour to have my thesis reviewed by such experienced researchers in this field. I would also like to thank Mr. Janne Rissanen for revising the English of this thesis.

This research was supported financially by Infotech Oulu Graduate School, University of Oulu, Finnish Funding Agency for Technology and Innovation (TEKES), Academy of Finland, AWR-APLAC corp., National Semiconductor Ltd., Elektrobit Ltd., ESJU Ltd. and divisions of Nokia Group. Financial support has also been received from the following foundations: Tekniikan Edistämissäätiö (TES), Tauno Tönningin Säätiö, Nokia Oyj:n Säätiö and Seppo Säynäjäkankaan Tiedesäätiö. All of these partners and foundations are gratefully acknowledged.

I would like to thank my parents and relatives as well as my friends, especially, Matti Passoja and Petri Koivukangas for their support. Finally, I would like to express my warmest thanks to my family, Hannakaisa, Miska and Heta for their patience and support.

Oulu, March 2007

Janne Aikio

List of symbols and abbreviations

1-D	1-dimensional
2-D	2-dimensional
1T	1-tone signal
2T	2-tone signal
3T	3-tone signal
3GPP	The 3rd Generation Partnership Project
AC	alternating current
ADS	advanced design system
AM-AM	amplitude dependent amplitude distortion
AM-PM	amplitude dependent phase distortion
BJT	bipolar junction transistor
BSIM	Berkeley's short-channel IGFET model
CW	continuous wave, nonpulsed sinusoidal signal
DC	direct current
ES	envelope simulation technique
FET	field effect transistor
FU	fundamental tones, fundamental band
FUH	higher fundamental tone = f_2
FUL	lower fundamental tone = f_1
EER	envelope elimination and restoration
HB	harmonic balance
HBT	heterojunction bipolar transistor
HD	harmonic distortion
HN	Nth harmonic frequency band
IC	integrated circuit
InGaP	indium gallium phosphide
IM	intermodulation
IM3	3rd-order intermodulation distortion
IM3L	3rd-order intermodulation distortion at $(2 \cdot f_1 - f_2)$ (below fundamental tones)
IM3H	3rd-order intermodulation distortion at $(2 \cdot f_2 - f_1)$ (above fundamental tones)

IM3R	3rd-order intermodulation product relative to the fundamental tone
IM5	5th-order intermodulation distortion
IMD	intermodulation distortion
LDMOS	laterally diffused metal oxide semiconductor
LSE	least square error
MESFET	metal-semiconductor field effect transistor
MET	Motorola's electro-thermal model
NWA	Network analyser
MOSFET	metal oxide semiconductor field effect transistor
OFDM	orthogonal frequency division multiplexing
PA	power amplifier
PAR	peak to average ratio
pdf	amplitude power density function
PWC	printed wired circuit
RF	radio frequency
SB	spectral balance
VBIC	vertical bipolar intercompany model
VCCS	voltage controlled current source
VNA	vector network analyser
VSA	vector signal analyser
WCDMA	wideband code-division multiple access
QAM	quadrature amplitude modulation

A	Amplitude of the input signal [V]
a_n	nth-order nonlinearity coefficient of the Taylor series
C_{BE}	base to emitter capacitance
C_{DS}	drain to source capacitance
C_{GS}	gate to source capacitance
C_{GD}	gate to drain capacitance
CTH	thermal capacitance
f	frequency
f_0	centre frequency
f_1	lower fundamental frequency = FUL
f_2	higher fundamental frequency = FUH
f_{IM3}	IM3 frequency
f_{H2}	second harmonic frequency
f_{ENV}	envelope frequency
G-V	conductance-voltage characteristics
g_m	transconductance
g_o	output conductance
I	current vector
I(f)	current spectrum
I-V	current-voltage characteristics
I_C	collector current
I_{CQ}	collector bias current
I_{DS}	drain to source current

I_{DQ}	drain bias current
K	coefficient vector
K_n	nth-degree coefficient of the polynomial model
M	Vandermonde matrix, fitting matrix
P_{DISS}	dissipated power
PHA_{OUT}	output phase
P_{IN}	input power [dBm]
P_{OUT}	output power [dBm]
$Q-V$	charge-voltage characteristics
Q_{BE}	base to emitter charge
Q_{DS}	drain to source charge
Q_{GD}	gate to drain charge
Q_{GS}	gate to source charge
R_{TH}	thermal resistance
R_D	drain resistance
R_G	gate resistance
R_S	source resistance
t_j	junction temperature
$T_j(f)$	junction temperature spectrum
Y	admittance matrix
$V_1(f)\S$	controlling voltage spectrum
V_{BC}	base to collector voltage
V_{BE}	base to emitter voltage
V_{BEQ}	base to emitter bias voltage
V_{DS}	drain to source voltage
V_{ENV}	2nd-degree voltage mixed to fundamental band from the envelope band
$V_{ENV}(f)$	convolved 2nd-order envelope spectrum
V_{GS}	gate to source voltage
V_{H2}	2nd-degree voltage mixed to fundamental band from 2nd harmonic band
$V_{H2}(f)$	convolved 2nd-order voltage spectrum
V_{in}	input voltage signal
V_n	nth-degree voltage
$V_n(f)$	nth-degree convolved spectrum
V_{out}	output voltage signal
Z_b	base impedance
Z_{FB}	feedback impedance
Z_{IN}	input impedance
Z_L	load impedance
Z_{OUT}	output impedance
Z_S	source impedance
Z_{TH}	thermal impedance
Δf	tone spacing f_2-f_1
τ	time constant

List of original publications

This thesis consists of an overview and the following eight publications:

- I Aikio JP, Rahkonen T (2003) The effect of fitting techniques on the accuracy of distortion simulations using polynomial device models. Proceedings of the European Conference on Circuit Theory and Design (ECCTD'2003), Krakow, Poland, 1-4 Sep. 2003, 3: 325-328.
- II Aikio JP, Rahkonen T (2003), Fitting of polynomial device model based on large-signal voltage and current spectra. Proceedings of the 21st Norchip conference, Riga, Latvia, 10-11-Nov. 2003, 72-75.
- III Aikio JP, Rahkonen T (2004), Fitting of 2-dimensional polynomial device model based on simulated voltage and current spectra. Proceedings of the International Symposium on Circuit and Systems (ISCAS'2004), Vancouver, Canada, 23-26 May 2004, 4: 645-648.
- IV Aikio JP, Rahkonen T (2004), Analysis method of nonlinear self-heating effects based on simulated large signal spectra. Proceedings of the 22nd Norchip conference, Oslo, Norway, 8-9 Nov. 2004, 91-94.
- V Aikio JP, Rahkonen T (2005), Reliability of polynomial I_{DS} - V_{GS} - V_{DS} model fitted using harmonic balance simulation. Proceedings of the European Conference on Circuit Theory and Design (ECCTD'2005), Cork, Ireland, 29 Aug. - 2 Sep. 2005, 3: 89-92.
- VI Aikio JP, Rahkonen T (2005) Detailed distortion analysis technique based on large-signal voltage and current spectra. IEEE Transaction on Microwave Theory and Techniques, 53(10): 3057-3066.
- VII Aikio JP, Rahkonen T (2005), Detailed Analysis of IMD in an LDMOS RF Power Amplifier. IEEE MTT-S International Microwave Symposium Digest (IMS'2005), Long Beach, USA, 12-17 June 2005, 967-970.

VIII Aikio JP, Vuolevi J & Rahkonen T (2006), Detailed analysis of IMD of HBT PA using VBIC model. Proceedings of the 1st European Microwave Integrated Circuits Conference, (EuMIC'2006), Manchester, UK, Sept. 2006, 445-448.

All the above publications were written by the author, who was also responsible for most of the work behind the papers. The spectral based fitting technique and simplified Volterra analysis was developed by the author in co-operation with Prof. Timo Rahkonen. The implementations of the spectral based fitting and simplified Volterra analysis technique was made by the author. The author was also responsible for performing all the detailed distortion simulations and the interpretations of the detailed analysis carried out in this work. The author also performed all the measurements except the load-pull tests of HBT PA that were made by Markku Kyllönen under the guidance of the author. The author was supervised by Prof. Timo Rahkonen who also contributed to the work with his numerous ideas, comments and hints. The idea of extending the spectral based fitting and simplified Volterra analysis to the VBIC model was developed by Dr. Joel Vuolevi in co-operation with the author. The HBT PA was designed by Dr. Joel Vuolevi.

Contents

Abstract	
Acknowledgements	
List of original publications	
List of symbols and abbreviations	
Contents	
1 Introduction.....	17
1.1 Background and aim of the research.....	17
1.2 Contents and contributions of the work.....	18
2 Nonlinearity and memory effects	20
2.1 Nonlinearity	20
2.1.1 Nonlinearity without memory	21
2.1.2 AM-AM and AM-PM	22
2.2 Nonlinearity with bandwidth dependent memory effects.....	24
2.2.1 Modelling a PA with memory	25
2.2.2 Composition of IM3	26
2.2.3 Optimization of IM3	27
2.2.4 Bandwidth dependent memory effects	28
2.2.5 Electrothermal memory effects	29
3 Nonlinear analysis.....	31
3.1 Nonlinear analysis techniques	31
3.1.1 Transient analysis and harmonic balance	32
3.1.2 Envelope simulation	32
3.1.3 Spectral balance	33
3.1.4 Volterra analysis	33
3.1.5 Comparison of the nonlinear analysis techniques	34
3.2 Nonlinear simulation models.....	34
3.2.1 General device models	35
3.2.2 Polynomial device models	37
4 Fitting techniques of polynomial device models	38
4.1 Volterra analysis using polynomial models.....	38

4.2 Polynomial device models	39
4.3 Fitting techniques of polynomial device models	39
4.3.1 Taylor series approach	39
4.3.2 I-V, C-V, and G-V fitting techniques	40
4.3.3 Harmonic based fitting	42
4.3.4 Frequency domain fitting	43
4.4 Comparison of the techniques to build polynomial models	44
4.5 The effect of pdf of the input signal	45
4.5.1 Distortion simulations	47
5 Fitting of polynomial model based on simulated large-signal spectra	49
5.1 Fitting based on large-signal voltage and current spectra	49
5.1.1 Spectral convolution	50
5.1.2 1-dimensional nonlinearity	50
5.1.3 2-dimensional nonlinearity	50
5.1.4 Fitting using correlating inputs	51
5.2 Spectral based fitting in APLAC	52
5.2.1 Simulation procedure	52
5.2.1.1 1- and 2-dimensional fitting procedure in APLAC	54
5.2.1.2 Compensating the delays	56
5.2.1.3 Fitting procedure using different test setups	57
6 Simplified Volterra analysis method	60
6.1 Simplified Volterra method	61
6.1.1 Memory effects and simplified Volterra method	61
6.1.2 Calculating distortion voltage contributions	63
6.2 Comparison of the Volterra methods	67
7 Test cases	70
7.1 Test benches	70
7.1.1 30W LDMOS PA based on MET model	70
7.1.2 HBT PA based on VBIC model	71
7.2 Extending the spectral based fitting to cope with thermal effects	73
7.3 IMD sweet spot analysis	74
7.3.1 Locating the sweet spot	75
7.3.2 Detailed distortion analysis of the sweet spot	75
7.3.2.1 IDQ sweep	75
7.3.2.2 Phasor presentation	77
7.4 AM-AM and AM-PM analysis	79
7.4.1 Measured results	79
7.4.2 Detailed analysis of AM-AM and AM-PM	80
7.4.2.1 Power sweep	81
7.4.2.2 Phasor presentation	83
7.5 Analysing the bandwidth dependent memory effects	85
7.6 Impedance optimization	85
7.6.1 Practical impedance optimization	86
7.6.2 Result of the optimization	86
7.6.3 Detailed distortion analysis	87
8 Discussion	91

8.1 Building a frequency domain polynomial model	91
8.2 Componentwise analysis.....	92
8.3 APLAC implementation	93
8.4 Results of the test cases	94
8.5 Future work.....	95
9 Summary.....	96
References	
Appendices	
Original papers	

1 Introduction

1.1 Background and aim of the research

In the year 2006 the number of mobile phone connections passed the 2.5 billion mark [1], which means, roughly speaking, that every third person in the world possessed a mobile phone. The mobile operators must thus assure that the capacity of the wireless networks satisfies the growing demands. In addition, thus far mainly the voice media has filled the radio channels but the trend towards the digital media including digital pictures, live media, e-mail, Internet etc. is growing rapidly. This altogether has driven the 2nd generation wireless communication systems to their limits. Hence, 3rd generation [2] that has been introduced lately utilizes the wideband code-division multiple access (WCDMA) radio access technology, in which radio channel capacity is increased by widening the bandwidth. In fact, this is not enough as the research towards the 4th generation mobile standards has been ongoing for some time now, in which the orthogonal frequency division multiplexing (OFDM) is suggested as a radio access technology [3].

These new wireless systems need to be specified at higher frequencies as the lower frequencies are already occupied. New systems are very complex and the lack of suitable components makes the implementations difficult. In fact, many solutions for wireless communication standards have been adopted from military or space applications but since the mobile systems are used by billions of people the key issues are cost efficiency, reliability, testability, productivity, usability, etc. For this reason the design of such systems is a huge challenge.

Efficient modulation scheme is used in WCDMA in which the information is modulated in both the amplitude and phase. This results in time varying amplitude. In order to further increase the bit rate, the number of carriers need to be increased. This is possible by widening the bandwidth or by multiband solutions. This altogether results in high linearity requirements for PAs. Usually, linear class A or class AB PAs are used to achieve such high linearity, which, unfortunately, yields to low efficiency. In addition, due to the use of time-varying signals that additionally vary widely and rapidly the linear PA needs to be backed off several dBs from the compression point. For example, in the specifications of 3GPP WCDMA standard [2] the peak to average ratio (PAR) of the WCDMA signal is more than

10 dB, which means that even if the power amplifier is well backed off, the highest peaks might still reach the compression. As a result the efficiency higher than 20% of the backed-off class AB high power amplifier for WCDMA system is difficult to achieve. The rest of the power is transferred to heat, which calls for efficient thermal management. In the mobile device the poor efficiency decreases battery life but the problem is also to prevent the mobile device itself from heating up excessively.

Since the linear class A or AB amplifiers cannot achieve high efficiency, more efficient envelope tracking or envelope elimination and restoration (EER) PAs [4]-[7] have been studied. Thus far, the most common solution to meet the specifications, however, is to bias the PA more efficiently and the linearity requirements are then met by linearizing the amplifier using an external linearizer. Unfortunately, the linearity improvement in broadband wireless communication systems also requires a complex linearizer that together with the PA easily consumes as much power as the low-efficiency high-linearity PA alone.

It is difficult to design an efficient, simple and especially wideband linearizer like a predistorter, for example, because the distortion of a PA is not memoryless but always exhibits some amount of memory that is difficult to cancel. In fact, the memory effects are problematic especially in the wideband applications as will be discussed in this thesis. Here the memory effects are considered distortion variation as a function of bandwidth. This results in the fact that we need to understand the behaviour of the distortion in the PA with and without memory before the distortion can be efficiently cancelled. In order to analyse the distortion in detail an analysis technique that can provide such information is needed. Analysis techniques alone, however, do not suffice but accurate simulation models are needed as well.

The aim of this research is to find out how the distortion is built up and to show which part of the distortion is memoryless and which part has memory effects. Here the polynomial model is used as a nonlinear model for detailed distortion analysis that is performed by Volterra analysis. Thus the main portion of the work aims to reliably fit the polynomial model from the simulated large-signal spectral data. This fitted model and the use of detailed distortion analysis aim at giving more detailed view of nonlinear behaviour, including memory effects. This information is important in order to efficiently minimize the distortion. The proposed technique can be easily implemented in a commercial circuit simulator in which extensive simulations can be made.

1.2 Contents and contributions of the work

The content of this thesis is as follows. The nonlinear phenomena with and without memory is reviewed in Chapter 2. In order to comprehend the detailed analysis of the nonlinear behaviour presented in the Papers and in this overview it is important to understand how nonlinearities emerge, how to measure and most importantly how to model and cancel nonlinearities. An overview of these issues as well as the most used figures of merit of distortion are covered in Chapter 2.

Nonlinear analysis techniques and the simulation models are reviewed in Chapter 3. The literature review of transient analysis, Harmonic Balance, Envelope simulation, Spectral

Balance and Volterra analysis are presented in general including advantages and limitations. In addition, nonlinear analysis methods are compared and their suitability for detailed distortion analysis is discussed. The nonlinear simulation models are also reviewed shortly in Chapter 3.

For detailed distortion analysis the Volterra analysis is the most powerful tool and also used in this thesis. However, it relies on the polynomial models that are by default not available but can be easily fitted. The fitting and characterization techniques for polynomial models are reviewed in Chapter 4. Especially the proposed spectral based fitting technique is described in brief. An example of the effect of the power density function of the input signal by using different polynomial fitting methods concludes the chapter.

A more detailed description of the spectral based fitting is presented in Chapter 5. The technique is based on convolved simulated large-signal controlling voltage spectra and the corresponding output current of the nonlinear source. The fitting technique is mainly described in the Papers, and in Chapter 5 more attention is paid to the implementation of the technique in the APLAC circuit simulator.

The main motivation of the work is obviously the more detailed view of distortion. By the use of the fitted frequency domain polynomial model any distortion component can easily be analysed in detail by using the Volterra analysis. The simplified Volterra analysis method is presented in Chapter 6. This technique is presented shortly in the Papers but a detailed description of the technique is presented in this overview.

In Chapter 7 the spectral based fitting technique and simplified Volterra analysis are applied for detailed distortion analysis. IMD sweet spot, AM-AM and AM-PM, bandwidth dependent memory effects and impedance optimization are analysed in detail. In Chapter 7 also the test benches used in APLAC as well as the real amplifiers are described.

The proposed technique and main results are discussed in Chapter 8, and a summary given in Chapter 9 concludes the overview. In addition, eight original publications published in seven international conferences and in one journal are included in this thesis.

The scientific contribution of the thesis is the development of a unified tool for fitting a polynomial model and calculating intra-device mixing mechanisms of the distortion. The contributions are specified in the following. First, spectral based fitting technique based on the simulated large-signal voltage and current spectra is one of the main contributions of the work. The use of the large-signal spectra solves the problem of determining the correct large-signal bias point and amplitude range. The spectral based fitting is extended to include also electrothermal effects. Second, reliability of the fitting has been a great concern and hence several techniques to make the fitting process more solvable and reliable have been proposed. Third, a simplified Volterra method is proposed for componentwise distortion calculation. A tear-down view of the distortion caused by each nonlinear source can be calculated including also the distortion mixed between frequency bands. Fourth, different methods to efficiently visualise the componentwise information are proposed. From a large number of contributions the essential information is compressed for easier and more visual analysis. Fifth, implementation of the spectral based fitting technique and simplified Volterra analysis in a commercial circuit simulator by using the simulator's command language is an important contribution of the work. Finally, the interpretations and the analysis made of several test cases using the proposed technique are unique.

2 Nonlinearity and memory effects

This chapter deals with the nonlinear phenomena and memory effects. The aim is to provide the necessary background of nonlinear phenomena and the most often used figures of merit of distortion using simple illustrations. First, the nonlinearity in general is discussed and followed by an introduction to spectral regrowth and amplitude dependent amplitude and phase distortion AM-AM and AM-PM, respectively. Then nonlinearity with bandwidth dependent memory effects is described. Finally, the illustration of nonlinearity with memory effects is presented including a detailed analysis of 3rd-order intermodulation distortion (IM3).

2.1 Nonlinearity

Electrical systems can be divided in four different categories, i.e. linear and nonlinear systems with and without memory. Passive components are generally considered linear while active components are more or less nonlinear. Examples of such elements are given in Table 1. The main difference between the linear and nonlinear elements is that the nonlinear systems always generate new frequency components while the linear elements only shape the existing frequency components. The response of the elements with memory depends on the present input but also on all the previous inputs whereas the memoryless element is independent of previous inputs.

Table 1. Examples of linear and nonlinear elements with and without memory.

	Memoryless	With memory
Linear	resistor	capacitor
Nonlinear	nonlinear resistance	nonlinear capacitance

2.1.1 Nonlinearity without memory

The simplest way to model the nonlinearity is to use a memoryless polynomial expansion or power series

$$y = a_0 + a_1 \cdot x + a_2 \cdot x^2 + a_3 \cdot x^3 . \quad (1)$$

The advantage of this approach is the easy calculation of the spectral regrowth, and it has also been presented in many text books [8]-[12]. For completeness, a brief description is given here.

Usually a nonlinear system (especially RF applications) is characterized by applying a 2-tone signal

$$x = A_1 \cdot \cos(2\pi f_1 \cdot t) + A_2 \cdot \cos(2\pi f_2 \cdot t) \quad (2)$$

to the system. In this case a memoryless system modelled using a 3rd-degree polynomial shown in (1) is used, where the coefficients $a_0, a_1, a_2, a_3 = 1$ and the input amplitude $A_1=A_2=0.5$. The output spectrum is shown in Fig. 1, where new frequency components (also called tones) can be seen in addition to the amplified input signals f_1 and f_2 (called fundamental tones (FU)). The amplitudes of the tones can be calculated using Table 7.2 in [9].

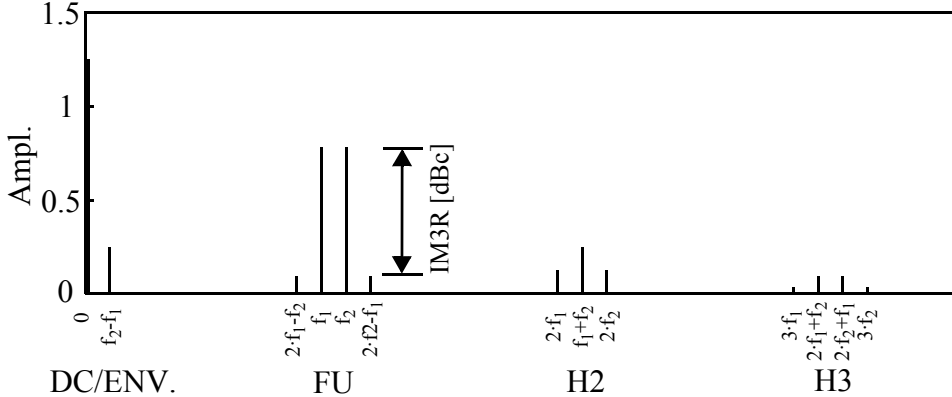


Fig. 1. Output spectrum of the memoryless nonlinear system.

The output spectrum of the nonlinear system consists of different types of tones which are mainly divided into two groups, harmonic and intermodulation distortion. Tones $n \cdot f_1$ and $m \cdot f_2$, where $n, m = 2, 3, \dots$ are considered harmonic distortion (HD) while the tones $|n \cdot f_1 \pm m \cdot f_2|$ where $n, m = 1, 2, 3, \dots$ are considered intermodulation distortion (IMD). In narrowband RF applications the tones appear in groups called frequency or harmonic bands. The general description of the spectral regrowth caused by odd- and even-degree nonlinearity is specified in Table 2.

Table 2. Spectral regrowth caused by odd- and even-degree nonlinearity.

Frequency band	Odd-degree nonlin.	Even-degree nonlin.
DC & envelope band (ENV)	-	DC + IM products
Fundamental band	FU tones + IM Products	-
Odd-degree harmonic bands (H3, H5,...)	harmonic tones and IM products to lower-degree odd-harmonics	-
Even-degree harmonic bands (H2, H4,...)	-	harmonic tones and IM products to lower-degree even-harmonics

The generation of the most important tones up to 9th-degree are shown in Table 1 in Paper I. Note that this holds only when the input signal is a non-distorted 2-tone signal.

The situation becomes more complicated if the input signal is distorted as this results in several mixing mechanisms from different frequency bands. In such a case Table 2.4 in [11] can be used to calculate the output spectrum up to the 3rd-degree. This will be illustrated also in Section 2.2.4.

In general, the distortion components outside the fundamental band can be affected by filtering while the distortion at the fundamental band cannot be removed by filtering without affecting the fundamental tones. The intermodulation products $2 \cdot f_1 - f_2$ and $2 \cdot f_2 - f_1$ also called lower and higher 3rd-order intermodulation distortion (IM3L and IM3H) are thus the most harmful distortion components since they are the strongest and appear next to the fundamental tones. IM3R is the ratio of 3rd-order intermodulation distortion (IM3) with respect to the output power of the fundamental tones and is one of the most often used figures of merit of nonlinearity of the system. In this thesis the causes of IM3 distortion are studied in detail.

2.1.2 AM-AM and AM-PM

The nonlinearity of the system can be estimated also from the fundamental tone only. This can be done by sweeping the input amplitude and measuring the output response of the fundamental tone. The deviation from the linear response is known as amplitude dependent amplitude distortion AM-AM. Furthermore, the nonlinear systems always exhibit some amount of memory and thus also the phase of the output response deviates as a function of input amplitude, which is known as amplitude dependent phase distortion AM-PM [9], [13]. In order to characterize AM-AM and AM-PM, 1-tone input signal is enough. If $x=A \cdot \cos(2\pi f_1 \cdot t)$ is applied to (1), the output spectrum contains only DC, fundamental and harmonic tones.

The simplest way to illustrate the AM-AM and AM-PM using a 3rd-degree polynomial model is to use phasor calculation and complex coefficients in (1). AM-AM and AM-PM are presented in Fig. 2, where the fundamental tone of polynomial model (1) is used with different a_3 values. The fundamental tone is presented as contributions caused by the linear gain a_1 and 3rd-degree nonlinearity a_3 . In Fig. 2a) $a_3 = a_1/2$ causes expansion as the phases of a_1 and a_3 are equal. In Fig. 2b) $a_3 = -a_1/2$ results in 180 degree phase shift between contributions causing a gain compression. In the case of Fig. 2c) imaginary a_3 is used and the phase shift between a_1 and a_3 is 90 degrees causing AM-PM. In the final case shown in

Fig. 2d) complex a_3 is used with a 135 degree phase shift between a_1 and a_3 . This causes both gain compression and AM-PM.

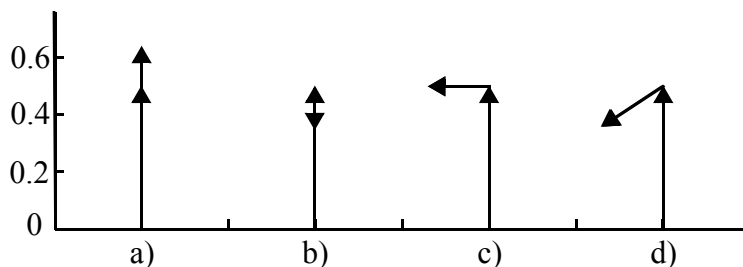


Fig. 2. Amplitude and phase conversion.

The measured AM-AM and AM-PM for a 30 W LDMOS RF PA [15] biased in class AB is shown in Fig. 3. If a digitally modulated signal like WCDMA with PAR of ~ 10 dB is applied to the amplifier, it needs to be backed off about 10 dB from 1 dB compression point in order to prevent the peaks from reaching the compression. The average channel power of the modulated input signal is therefore around 20 dBm while the peaks can be 10 dB larger and thus reach the compression, as seen in Fig. 3. However, at the same time the phase deviates by 7 degrees and furthermore the deviation begins at a lower power level where the amplitude response is linear. This type of behaviour is typical for class AB power amplifiers and may cause linearity problems already before the compression point [9].

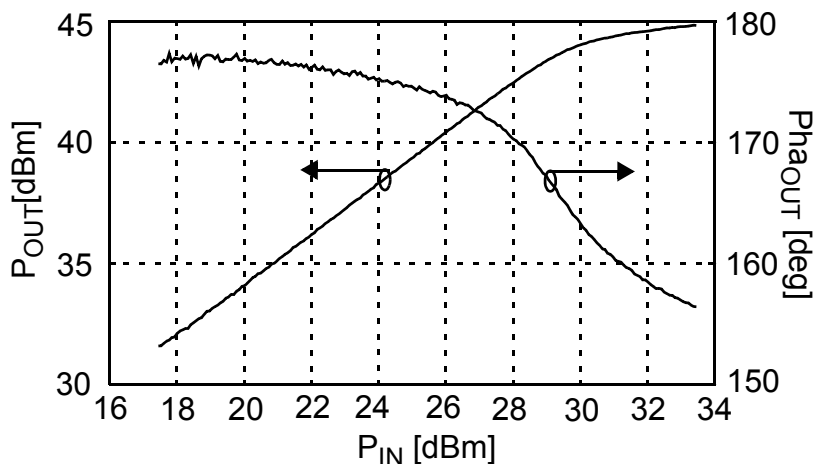


Fig. 3. Measured AM-AM and AM-PM of 30W LDMOS RF power amplifier.

AM-AM and AM-PM are often used figures of merit of nonlinear systems. However, IM3 is usually preferred since AM-AM and AM-PM are difficult to measure accurately. This is because of the fact that in high linearity systems the nonlinearity seen on top of the linear part is very small. The AM-AM and AM-PM shown in Fig. 3 are measured using vector network analyser (VNA) that sweeps continuously the CW signal and measures the

amplitude and the phase response. If fast continuous sweep is used, the thermal steady state for each power level is not achieved. This should be considered if measured results are compared with the simulation in which the thermal steady state is attained for each power level.

2.2 Nonlinearity with bandwidth dependent memory effects

A simple linearizer for a memoryless and narrowband system described above is relatively easy to implement. However, in reality the nonlinear systems always exhibit some amount of memory that can considerably decrease the performance of a simple memoryless linearizer [14]. Bandwidth dependent memory effects can be investigated by a 2-tone test with variable tone spacing ($\Delta f = f_2 - f_1$) which is, in fact, often used instead of a real modulated signal as it simulates a broadband signal and can reveal bandwidth dependencies and low-frequency resonances.

The measured fundamental, IM3 and IM5 tones of 30W LDMOS PA [15] with and without polynomial predistortion [16] are presented in Fig. 4, where the separation between the fundamental input tones is swept from 1 kHz to 30 MHz.

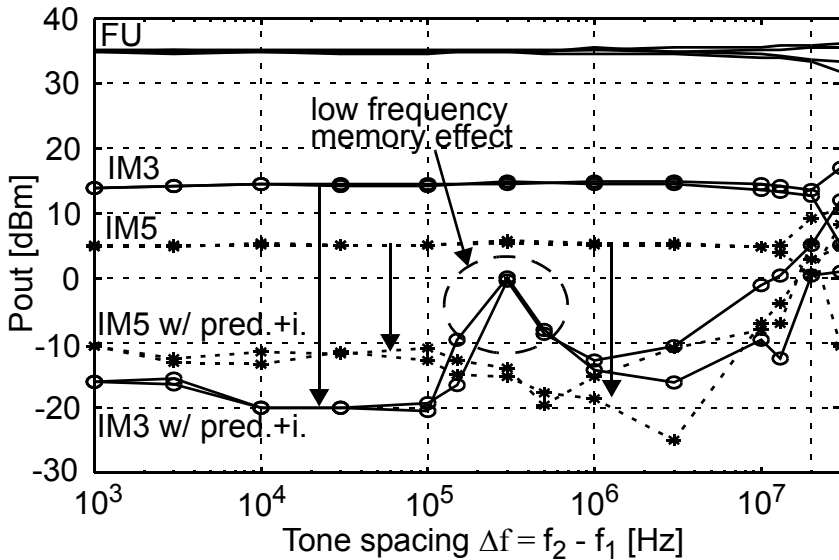


Fig. 4. Measured IM3 and IM5 tones with and without polynomial predistortion as a function of tone spacing Δf .

It can be seen that without predistortion the fundamental, IM3 and IM5 tones as a function of tone spacing are almost flat indicating that memory effects are almost negligible. However, with the predistortion a low-frequency memory effect can be seen at $\Delta f = 300$ kHz in Fig. 4, which reduces the achieved cancellation to 15 dB. This memory effect was caused by a resonating gate bias impedance on the LDMOS PA and was filtered

out with an additional capacitor. By using a modulated signal this low-frequency memory effect would not be so easy to pinpoint.

The memory effects can be separated in general to electrothermal and electrical memory effects [11]. The electrothermal memory effects are caused by the electrothermal coupling that occurs at low modulation frequencies up to the megahertz range. Electrical memory effects are caused by the varying envelope, fundamental and 2nd harmonic node impedances at different modulation frequencies, as will be studied next.

2.2.1 Modelling a PA with memory

Thus far the nonlinear system has been modelled using simple low-degree memoryless polynomial expansion excited with non-distorted 1- or 2-tone input signal in which, for instance, IM3 is caused only by the odd-degree nonlinearity. However, this approach oversimplifies the nature of the nonlinear system as the distortion is, in fact, a result of several mixing mechanisms. First, there is always some feedback within PA meaning that the distorted output is fed back to input somehow. Second, the power transistor of the PA contains several nonlinearities alone and consequently the input signal for some nonlinear elements is already distorted. Third, the existence of the memory needs to be taken into account as well. As a result, more detailed models are needed to study nonlinear phenomena.

As an example, a typical nonlinear feedback structure for a microwave PA with memory is presented in Fig. 5a) [17]. The block A in Fig. 5a) represents the memoryless nonlinear part of the amplifier. The output of block A is shaped by a linear filter $F(f)$ and fed back to input. Blocks $H(f)$ and $O(f)$ represent the linear memory effects related to the input and output matching network. This structure can easily be used for a complete Volterra analysis.

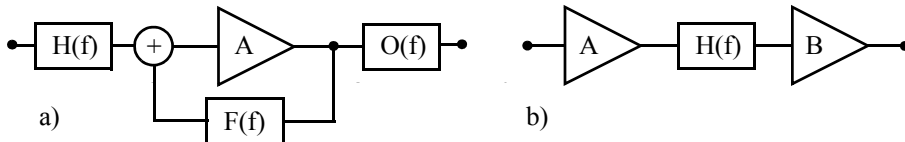


Fig. 5. a) Typical nonlinear feedback structure of a microwave PA [17] and b) cascade of two polynomials.

Calculation of the Volterra analysis using the nonlinear model shown in Fig. 5a) becomes easily laborious and thus a simplified model is often preferred. A typical nonlinear model is the cascade of nonlinear and linear blocks, as shown in Fig. 5b). This structure can be used to study nonlinear phenomena with memory effects but, however, cannot be used for modelling feedback. This cascade structure can also be considered a device model, in which blocks A and B represent the input and output nonlinearity, respectively, and block $H(f)$ is the impedance transfer function between input and output nonlinearities.

2.2.2 Composition of IM3

This section demonstrates by an example how low-frequency resonances seen in Fig. 4 can affect IM3 and cause memory effects. Hence, the cascade structure shown in Fig. 5b) is used in this illustration as a device model as described above. First, a 2-tone signal is applied to input nonlinearity (block A). Then the distorted signal from block A is shaped by the impedance transfer function $H(f)$. Finally, the distorted and shaped signal is applied to output nonlinearity (block B).

A 2-tone input signal with an amplitude of 0.5 is applied to block A which is modelled using a 3rd-degree polynomial (a_0 - $a_3 = 1$). Its output signal is then shaped by $H(f)$ which shorts the DC and 3rd harmonic band and gives unity response for the fundamental band. The envelope and 2nd harmonic band have a purely inductive response. This shaped distorted signal is the input signal of block B which models the exponential transconductance and is also modelled using a 3rd-degree polynomial. The coefficients of the polynomial of block B are $a_i = 10 \cdot a_{i-1}$, where $a_0 = 10e^{-3}$ and $i = 1, 2, 3$.

Next, the generation of IM3 tone at the output of block B is analysed in detail. By using the non-distorted 2-tone input signal and polynomial model up to the 3rd-degree the IM3 in block A is caused only by 3rd-degree nonlinearity. However, as this distorted signal is applied to block B, various mixing mechanisms exist even though block B is modelled using only a 3rd-degree polynomial. The IM3 in block B is caused by the 3rd-degree nonlinearity, but also by 2nd-degree nonlinearity. This is illustrated in Fig. 6. In short, the 2nd-order signal at the envelope (V_{ENV}) and second harmonic (V_{H2}) band mixes with fundamental tones in the 2nd-degree nonlinearity and generates IM3. The total IM3 is the sum of these contributions. Therefore, low-frequency resonances in envelope impedance as depicted in Fig. 4 have an impact on IM3, resulting in bandwidth dependent memory effects.

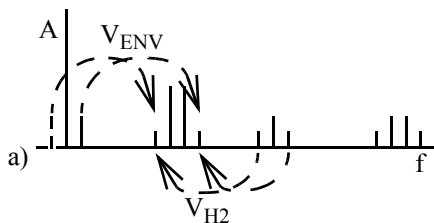


Fig. 6. Spectral components generated by nonlinearities up to the 3rd-degree.

The composition of IM3L tone at the output of block B is presented in Fig. 7a) in which the IM3 is presented as a vector sum caused by the 3rd-degree nonlinearity and 2nd-degree nonlinearity mixed to IM3 either from envelope or 2nd harmonic band. The x-axis in Fig. 7a) is the real part and y-axis the imaginary part of the phasor. It can be seen that the 3rd-degree nonlinearity causes the largest IM3 contributor. The IM3 contributions caused by 2nd-degree nonlinearity are both imaginary and caused by the $H(f)$ in this case. The result vector is the sum of these three IM3 contributors. This detailed analysis is calculated using the simplified Volterra analysis technique presented in Paper VI and in this thesis in Chapter 6.

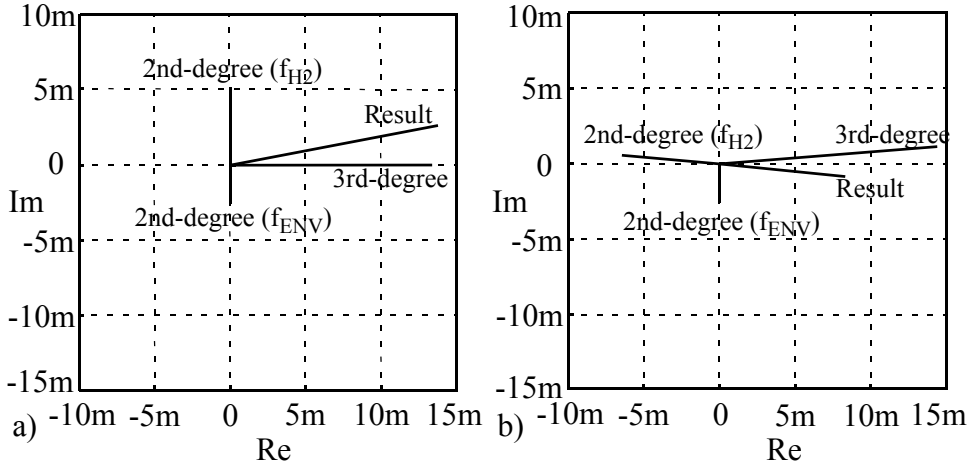


Fig. 7. Composition of IM3L in a cascade of polynomials a) without tuning and b) after tuning the 2nd harmonic of $H(f)$.

2.2.3 Optimization of IM3

The illustration presented in the previous section shows which part of IM3 is caused by the 3rd-degree nonlinearity and which part is caused by 2nd-degree nonlinearity that mixes the 2nd-order distortion from envelope and 2nd harmonic with the fundamental signals to IM3. In addition, the 2nd-order distortion mixed to IM3 is affected by the impedance at the envelope and 2nd harmonic band. This enables the possibility to minimize IM3 by tuning the impedance of the envelope and 2nd harmonic band as this has no effect to the fundamental signal.

In order to illustrate the impedance optimization the IM3 was minimized by manipulating $H(f)$. The results are shown in Fig. 7b). It can be seen that the 2nd-degree nonlinear term mixed down to IM3 from the 2nd harmonic band is rotated and cancels the IM3 caused by the 3rd-degree nonlinearity. This was achieved by rotating the 2nd harmonic response of $H(f)$ by 85 degrees. To maximize the cancellation the magnitude of the 2nd harmonic of $H(f)$ was increased by 25%. As a result, a 4 dB reduction in the total IM3 was obtained. This type of distortion minimization is possible only if transfer functions between nonlinearities can be manipulated. In practice, the impedances cannot be tuned inside the device but the optimization of the input and output matching networks at the envelope and 2nd harmonic is possible and thus can be efficiently used to minimize the distortion.

A componentwise distortion analysis would be difficult by using more realistic multitone or real modulated signals since the number of distortion contributions would become too large resulting in unclear presentation. Moreover, in order to include all the distortion contributions a large number of terms needs to be included to the polynomial. The detailed analysis shown in Fig. 7 is quite easy to comprehend but when the 2-tone test is used to analyse a nonlinear element that is controlled by two voltages with a 5th-degree

model, IM3 consists of more than 30 terms and merely this would make the analysis quite complicated. Therefore, a 2-tone test is used as it enables quite a simple, yet detailed distortion analysis. In addition, by the use of a 2-tone test it is possible to reveal bandwidth dependencies of the nonlinear system by varying tone spacing as shown in Fig. 4. It has been shown also in [18] that a 2-tone test provides much valuable information.

2.2.4 Bandwidth dependent memory effects

The previous illustration shows that IM3 consists of several contributions some of which are mixed to IM3 from different frequency bands. The interest is mainly in the 2nd-degree nonlinearities that mix to IM3 from envelope and 2nd harmonic band which can be affected by manipulating the impedance at the corresponding frequency bands, as illustrated above. The bandwidth in modern wireless communication systems can exceed easily 50 MHz while the centre frequency occurs between 1 and 3 GHz. Therefore, it is generally rather easy to keep the fundamental band as well as the 2nd harmonic band constant. The envelope impedances, however, extend from DC up to tens of megahertz, which is quite difficult to keep constant and therefore is the main cause of bandwidth dependent memory effects. The simulated impedance response at the base node of a HBT RF PA for the envelope, fundamental and 2nd harmonic band is shown in Fig. 8.

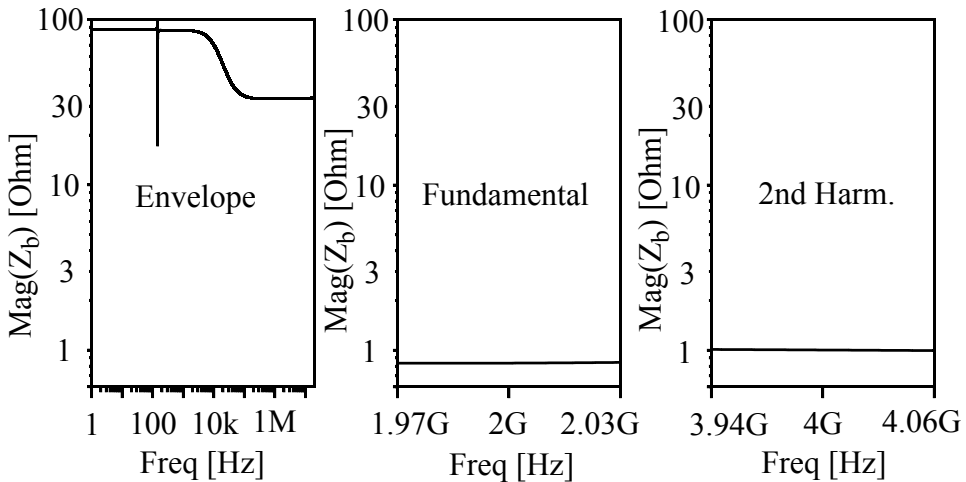


Fig. 8. Simulated magnitude of base impedance (Z_b) of HBT PA.

The centre frequency of HBT PA is 2 GHz and the band of interest is 60 MHz. The corresponding HBT amplifier will be presented in Section 7.1.2. It can be seen that the fundamental and 2nd harmonic bands are almost flat while the envelope impedance varies heavily. There is a large drop in the envelope impedance at 10 kHz that causes bandwidth dependent memory effects to IM3 via 2nd-degree distortion. There is also a low-frequency resonance at 100 Hz caused by the large time constant in the biasing network of the amplifier.

As stated above, the bandwidth dependencies of IM3 can be studied by sweeping the tone spacing of the 2-tone test and observing the variations in IM3 response. The result of the corresponding simulation at the collector node of the same HBT PA is shown in Fig. 9. The tone spacing is swept from 30 Hz up to 20 MHz. Large variations in the phase and magnitude of IM3L and IM3H can be seen in the figure. The magnitude of IM3 is high before it drops 25 dB between $\Delta f = 1 \text{ kHz} - 100 \text{ kHz}$. This IM3 decrease is due to the envelope impedance drop shown in Fig. 8. Also the phase of IM3 varies by almost 100 degrees. It is interesting to note that the magnitude of the IM3L and IM3H are almost equal while the phases are opposite. The variations in IM3 seen in Fig. 9 are large and thus difficult to cancel. The optimization of the envelope impedance would be the most efficient way to cancel bandwidth dependent memory effects in this case. Detailed analysis of this amplifier is presented in Paper VIII and also discussed in Section 7.5.

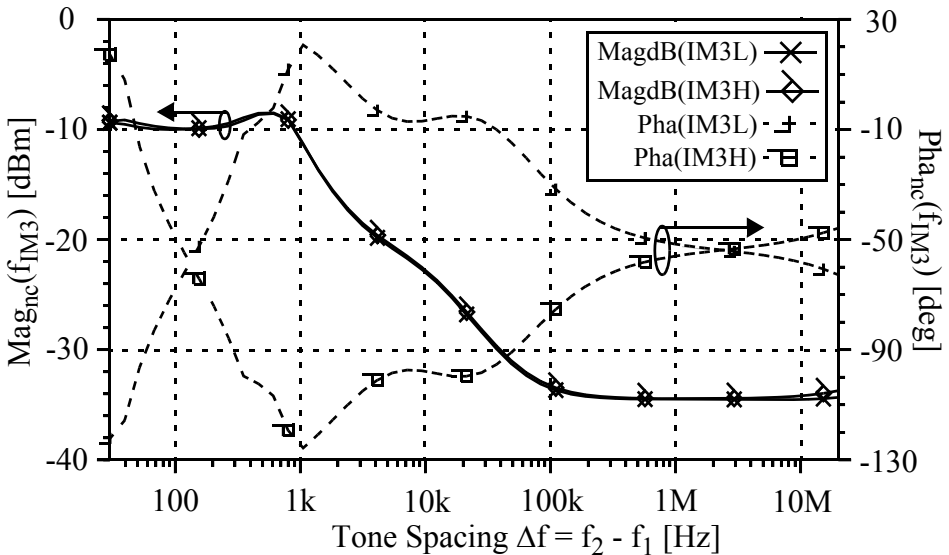


Fig. 9. Simulated IM3 response at the collector node of the HBT PA.

2.2.5 Electrothermal memory effects

Electrothermal coupling may cause electrothermal memory effects in transistor amplifiers [11],[19]. The temperature variations caused by the dissipated power are determined by the thermal impedance (Z_{TH}) [20] which describes the ratio between temperature rise and heat flow from the device. Z_{TH} is not purely resistive due to non-zero mass of the device but forms a lowpass filter with a wide range of time constants as shown in Fig. 10. The time constants also shown in the figure are measured in [20]-[24].

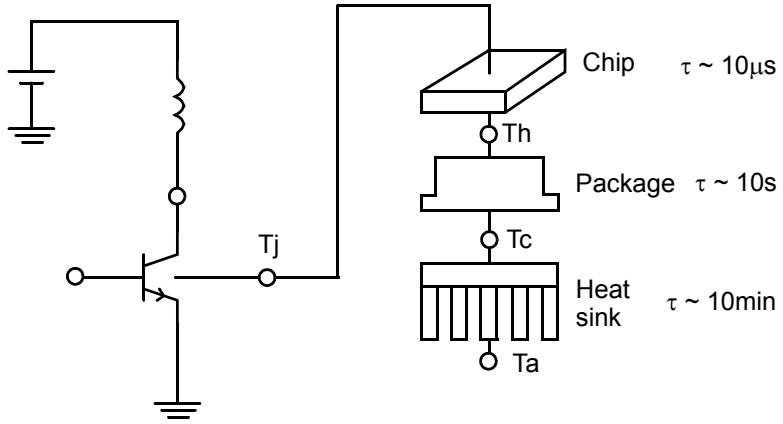


Fig. 10. Heat flow from the device.

3 Nonlinear analysis

This chapter is dedicated for reviewing the nonlinear circuit analysis techniques to obtain an overview of the limitations and advantages of different nonlinear analysis techniques and their suitability for detailed distortion analysis. An accurate nonlinear analysis also calls for accurate nonlinear simulation models. Hence, nonlinear simulation models are also briefly reviewed.

3.1 Nonlinear analysis techniques

The optimization of the dynamic range is the most difficult task in circuit design, calling for optimization of both noise and distortion. Noise analysis tools are well established, and it has been possible for decades to pinpoint the most dominant noise sources [25]. In distortion analysis, however, this has not been the case, as most distortion analysis tools only show the total amount of distortion, giving no guidance how to reduce the distortion. The interest towards more detailed distortion analysis techniques began in the 1990s when more complex wireless communication systems were established. The design of highly linear and efficient PA was and still is difficult due to the lack of design tools that are able to provide the information about the causes of distortion.

Altogether, nonlinear analysis and finding the dominant cause of distortion is not that straightforward. In addition, noise is a stochastic signal and so correlation between different noise sources is quite modest. Distortion, on the contrary, is a deterministic signal and it is quite common that distortion contributions as well as different nonlinear sources do cancel each other, as shown already in Fig. 7 in Section 2.2.3. This means that both the magnitude and the phase of the distortion need to be known accurately. Furthermore, in the RF applications not only the causes of distortion are important but also the various mixing mechanisms that reveal the bandwidth dependent memory effects. Memory effects have been a hot topic in nonlinear modelling for several years, for example [11], [12],[26]-[29]. In the following sections the most common distortion analysis techniques are briefly reviewed.

3.1.1 Transient analysis and harmonic balance

The two main methods for nonlinear circuit analysis used in circuit simulators are the transient analysis and harmonic balance (HB). The transient analysis technique was developed in Berkeley University in the 1970s for the SPICE [30] simulator. Transient analysis is a time domain analysis technique that solves a group of ordinary differential equations numerically. However, transient analysis becomes inefficient with circuits with stiff systems (i.e. $\tau_{\max}/\tau_{\min} \gg 1$), and it cannot calculate directly the steady state response that is usually desired. In addition, circuits with transmission lines and transmission line discontinuities are difficult to analyse in the time domain. In the time domain analysis each linear and nonlinear reactive element adds a differential equation that may increase simulation time excessively [8].

The first general-purpose HB simulator was also developed in Berkeley [31] and it soon became the work horse of steady state analysis of nonlinear RF circuits. Even today it is the most used analysis technique for nonlinear RF circuits. HB has been presented in [8], [12], [32], [33], for example. In HB the linear part of the circuit is calculated in the frequency domain while the nonlinear part that cannot be solved in the frequency domain is converted to time domain using inverse Fourier transform. In the time domain every time sample is solved and the result is then again converted to frequency domain using Fourier transform. The circuit equations in HB are solved using Newton iteration, allowing us to avoid the calculation of the transient and using direct steady state analysis instead. Furthermore, HB works efficiently for passive and linear components that are easier to model in the frequency domain and difficult to analyse using transient analysis. However, nowadays HB can be used purely in the time domain as well [25], which is preferred in the simulations of large integrated circuits (ICs) that usually contain only a few passive or linear components. The usability of HB is limited by the Fourier transform algorithms in which only periodic signals can be used. This limits the use of HB to a few input excitations only. Therefore, more realistic modulated signals cannot be used in HB. However, many algorithms that circumvent this problem are presented for instance in [12].

3.1.2 Envelope simulation

A more sophisticated simulation technique in which more realistic modulated or multitone (not periodic) signals can be used for nonlinear analysis is known as the Envelope Simulation (ES) technique [34], [35]. ES is based on the assumption that the envelope is a slowly varying non-periodic signal that can be solved using time domain integration, whereas the periodic carrier signal can be solved using HB. Hence, ES offers a quick analysis technique of complex signals. The drawback of ES has been that only a small fraction of the fundamental band can be occupied due to the slowly varying envelope signal. However, several techniques have been reported to solve this problem [36]-[38]. In addition, enhanced transformation techniques between the time and frequency domain presentations capable of handling several modulated signals have been reported recently in [39]. ES is available in commercial circuit simulators such as ADS [40] and Eldo RF [41].

3.1.3 Spectral balance

Also the technique called spectral balance (SB) or frequency domain harmonic balance [42]-[44] is developed to circumvent the multitone limitations of HB. SB is a quick and purely frequency domain substitute for the standard HB. In SB nonlinear effects are calculated in the frequency domain by convolving the input spectrum with the spectrum of the transfer function of the model to obtain the spectrum of the output. The advantages of SB include easy modelling of dispersion effects in the frequency domain, quick iteration, and no need to alternate between time and frequency domain presentations. In addition, SB can handle multitone input spectra. The main disadvantage comes from the modelling burden: In SB the polynomial or rational polynomial models are used which need a large number of terms to cover all operating regimes of the device. This is also the reason why SB is not commonly used in circuit simulators.

3.1.4 Volterra analysis

The nonlinear analysis techniques presented above are able to pinpoint only the total amount of distortion. In order to minimize the distortion using HB, different iterative optimization methods have to be used of which the most common is the load-pull method [9]. Iterative techniques are based on sweeping some circuit parameter and observing the total nonlinear response of the amplifier. However, no direct guidance how to minimize the distortion can be obtained. The techniques presented above are iterative and thus cannot give an analytical solution. Fortunately, analysis methods that can provide componentwise information of the distortion do exist. Volterra analysis is the most common method to perform the detailed distortion analysis [8], [45], [46]. In general, Volterra series is a power series with memory. It is thus not an iterative method and therefore capable of providing a closed form presentation of the distortion. The main drawback of a Volterra series is that it is limited to weak nonlinearities only. This results from the fact that it relies on the polynomial models which cannot cover all operating regimes with a reasonable number of terms. However, if the polynomial model is locally modelled around the bias point and large-signal amplitude range, it can be very accurate even for high nonlinear regimes.

Thus far, only very few analysis techniques have been capable of showing anything else but just the total amount of distortion [48], [11] and [49]. The fine structure of distortion has previously been studied using either symbolic or semi-symbolic Volterra analysis or dedicated numerical simulators in [8], [47], [11] and [49], respectively. Per-component information of the distortion is under interest since it is also possible to obtain the information of the bandwidth dependent memory effects, as illustrated already in Section 2.2.2. Bandwidth dependent memory effects are usually the cause of IM3 sideband asymmetry as well. Alternatively, Volterra analysis can be used to design optimal impedances for the envelope and second harmonic bands to minimize overall IM3 [50].

3.1.5 Comparison of the nonlinear analysis techniques

The general features of the nonlinear analysis techniques presented above are compared in Table 3. Transient analysis is purely a time domain analysis technique, while HB and ES use both time and frequency domain techniques. SB and Volterra analysis can be calculated purely in the frequency domain. The Fourier conversion between time and frequency domain presumes a periodic signal that limits the use of multitone input signals in HB. In ES this has been circumvented by the use of a slowly varying envelope signal (non-periodic modulated signal) that is analysed in the time domain, while the periodic carrier is analysed in the frequency domain. Also, since SB is purely a frequency domain technique, a multitone input signal can be used. In Volterra analysis any kind of input signal can be used, but the Volterra calculation expands considerably after a few degrees and thus a low-order model and input signal with a few excitations only is preferred.

Simulation time depends on the time step. In transient analysis the time step depends on the carrier signal while in HB and ES it depends on the modulation. In SB and Volterra analysis there is no time step as those are purely frequency domain presentations and hence very quick techniques for nonlinear analysis. In order to perform detailed distortion analysis using transient analysis, HB and ES polynomial models need to be fitted using the simulated data of the corresponding technique. However, since SB and Volterra analysis are based on polynomial models, detailed distortion analysis is easy to calculate and thus the componentwise mixing between different frequency bands can be pinpointed.

Table 3. Comparison between different analysis techniques for nonlinear circuits.

Technique	Domain	Signal	Time step	Componentwise mixing btw bands
Transient	time	arbitrary	@ carrier	requires
HB	time/freq.	N-tone	@ modulation	polynomial
ES	time/freq.	arbitrary	@ modulation	fitting
SB	freq.	multitone	-	easily
Volterra	freq.	arbitrary	-	easily

3.2 Nonlinear simulation models

In general, two types of simulation models exist, physically and empirically based models. These can be divided further to behavioural models and device models. Behavioural models, or more commonly known as black-box models, can be applied for devices or even complete systems and are mainly used for system simulations. Behavioural models are preferred when there is not enough information to extract the device model or the desired accuracy cannot be attained. Unfortunately, behavioural models cannot be used for circuit level detailed distortion analysis. Since the aim of this work is to identify the componentwise distortion on the circuit level, the interest is thus in device models some of which are reviewed in the following sections. A thorough study of different types of behavioural modelling approaches for nonlinear analysis is given in [17].

3.2.1 General device models

Physical device models are based on the knowledge of the device's physical or geometrical structures and physical laws. However, model equations are usually approximations or based on the measurements of some quantity, which means that purely physical models do not exist [12]. In addition, the parameters needed for purely physical models are difficult to obtain since the device manufacturers are unwilling to release the technology details for obvious reasons. Therefore, in many existing device models closed form analytical models functions are used in order to fulfil the continuity restrictions through the whole of the device operation region, including high order derivatives. This has led the modelling from physical approach to empirical one [51]. Moreover, in many cases the models need to be simplified to speed up the simulation time. Altogether, the following models are already quite sophisticated and thus usable for quite demanding simulations: Philips' MOS model 9 and 11 [52] and BSIM3 [53], [54] for MOSFET transistors, MEXTRAM [55] and VBIC [56] for BJTs and Freescale's MET model [57] for LDMOS devices.

Device models are presented using a set of equations that are lumped in the equivalent circuit. Various nonlinearities of a device are generally considered nonlinear I-V and Q-V sources that are modelled using voltage controlled current or charge source (VCCS) elements. VCCS elements are usually modelled using memoryless functions, which is due to the quasi-static assumption. However, Q-V and I-V nonlinearities often have transit time delays, which is causing memory. In addition to VCCS elements, the equivalent circuit of the device models can also include capacitors and conductances between different nodes as well as terminal resistors.

As an example, an equivalent circuit of Freescale's MET model [57] is shown in Fig. 11. The circuit consists of three nonlinear Q-V sources Q_{GD} , Q_{GS} and Q_{DS} and one nonlinear I-V source I_{DS} . Q-V sources are controlled by only one voltage while the I_{DS} I-V source is controlled by two voltages and is therefore considered as 2-dimensional. A more complex VBIC model [56] for BJT is shown in Fig. 12. This model contains several nonlinear I-V and Q-V sources that are controlled by one voltage while Q-V source Q_{BE} and I-V source I_C are controlled by two voltages. These models are used later in this thesis and hence presented here. Equivalent circuits of the other models can be found from the references.

The model equation of these models contains a large number of parameters that need to be extracted based on measured data or by the geometry of the device. Usually, a set of parameters for a high power device is extracted from a small die that is then scaled up by using a scaling factor of the model to correspond the actual device.

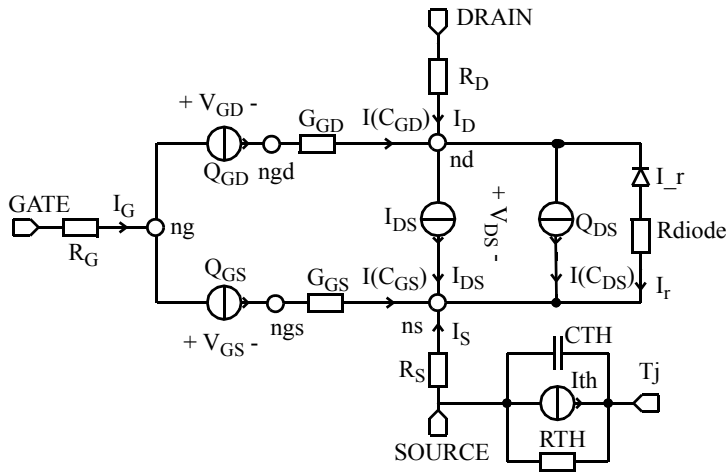


Fig. 11. Equivalent circuit of the intrinsic MET model.

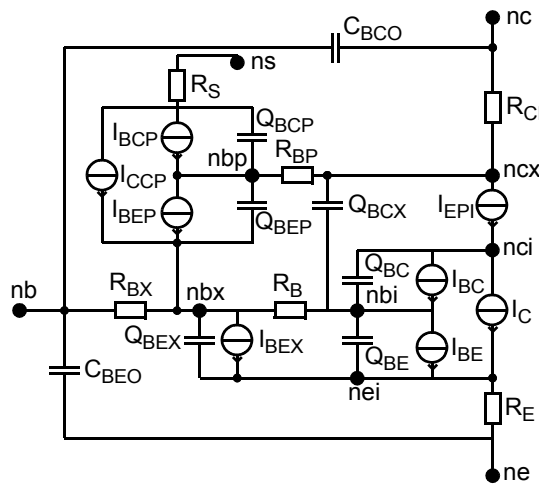


Fig. 12. Equivalent circuit of the VBIC model.

The models presented above include a few enhanced features. First, the transit time which causes delay between input and output enables a more realistic phase response. Second, the models include Q-V or I-V sources that are controlled by both input and output related voltages that might correlate strongly. The fitting problems caused by correlating controlling signals are studied in Papers III and V. And third, the models contain a thermal circuit. The thermal circuit of the MET model is shown in Fig. 11 and consists of a parallel thermal capacitor (CTH) and resistor (RTH). The VBIC model contains a thermal circuit similar to the one in the MET model but it is not shown in Fig. 12. Usually CTH is chosen to be very large so that it shorts everything but DC and RTH is therefore specified to obtain the correct DC temperature. Unfortunately, these thermal models can be used to model only

one time constant and so are unable to model several thermal time constants shown in Fig. 10. This problem has been studied in Paper IV.

3.2.2 Polynomial device models

The empirical models are usually modelled using general mathematical functions that can be used for several different purposes. The polynomial expansion is often used in such models. The coefficients for polynomial model are obtained by differentiating the I-V or Q-V functions or by fitting from the measured data. Polynomial device models can be divided into global and local models. The global model attempts to cover all the operation regimes. Therefore, if the global model is used in high nonlinear regimes, a large number of terms is needed in the series. Usually a fixed-degree and as low-degree series as possible is preferred, as the calculation of the model becomes considerably more complicated after a few degrees. This limits the use of the global model for weak nonlinearities only. On the other hand, the local model that is fitted around a large-signal bias point and amplitude swing is able to give more accurate results locally around the regime it has been extracted to [12]. A locally modelled polynomial model is also capable of modelling accurately highly nonlinear behaviour as shown, for example, in Paper I. This approach is also used in this thesis.

In this work the detailed distortion analysis is performed using a frequency domain polynomial device model that is based on the existing device model. In fact, each VCCS element in the equivalent circuit is replaced by a polynomial model. This technique is presented in more detail in Chapter 5. Altogether, there are many different ways to use polynomial models, which depends on the fitting methods and the data used for fitting. Different fitting methods of polynomial device models and their usability for distortion analysis are reviewed in Chapter 4.

4 Fitting techniques of polynomial device models

This chapter starts by a presentation of the basics of polynomial device modelling. Then, different techniques to build polynomial models are reviewed. This includes the use of derivatives in Taylor series approach, fitting of the coefficients for I-V and Q-V sources using small-signal measured data and also building the polynomial model using harmonic based fitting, and finally a new spectrum based polynomial fitting technique. The comparison of the fitting techniques is then presented. The chapter is concluded by an example of the effect of the power density function of the input signal by using different polynomial fitting methods.

4.1 Volterra analysis using polynomial models

The Volterra analysis relies on the polynomial models as these allow easy calculation of the spectral regrowth and mixing between frequency bands. The Volterra calculation using polynomial models relies on the fact that a time domain product corresponds to a frequency domain convolution, as shown in (3). Thus, the distortion products can be calculated by convolving the spectra of the controlling voltage and temperature, which is a relatively easy task if the spectra consist of a few discrete tones only.

$$v(t) \cdot v(t) \leftrightarrow V(f) \otimes V(f) \quad (3)$$

In short, 1- or 2-tone Volterra analysis is very fast, and moreover, it allows one to separate the distortion terms arising from different nonlinearities and mixing mechanisms, as illustrated in [11] and later in this thesis.

Polynomial device models, however, are not usually available in circuit simulators but physics based or analytical device models are preferred instead as those are able to cover most of the operation regimes. On the other hand, polynomial models can be easily fitted and are flexible to use.

4.2 Polynomial device models

The main idea of using polynomial device models in the circuit analysis is simply that each I-V and Q-V nonlinearity of the device is modelled as a polynomial function of the controlling AC voltages and junction temperature. For example, drain-source current I_{DS} of the FET device can be considered I-V nonlinearity that is controlled by gate-source (V_{GS}) and drain-source (V_{DS}) voltages. Hence, the 3rd-degree polynomial of the $I_{DS} - V_{GS} - V_{DS}$ nonlinearity can be written as

$$\begin{aligned} i_{DS} = & K_{100} \cdot v_{GS} + K_{200} \cdot v_{GS}^2 + K_{300} \cdot v_{GS}^3 \\ & + K_{010} \cdot v_{DS} + K_{020} \cdot v_{DS}^2 + K_{030} \cdot v_{DS}^3, \\ & + K_{110} \cdot v_{GS} \cdot v_{DS} + K_{210} \cdot v_{GS}^2 \cdot v_{DS} + K_{120} \cdot v_{GS} \cdot v_{DS}^2 \\ & + K_{001} \cdot t_J + K_{101} \cdot v_{GS} \cdot t_J + K_{011} \cdot v_{DS} \cdot t_J \end{aligned} \quad (4)$$

where $v_{GS} = V_{GS} - V_{GSQ}$ and $v_{DS} = V_{DS} - V_{DSQ}$ are corresponding AC voltages around bias point Q and $t_J = T - T_Q$ is the signal dependent temperature change. K 's are the coefficients and the indexes of the coefficients K_{nmp} refer to a product term $v_i^n \cdot v_o^m \cdot t_J^p$, where v_i and v_o are the controlling input and output voltages, respectively.

Similarly, for example, the gate-source capacitance (C_{GS}) of the FET device can be considered a Q-V nonlinearity controlled by V_{GS} . Hence, the 3rd-degree polynomial for the $Q_{GS} - V_{GS}$ nonlinearity can be written as

$$q_{GS} = K_{10} \cdot v_{GS} + K_{20} \cdot v_{GS}^2 + K_{30} \cdot v_{GS}^3 + K_{01} \cdot t_J + K_{11} \cdot v_{GS} \cdot t_J, \quad (5)$$

where $v_{GS} = V_{GS} - V_{GSQ}$ and K_{np} refers to a product term $v_i^n t_J^p$.

4.3 Fitting techniques of polynomial device models

4.3.1 Taylor series approach

In principle, a polynomial device model is described by a Taylor series, where the coefficients for the polynomial are derived from high-order derivatives $f^{(i)}(x)$ of the nonlinear curve $f(x)$

$$f(x) = f(x_0) + \sum_{i=1}^n \frac{f^{(i)}(x_0)}{i!} \cdot (x - x_0)^i + R_{n+1}. \quad (6)$$

The complexity of Volterra calculations grows rapidly with increasing degree of the model,

which is why there is a definite interest to cope with as low-degree model as possible, as shown in [47]. With increasing signal amplitude a truncated series inevitably differs from the full series. The error caused by the truncation is indicated as a residue term R_{n+1} in (6). This error can only be minimised by abandoning the fixed derivative values and using coefficients that are fitted for a specific power level, instead. Also, analytical derivative values may be available for simulator device models but not for real physical devices.

One way to extend the accuracy of a Taylor series is to evaluate also the residue term that can be written as [58]

$$R_{n+1} = \frac{1}{n!} \cdot \int_{x_0}^x (x-t)^n \cdot f^{(n+1)}(t) dt. \quad (7)$$

This method is described in [59]. Equation (7) works nicely for point values of x , but in distortion analysis x is a function in time. Hence, R_{n+1} needs to be evaluated in all time points of one cycle of a sine wave, and the Fourier coefficients of the resulting sequence of residues are used for finding the $(n+1)$ th-degree coefficient and updating the lower-degree coefficients as well. Note that for this we need to know the shape of $f^{(n+1)}(x)$, which was approximated from measured data by a series of impulses in [59].

4.3.2 I-V, C-V, and G-V fitting techniques

Another approach is to directly apply polynomial fitting techniques to the measured values. This technique is also presented in Paper I but for completeness the technique is shown here in brief. For example, a 3rd-degree polynomial I-V source

$$i = K_0 + K_{10} \cdot v + K_{20} \cdot v^2 + K_{30} \cdot v^3 + K_{01} \cdot t_J + K_{11} \cdot v \cdot t_J \quad (8)$$

can be fitted most easily by writing a slightly extended Vandermonde matrix M [60] consisting of the polynomial model functions evaluated at each point x

$$M \cdot K = \begin{bmatrix} 1 & x_I & \dots & x_I^N \\ \vdots & & & \vdots \\ 1 & x_J & \dots & x_J^N \end{bmatrix} \cdot \begin{bmatrix} K_0 \\ \vdots \\ K_N \end{bmatrix} = \begin{bmatrix} i_I \\ \vdots \\ i_J \end{bmatrix} = I, \quad (9)$$

from which the coefficient vector K can be solved simply by

$$K = M^{-1} \cdot I. \quad (10)$$

In order to solve N unknowns in (9) $J=N+1$ equation (measured points) are needed.

Often a large amount of data is available and thus it can be used to fit the coefficients. The matrix equation for the polynomial model in (8) using m measured result can be written by

$$M \cdot K = \begin{bmatrix} 1 & x_1 & x_1^2 & x_1^3 & t_1 & x_1 \cdot t_1 \\ \vdots & \vdots & \vdots & \vdots & \vdots & \vdots \\ 1 & x_m & x_m^2 & x_m^3 & t_m & x_m \cdot t_m \end{bmatrix} \cdot \begin{bmatrix} K_0 \\ K_{10} \\ K_{20} \\ K_{30} \\ K_{01} \\ K_{11} \end{bmatrix} = \begin{bmatrix} i_1 \\ \vdots \\ i_m \end{bmatrix} = I, \quad (11)$$

where K is the coefficient vector that can be solved using the least square error (LSE) method by [61]

$$K = (M^T \cdot M)^{-1} \cdot (M^T \cdot I). \quad (12)$$

Since in many cases the Vandermonde matrix is ill-conditioned, orthogonal or close-to-orthogonal polynomials like the Chebychev polynomials can be used to solve the coefficients [62], [63]. This is briefly discussed in Section 8.1.

For device characterization, isothermal I-V measurements are readily available using pulsed DC measurement techniques that can be used to fit the I_{DS} nonlinearity. Unfortunately, the charge needed to fit Q-V nonlinearities cannot be measured directly. Instead, the charge equation (5) is differentiated with respect to the controlling voltage, resulting in capacitance equation. Now capacitance values can be extracted from the measured small-signal AC data that is used to fit the coefficients of the following polynomial equation

$$C_{GS} = \frac{\partial Q_{GS}}{\partial v_{GS}} = K_{10} + 2 \cdot K_{20} \cdot v_{GS} + 3 \cdot K_{30} \cdot v_{GS}^2 + K_{11} \cdot t_J. \quad (13)$$

Note, however, that some data is lost. For example, the temperature dependency of charge $K_{01} \cdot t_J$ is not seen in capacitance measurements. As a benefit, the degree of the model is now lower and fitting becomes easier.

Similar to Q-V sources, also I-V sources can be fitted using the extracted small-signal derivative values g_m , g_0 , as described in [11]. For example, (8) can be fitted using extracted small-signal conductance g expressed by

$$g = \frac{\partial i}{\partial v} = K_{10} + 2 \cdot K_{20} \cdot v + 3 \cdot K_{30} \cdot v^2 + K_{11} \cdot t_J. \quad (14)$$

This also results in a lower degree fitting problem, but requires precisely calibrated and de-embedded pulsed AC measurements. It also loses some temperature drift effects.

4.3.3 Harmonic based fitting

The idea of the harmonic based fitting is to measure the amplitudes of the harmonics and intermodulation products of the modelled device at low frequencies to solve the coefficients of the polynomial. The reason to measure at low frequencies is that the capacitances can be considered open circuits and their nonlinearities can be regarded as negligible. This results in that the major nonlinear component is the g_m -element and the distorted output signal can be expressed as the polynomial in (4).

For example, in [47] the g_m is modelled as in (4) and the input signal

$$v_{in} = V_{in} \cos(2\pi \cdot f_1 t) \quad (15)$$

is applied between the gate and the source of the FET device. The coefficients K_{100} , K_{200} and K_{300} can be extracted directly from the measured harmonic amplitudes by

$$\text{fundamental} = K_{100} \cdot V_{in} \cdot \cos(2\pi \cdot f_1 \cdot t), \quad (16)$$

$$\text{2nd harmonic} = K_{200} \cdot \frac{V_{in}^2}{2} \cdot \cos(2\pi \cdot 2f_1 \cdot t), \quad (17)$$

$$\text{3rd harmonic} = K_{300} \cdot \frac{V_{in}^3}{4} \cdot \cos(2\pi \cdot 3f_1 \cdot t). \quad (18)$$

In order to obtain output related coefficients K_{010} , K_{020} and K_{030} , a test signal is applied to the output. This technique has been extended in [64] to cope with the feedback due to terminal resistances.

In order to obtain also the coefficients for the cross-terms, two input signals are required. However, in most cases the $I_{DS} - V_{GS} - V_{DS}$ source results in strong correlation between V_{GS} and V_{DS} . This is a desired feature of a good amplifier but in this case it is difficult to separate input terms from the output. In order to reduce this correlation, one tone can be applied to the input and the other to the output. This technique has been used in [47] and [65]. In [65] also the terminal impedances have been taken into account. In [66] the low-frequency 2-tone signal is applied to the input only, but the load impedance is tuned so that it is easier to separate input and output terms. This is achieved by setting $Z_L(f_1)$ and $Z_L(f_2)$ to a complex conjugate pair.

Nonlinear Q-V sources can also be extracted by measuring the amplitude of the harmonics. This requires, however, that the transfer functions from the origin of distortion to the measurement point need to be known precisely, as shown in [67], where the characterization of a nonlinear gate-source capacitor is studied. Also in this case some information is lost as the charge needed to fit Q-V nonlinearity cannot be measured directly.

4.3.4 Frequency domain fitting

In the frequency domain fitting the entire spectrum is used to fit the polynomial model instead of characterising the coefficients of the polynomial by measuring the amplitudes of the harmonic tones, for instance. Spectrum based fitting is quite an easy task if the input signal is a non-distorted 1- or 2-tone signal. Non-distorted spectrum of a 2-tone input signal is used in Paper I to fit a low-degree polynomial from a high-degree polynomial model. The idea is just to tune the coefficient to obtain accurately the desired distortion tone. In this way the low-degree polynomial is capable of predicting high nonlinearities accurately. The coefficient vector K of the approach presented in Paper I is basically solved from the matrix equation

$$M \cdot K = \begin{bmatrix} a_{11}A & a_{12}A^2 & \dots & a_{1n}A^n \\ a_{21}A & a_{22}A^2 & \dots & a_{2n}A^n \\ \vdots & \vdots & \ddots & \vdots \end{bmatrix} \cdot \begin{bmatrix} K_1 \\ \vdots \\ K_n \end{bmatrix} = \begin{bmatrix} I_1 \\ I_2 \\ \vdots \end{bmatrix} = I, \quad (19)$$

where K_n is the n th-degree coefficient and I is the current vector containing the selected tones. A in (19) is the amplitude of the input tone and a_{nm} are describing essentially how strongly each tone is affected by a given degree of nonlinearity and are presented in Table 1 in Paper I. This presentation holds only for equal amplitude 2-tone input spectrum and is thus not very practical since in nonlinear devices the input always contains some amount of distortion as discussed in Section 2.2.1.

However, (19) can easily be extended to include the entire spectrum. In fact, even a distorted input spectrum can be used. In such a case the higher-degree spectra need to be convolved according to (3). In (20) the fitting matrix M and current values I of (19) are replaced by the entire voltage and current spectra.

$$\begin{bmatrix} V_1(-f_N) & V_2(-f_N) & \dots & V_n(-f_N) \\ \vdots & \vdots & \ddots & \vdots \\ V_1(-f_1) & V_2(-f_1) & \dots & V_n(-f_1) \\ V_1(f_0) & V_2(f_0) & \dots & V_n(f_0) \\ V_1(f_1) & V_2(f_1) & \dots & V_n(f_1) \\ \vdots & \vdots & \ddots & \vdots \\ V_1(f_N) & V_2(f_N) & \dots & V_n(f_N) \end{bmatrix} \cdot \begin{bmatrix} K_1 \\ K_2 \\ \vdots \\ K_n \end{bmatrix} = \begin{bmatrix} I(-f_N) \\ \vdots \\ I(-f_1) \\ I(f_0) \\ I(f_1) \\ \vdots \\ I(f_N) \end{bmatrix} \quad (20)$$

$V_n(f)$ in (20) is the n th-degree two-sided voltage spectrum. The n -degree spectra are obtained simply by convolving the input spectrum $n-1$ times with itself. In this way the input spectrum may contain distortion components. The coefficients in (20) can be obtained simply by LSE fitting. If $V_1(f)$ and $I(f)$ are the controlling voltage spectrum and the

corresponding output current spectrum of the nonlinear current source, the polynomial model can be built purely in the frequency domain. This spectrum based fitting technique is used in this thesis and is discussed in more detail in Chapter 5.

4.4 Comparison of the techniques to build polynomial models

The comparison of the techniques to build polynomial device models for Volterra analysis is presented in Table 4. The comparison is made mainly by comparing the characteristics of different polynomial fitting techniques. This gives us a clear picture of the capabilities, disadvantages and restrictions of each technique.

Table 4. Comparison of different techniques to build a polynomial device model.

Technique	Ampl. dependent	Missing terms	Deriv. needed	Meas. based	Fitting range
Taylor	no	no	yes	no	no
Residue	yes	no	yes	yes	yes
DC I-V Fit	yes	no	no	yes	yes
C-V & G-V fit	yes	yes	no	yes	yes
Harm. based	yes	yes/no	no	yes	no
SpecFit	yes	no	no	no	no

As stated above, the Volterra calculation becomes complicated after a few degrees, and thus low-degree models are used, which is, unfortunately, applicable only in weak nonlinearities. Polynomial expansions are fixed normally up to the 3rd or 5th-degree. In the Taylor series approach this may not be enough as large number of terms needs to be included to the polynomial in order to model strong nonlinearities. The accuracy of the polynomial model can be improved by local modelling. This approach results in an amplitude dependent polynomial model. All the fitting techniques except for Taylor series in Table 4 are amplitude dependent. The residue technique is similar to the Taylor series approach but the difference is that the coefficients are updated to correspond the large-signal amplitude.

Characterizing all the terms in the fixed-degree polynomial according to (4) and (5) may prove to be difficult. For instance, C-V and G-V techniques are fitted from the small-signal element values but not from the direct charge and current values and thus the series expansion needs to be differentiated with respect to the controlling voltage. As a results some data is lost and therefore some terms cannot be characterized. This is the case also with the characterization of Q-V nonlinearity based on harmonic measurements. The characterization of the full fixed-degree model is also difficult if strongly correlating input and output voltages are both controlling the output current of the nonlinear source. This is typically the case in modelling the 2-dimensional g_m -element using harmonic measurements. Hence, several complex measurement and calculation characterization techniques have been proposed for calculating a full model for I-V and Q-V sources as discussed in Section 4.3.3.

The derivatives are needed in the Taylor series approach. The derivatives might be available from the simulation models but not for real devices. The residue technique is also

based on the derivatives. However, derivatives have been approximated by measuring the harmonic tones [47] while all the other techniques in Table 4 are based on fitting directly the coefficients of the polynomial device model using simulated or measured data.

The possibility to build a polynomial model based on measured data is important in order to extract the polynomial device model from real devices. The Taylor and residue techniques need the derivatives that cannot be obtained from direct measurements but can be approximated as shown in [59]. Also the spectrum based fitting technique cannot be characterized with measurements. This is due to the fact that the controlling voltage and the corresponding output current spectra of the nonlinear source of the actual device cannot be measured in practice. However, the corresponding data can be obtained from the simulation model and hence the spectrum based technique is valuable in the simulator environment, where it is used in this thesis.

The locally fitted polynomial models are amplitude dependent and fitted around the large-signal bias point and signal swing. If the model is extracted using the small-signal data, the large-signal bias point and amplitude range, simply called the fitting range, need to be estimated somehow. The fitting range needs to be defined for the DC I-V fit and C-V and G-V fitting techniques as well as the residue technique in order to update the coefficients to the corresponding large-signal behaviour. In the spectrum based fitting the large-signal data is used for fitting, which includes the information about the bias point and the actual amplitude range. Hence, there is no need to define the fitting range.

DC I-V fit and C-V and G-V fit are fitted based on the small-signal measurements performed at different bias points and temperatures [11]. This enables the measured points to be chosen arbitrarily. This data can also be weighted to match any amplitude power density function (pdf) as will be discussed in next section.

4.5 The effect of pdf of the input signal

The spectrum based fitting technique enables different input signals to be used in building the polynomial model. In this section it is studied how the amplitude power density function of the test signal affects the fitting result and the capability to predict distortion using a modulated signal. In fact, this has been studied in [68], where the DC I-V curve fit (DC fit), the residue update method (Res) using a 1-tone test, and spectrum based fitting using 1-tone (1T), 2-tone (2T), 3-tone (3T), and a QAM-16 modulated (QAM) test signal are compared. The main results are repeated here.

The 3rd-degree polynomial models were fitted using the selected six fitting techniques and compared against the 1-dimensional version of I_{DS} - V_{GS} nonlinearity of Freescale's MET-model [57]

$$I_{DS} = 2.5 \cdot \left(0.21 \cdot \log \left(1 + \exp \left(\frac{v_{GS} - 3.8}{0.21} \right) \right) \right)^{1.2} . \quad (21)$$

The model is biased in class C and excited with a test signal of varying amplitude. The derivatives of (21) are solved analytically up to the 3rd-degree and used for the residue fitting. The 1st- and 2nd-degree coefficients of the residue technique were updated from

their small-signal coefficient values to correspond the amplitude of the test signal. The DC I-V fit was performed by picking points from the DC I_{DS} - V_{GS} curve and fitted into the range of $V_{GSQ} \pm V_{ampl}$, and fitting the polynomial using this data only. Finally, the spectral based fitting was performed using the I_{DS} and V_{GS} spectra of the original model. The models were fitted separately for each input amplitude.

The fitted polynomial coefficients as functions of input peak to peak amplitude are shown in Fig. 13, which is similar to the example shown in Fig. 2 in Paper VI. It is seen that the coefficients are strongly amplitude dependent. At small amplitudes all techniques align with the derivative values of (21), but as the amplitude increases especially K_{10} and K_{30} vary strongly. All the curves have the same general trend, but the 1T fitting always reacts first with increasing amplitude, while the QAM fitting lags behind. The residue fitting gives the same results as a 1T fit (which it essentially is), and also the results of the 2T fit and DC fit are roughly equal.

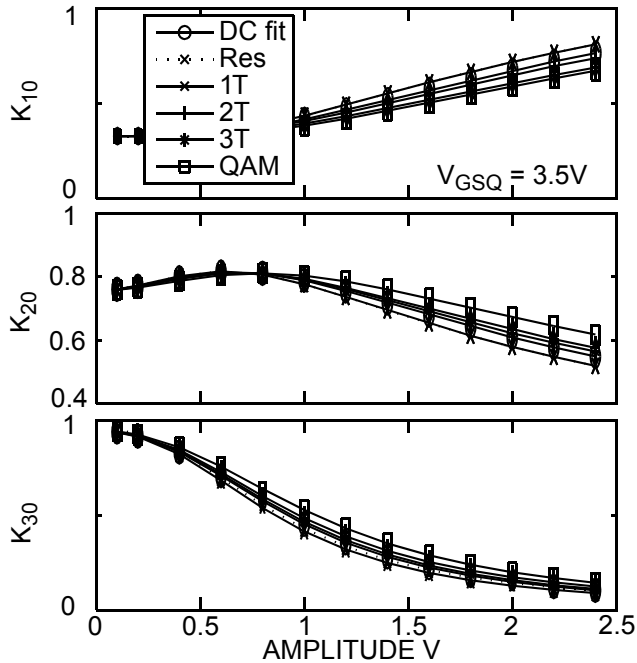


Fig. 13. The polynomial coefficients as a function of input amplitude, fitted using six different fitting techniques.

The reason why 1T fitting always reacts first and QAM fitting last to the increasing amplitude is because the pdf of a 1-tone and QAM signal are quite the opposite. This is illustrated in Fig. 14 in which the histograms of the amplitude distribution of the test signals are shown. It can be seen that the 1-tone signal has a high probability of peak amplitudes, while QAM has an almost Gaussian pdf, and this affects the rate of change of the coefficients. Note that the data for DC fit can be weighted to match any pdf by selecting and weighting suitable data points along the I-V curve.

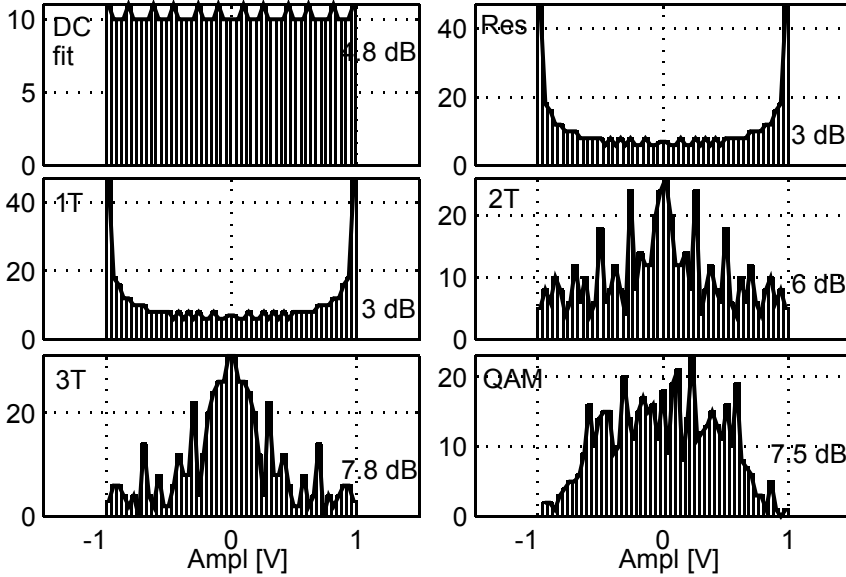


Fig. 14. Histogram including PAR value of each test signal illustrating the amplitude distribution. Amplitude swing is scaled between -1 and 1.

4.5.1 Distortion simulations

Now 2-tone test signal is applied to the polynomial models and their predictability of spectral regrowth is studied. The fundamental, 2nd and 3rd harmonic and IM3 tones of the 2-tone test are compared against the complete MET model as a function of input amplitude for each fitting technique in Fig. 15. All techniques model the fundamental tone well, but the Res, 1T, and QAM fitting have 1-3 dB errors in IM3 tones. At high amplitudes the 3rd harmonics are modelled poorly by all techniques. This is because the higher-order nonlinearities have different effects to the fundamental and 3rd harmonic bands, and while a simultaneous fit cannot be reached with a 3rd-degree model, the fitting methods tend to result in a better fit on the fundamental band.

Finally a long sequence of a high-amplitude 16-QAM signal was simulated. The output spectra of a QAM signal for the fitting techniques and the MET model at the peak input amplitude are shown in Fig. 16. The complete MET model fills the spectrum between the harmonic zones, while the polynomial models contain only 3rd-order distortion spectra. Compared with the 2-tone test signal now 1T and 2T fitting underestimate the IM3 side bands by several dBs. Not surprisingly, the QAM fit results in a very accurate estimate. Also the 3T fit matches well with the MET model.

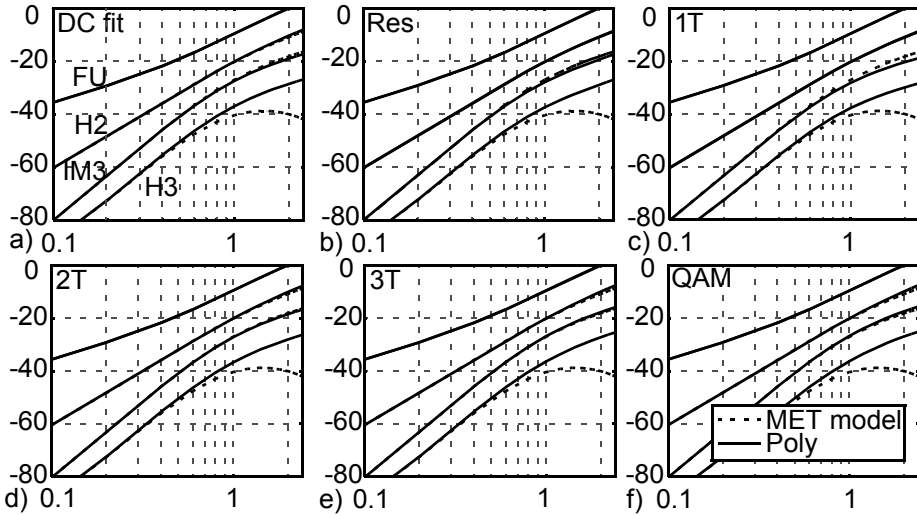


Fig. 15. Fundamental, IM3, 2nd and 3rd harmonic tones vs. input amplitude for six fitting techniques compared with the MET model using a 2-tone test signal.

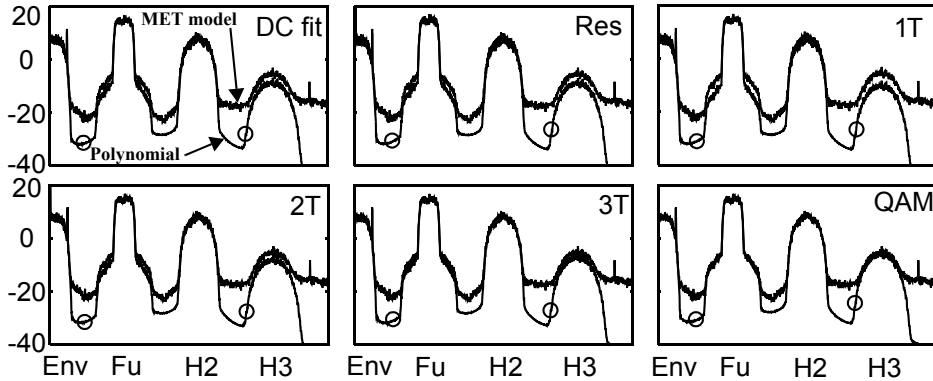


Fig. 16. Output spectra of a QAM signal ($V_{GSQ} = 3.5 \text{ V}$ / $AMPL = 2.4 \text{ V}$) of a 3rd-degree polynomial model of six fitting techniques compared with the MET model.

Altogether, the fitted model depends on the pdf of the test signal. QAM and 3T fit are closest to reality and hence give accurate results. 1T fit overweights the peak amplitudes and, in fact, better results would be obtained by reducing the amplitude by 20 - 30%. In addition, it was demonstrated that a low-degree polynomial model is capable of predicting high nonlinearity accurately if the model is fitted locally. However, in this case the fitting range needs to be known quite accurately.

5 Fitting of polynomial model based on simulated large-signal spectra

In this chapter the proposed spectrum based fitting method is studied in more detail. The proposed technique used for building the polynomial model is one of the main contributions of this work. It is studied in detail in Papers II - VI and therefore only an overview of the technique is presented in this chapter. The basic idea of the technique is presented in Section 4.3.4 and here this idea is extended to apply the simulated large-signal spectra that is obtained from the intrinsic simulation model using HB. The spectral based fitting technique has been implemented in the APLAC circuit simulator and therefore the latter part of the chapter is dedicated to the simulation procedure and implementation in APLAC with illustrative flowcharts. The calculation of the distortion contributions by using the fitted model is presented in Chapter 6.

5.1 Fitting based on large-signal voltage and current spectra

The polynomial model of nonlinear I-V and Q-V source can be fitted by using the controlling voltage spectrum of the source and the corresponding output current, as stated in Section 4.3.4. This gives a couple of advantages. First, when the large-signal spectra are used, the fitting range is not needed as the large-signal data contains the information about the bias point and the large-signal amplitude range. Second, in the frequency domain it is much easier to include delay and dispersion effects to the fitting process. This approach results in a local fit giving an accurate result in the regime of interest. The drawback of the technique is that the controlling voltage and the corresponding output current spectra of all nonlinear sources cannot be measured from the real device. Fortunately, such data can be simulated in a circuit simulator if the access to the intrinsic simulation model is available. Therefore also the accuracy of the fitted model is only as accurate as the simulation model. In fact, the idea is to build a polynomial device model from an existing device model. This may sound ridiculous but the aim is not to obtain a more accurate model but a more detailed analysis instead. In fact, by replacing each nonlinear I-V and Q-V source that is modelled

using VCCS elements with polynomial models the detailed distortion analysis using Volterra analysis can be easily calculated. This technique in general is simple and, moreover, it is able to provide interesting information about the causes of the distortion and especially bandwidth dependent memory effects.

5.1.1 Spectral convolution

In the spectrum based fitting technique the higher-order voltage spectra $V_n(f)$ that are needed to build the fitting matrix M as shown in (20) are obtained by convolution. Calculating the convolution is simply a matrix multiplication using equally spaced two-sided spectra. Convolution is illustrated in Paper VI. For the convolution the spectra need to be two-sided consisting of positive and negative frequencies. The negative frequency tones are the complex conjugate of the positive ones. Convolution results in spectral regrowth which is usually undesirable as the fixed-degree polynomial models are used. Thus it must be assured that the frequency zones do not overlap and this can be done by adding a sufficient amount of zeros between the frequency bands. If a multitone input signal is used, the tones need to be equally spaced.

5.1.2 1-dimensional nonlinearity

Nonlinearity that is controlled by only one voltage is called 1-dimensional nonlinearity. Fitting such a nonlinearity using large-signal spectra is quite simple and has been presented in Papers II and VI. The 1-dimensional I-V nonlinearity can be fitted using a matrix equation (20). Fitting the 1-dimensional Q-V nonlinearity is similar to I-V nonlinearity but the voltage spectra need to be multiplied by the $j2\pi f$ as illustrated in Paper VI. This is because $i=dq/dt$ causes $j2\pi f$ dependency to the nonlinear current of the capacitance [47].

5.1.3 2-dimensional nonlinearity

Nonlinearity that is controlled by two voltages is called 2-dimensional nonlinearity, and the corresponding matrix equation for fitting 2-dimensional I-V nonlinearity is shown in Paper VI. Fitting such a 2-dimensional nonlinearity is more difficult as both of the controlling voltages as well as the cross-terms need to be included in the polynomial model. This substantially increases the number of coefficients to be fitted even in a low-degree polynomial. However, the main difficulty of fitting 2-dimensional nonlinearity is the correlation between the controlling voltages. This is explained in more detail in the next section. The fitting of 2-dimensional nonlinearity has been studied in Papers III, VI and V.

5.1.4 Fitting using correlating inputs

The fitting of 2-dimensional nonlinearity becomes difficult if the controlling voltages correlate strongly. This causes similar columns in the fitting matrix, which results in numerical problems in the fitting process, i.e. the matrix becomes ill-conditioned. Even though the fitting matrix is ill-conditioned, the spectrum based fitting may result in accurate spectra. This is because fitting pursues to fit as accurate a model as possible of the current model. However, this does not indicate that the fitted coefficients are correct. In fact, an ill-conditioned fitting matrix easily causes coefficients large enough to consequently lead into non-physical distortion contributions. The fitting can be verified, for example, by plotting I-V curves over a wide range using the fitted polynomial model. Such plots are presented in Papers II and V.

The easiest way to deal with the correlation is to remove the least significant terms and to reduce the degree of the model. Since the fitting is performed in the frequency domain, it is possible to select the frequencies used for fitting by removing the highest-order harmonic bands, for example. Amplitude and per-equation normalization can also be used to improve the numerical properties of the fit. This is studied in Papers III and V.

In addition, correlation can be reduced by using different characterization test setups as discussed already in Section 4.3.3. In addition to the normal 2-tone input setup (Setup 1) the most useful technique is based on [65] in which 1-tone input - 1-tone output setup is used (Setup 2). This setup is for characterization purposes only. The fitted coefficients using setup 2 can be used for distortion analysis using normal HB data with Setup 1. The drawback of this method is the pdf of 1-tone input signal that weights the peak amplitudes much stronger than the 2-tone input signal, as explained in Section 4.5. However, by reducing the input amplitude by a couple of dB's more reliable results can be obtained. This technique is studied in detail in Paper V, where also the 2-tone input signal with the 3rd tone at the output were used without significant improvement.

In order to circumvent the drawback of the pdf of the 1-tone input signal in the use of Setup 2, the following technique can be used. First, the polynomial model of 2-dimensional nonlinearity including the selected terms

$$\begin{aligned} &K_{10} \cdot V_{10}(f) + K_{20} \cdot V_{20}(f) + \dots + K_{01} \cdot V_{01}(f) + K_{02} \cdot V_{02}(f) + \dots \\ &+ K_{11} \cdot V_{11}(f) + \dots = I(f) \end{aligned} \quad (22)$$

is fitted using Setup 2. This gives the best general result of all the terms, especially the cross-terms and output related terms. The fitted cross-terms and output related coefficients are stored and then Setup 1 is used to fit the input related terms more accurately by

$$\begin{aligned} &K_{10} \cdot V_{10}(f) + K_{20} \cdot V_{20}(f) + \dots \\ &= I(f) - (K_{01} \cdot V_{01}(f) + K_{02} \cdot V_{02}(f) + \dots + K_{11} \cdot V_{11}(f) \dots) \end{aligned} \quad (23)$$

This approach is used in Paper VI. Note that the techniques presented above have been used to build a reliable polynomial model of a 2-dimensional g_m -element of the MET model.

5.2 Spectral based fitting in APLAC

The spectral based fitting technique relies on the large-signal HB data simulated from the intrinsic simulation model, which is performed in the APLAC circuit simulator [25]. In this thesis the implementation of the spectral based fitting technique is called SpecFit. In the first evolution of SpecFit HB analysis was simulated in APLAC and the stored large-signal spectra were imported to MATLAB, where the spectral based fitting as well as detailed distortion simulation were performed. This approach is necessary if the fitting process itself needs to be analysed. However, this procedure is a bit clumsy, since SpecFit needs to be performed after each HB cycle, which prevents us from making demanding sweep simulations. The fitting procedure itself is quite simple, and APLAC has a flexible command language. Therefore SpecFit was implemented in APLAC after the first functional version of the SpecFit process was implemented. In this way, SpecFit was implemented on top of a nonlinear HB simulation in APLAC and thus can be used for quite extensive nonlinear simulations.

The APLAC command language is not, however, as flexible as the MATLAB language [69] and thus a different structure of the SpecFit was implemented. The APLAC command language has quite a simple function structure which cannot be used for complicated operations. Instead, the so-called procedure command block can be used for the purpose. However, all variables, functions, vectors and matrices are local inside the procedure block and cannot be returned to the main program. Fortunately, functions, numeric vectors, matrices and identifier vectors defined outside the procedure block can be used inside the block and are thus usable in the main program. In addition, inside the main SpecFit procedure there are a number of procedure calls that may again contain several procedure calls. As a result, the SpecFit returns the distortion contributions of each source to the main program. The labelling of each contribution is a bit tricky since the APLAC command language does not support a string vector. Instead, labels are saved in text files in the correct order. Hence, the handling of all the variables, vectors and matrices etc. is a difficult task and a large number of temporary variables etc. needs to be used. In addition, when vectors and matrices are declared, also their dimensions need to be known. As a result, a large number of variables needs to be defined beforehand with fixed dimensions.

To sum up, it is quite difficult to implement a general SpecFit program. However, the advantage is that SpecFit is totally functional in the APLAC circuit simulator on top of HB simulation and it is implemented using only the APLAC command language without touching the source code. As a result the SpecFit procedure consists of around 2000 lines of code and takes about 2 seconds on top of HB.

5.2.1 Simulation procedure

The flowchart of the simulation procedure of HB and SpecFit in APLAC is presented in Fig. 17. Prior to the HB analysis the required vectors and variables are declared, and then after the HB analysis the spectra of the internal nodes and branches of the simulation model are stored into the corresponding vectors. The next step is to send the data with the controlling parameters to the SpecFit procedure, where the spectra are sorted, flipped over

the DC axis to obtain two-sided spectra, and additional zeros are added between harmonic bands. As an example, the sorted I_{DS} spectrum is presented in Fig. 18a). After adding 12 zeros between the frequency bands and converting the spectra to two-sided the size of the vector increases from 31 to 181 and is shown in Fig. 18b). All the operations are performed in individual procedure blocks. The next step is to fit the polynomial models of each source. There are four different procedure blocks for fitting and for detailed distortion calculation: 2-dimensional I-V and Q-V nonlinearity and 1-dimensional I-V and Q-V nonlinearity.

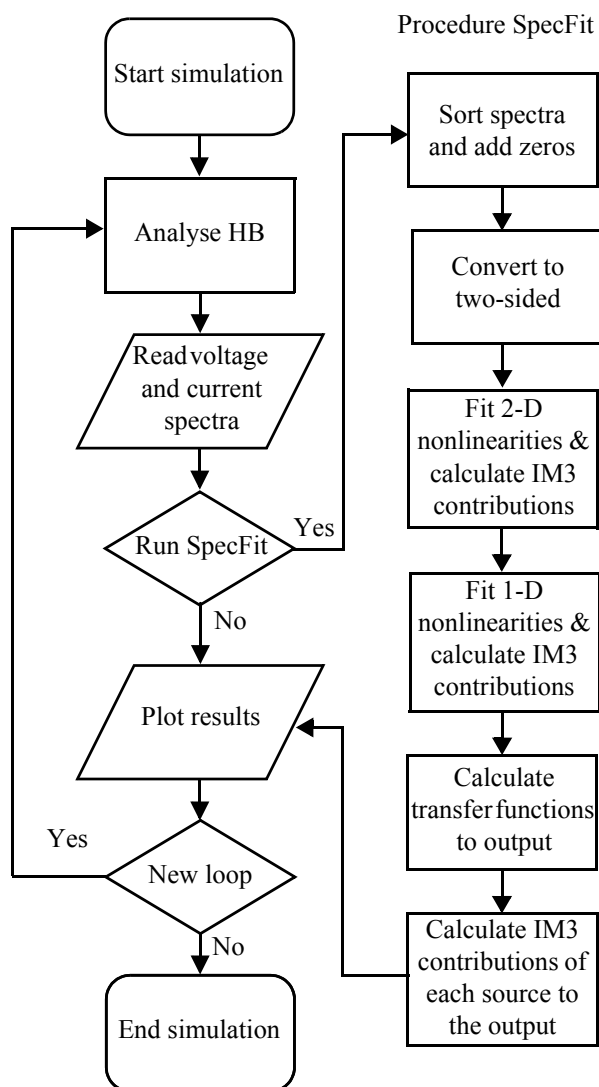


Fig. 17. Flowchart of APLAC simulation procedure for spectrum based fitting and simplified Volterra method using 2-tone input signal.

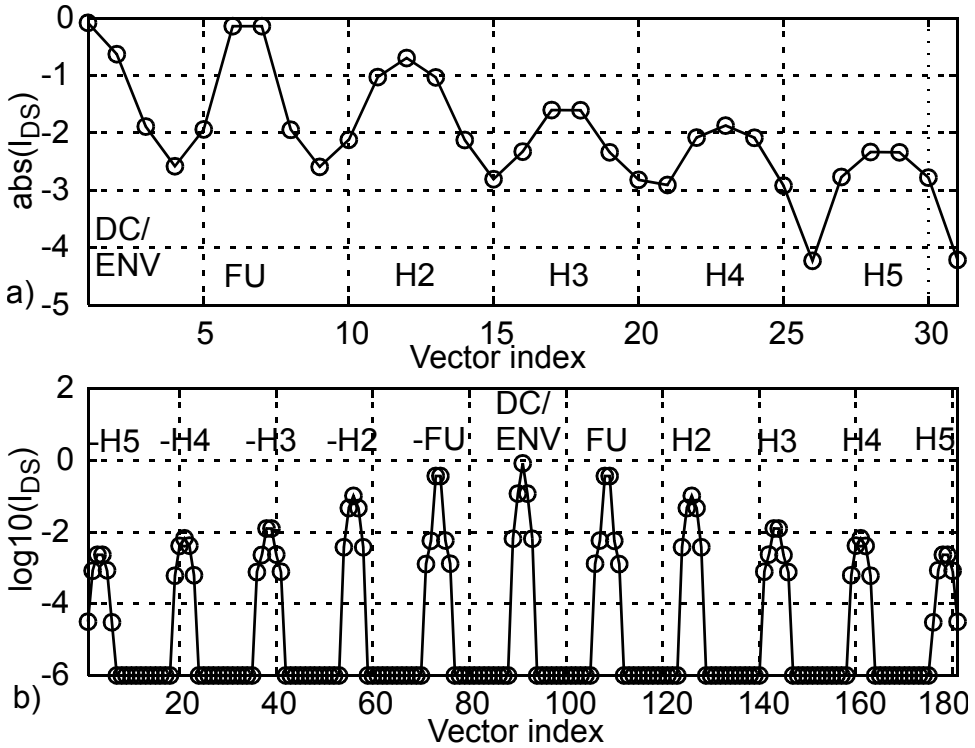


Fig. 18. a) Sorted I_{DS} spectrum vector and b) I_{DS} spectrum vector after adding 12 zeros between harmonic bands and converting the spectrum to two-sided.

After fitting each nonlinear source the obtained distortion contributions are calculated at the output node, which calls for calculating the transfer functions from each source to the output. The next step is to send the distortion contributions back to the main simulation, where the results are plotted. If the simulation continues, the same procedure starts over, otherwise the simulation ends.

5.2.1.1 1- and 2-dimensional fitting procedure in APLAC

The flowchart of the fitting procedure for 1- and 2-dimensional I-V and Q-V nonlinearities are presented in Fig. 19 and Fig. 20, respectively. The procedure for fitting a 1-dimensional nonlinearity is quite simple. First the obtained controlling voltage spectrum is convolved in order to obtain higher order spectra. At the same time these spectra can be manipulated, for example, by masking some frequency tones or frequency bands. In the case of Q-V nonlinearity the DC needs to be removed from the current spectrum and the convolved voltage spectra need to be multiplied by $j2\pi f$. The next step is to fit the coefficients using the LSE method. Using the fitted coefficients and convolved spectra the distortion contributions are calculated and returned to the main SpecFit procedure.

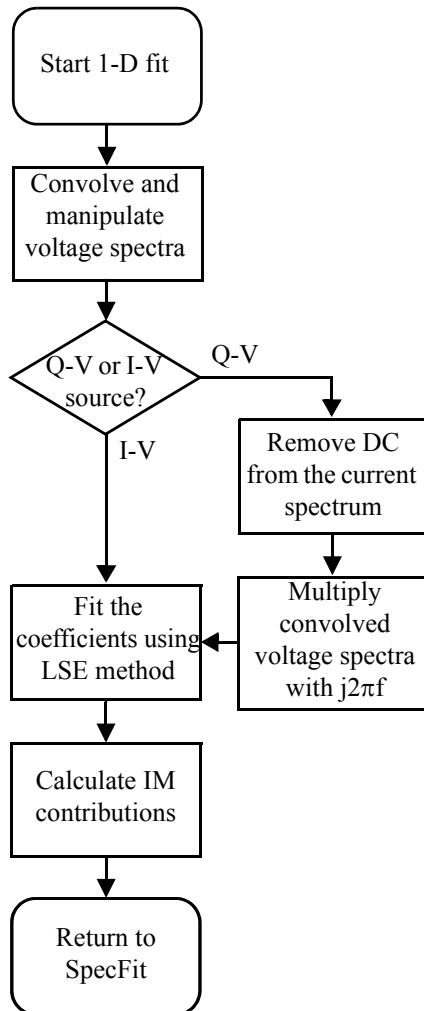


Fig. 19. Flowchart of the implementation of the fitting procedure for 1-dimensional nonlinearity in APLAC.

The fitting procedure of 2-dimensional I-V and Q-V nonlinearity is more complicated. First, the maximum amplitudes of the controlling voltage spectra are normalized to 0.5. Then, DC is removed from the current spectrum of Q-V nonlinearity and delay (usually in 2-dimensional g_m -element includes gate or base transit time) is compensated if necessary. Then higher-order voltage spectra for input, output and cross-terms are convolved as well as the masking operations for the spectra are performed if necessary. Then $j2\pi f$ is multiplied with the convolved voltage spectra of Q-V nonlinearity and per equation normalization is performed for I-V nonlinearity if necessary. Then, the selected coefficients are fitted using the LSE method and denormalized. Finally, the distortion contributions are calculated before returning to the main SpecFit procedure.

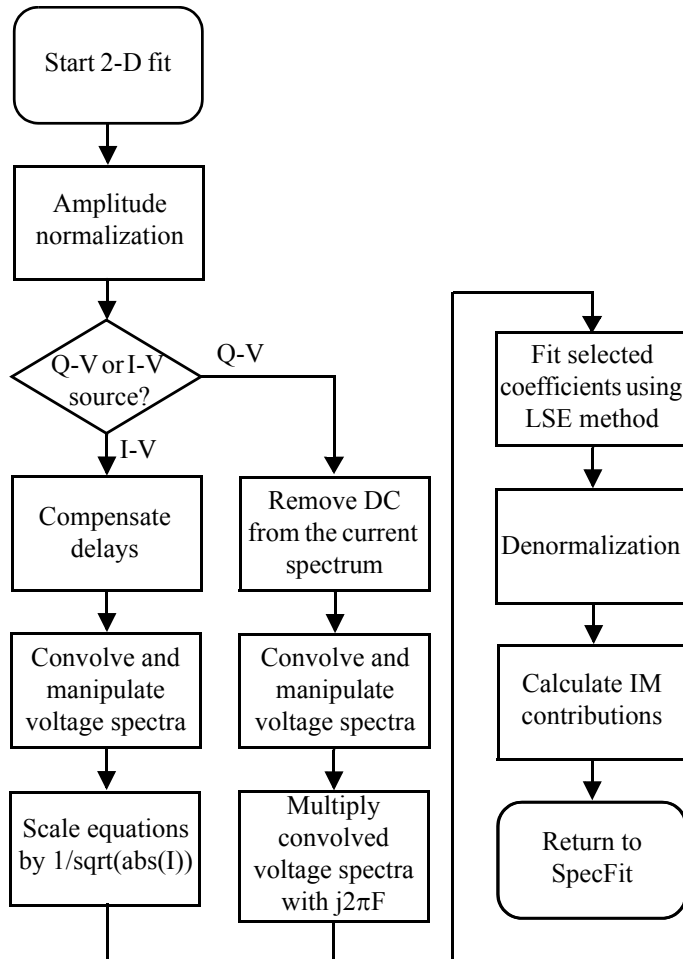


Fig. 20. Flowchart of the implementation of the fitting procedure for 2-dimensional nonlinearity in APLAC.

5.2.1.2 Compensating the delays

Modern sophisticated simulation models include the transit time that causes delay between the input and the output of the device. This is usually modelled within 2-dimensional transconductance. In order to fit the polynomial model of 2-dimensional nonlinearity the controlling voltage spectra and the output current spectra need to be synchronized. Therefore the delay needs to be removed. However, different models have different ways for modelling the delay. In this thesis Freescale's MET model was used as well as the VBIC model. In the MET model the transit time under the gate is added into the V_{GS} controlling voltage [57] while in the VBIC model the delay is added to the output current as a forward

excess phase delay time [56]. These are illustrated also in Fig. 21. In the MET model the delay can be compensated by adding the delay τ_1 into the V_{GS} controlling voltage by multiplying the V_{GS} spectrum with $\exp(-j2\pi f\tau_1)$, which is a simple task in the frequency domain. In the VBIC model the easiest way to compensate the delay is to remove the delay from the output current by multiplying the I_C spectrum with $\exp(j2\pi f\tau_2)$.

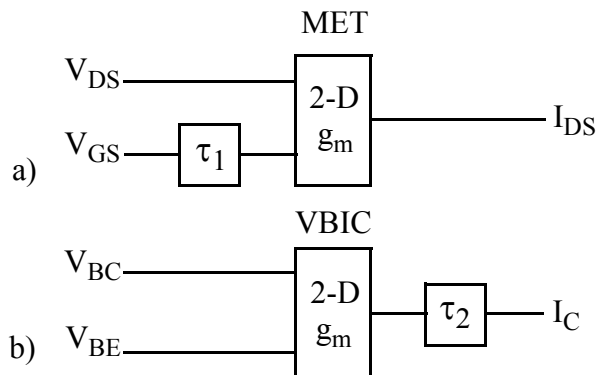


Fig. 21. Delay modelled in 2-dimensional transconductance in a) MET model and b) VBIC model.

5.2.1.3 Fitting procedure using different test setups

The simulation procedure is a bit more complicated if the coefficients need to be characterized using a different test setup or the input coefficients are fitted separately from the other coefficients. It is possible, fortunately, to characterize the coefficients using different setups and to perform the detailed distortion analysis using a normal 2-tone input setup in a single simulation. In such a case the setup shown in Fig. 22 is used. During the simulation the voltage sources seen in the figure can be turned on and off. The voltage source that is turned off is seen as a short circuit or a resistance. In this case the resistance of the output source and other input source are 50 ohms corresponding the 50 ohm source and load impedance. The other input source is seen as a short circuit.

The flowchart of the simulation procedure of different test setups is illustrated in Fig. 23. For the 1-tone input - 1-tone output setup (Setup 2) the other input source is turned off while the output source is turned on. After the coefficients are characterized the output source is turned off and the other input source is turned on to simulate a normal 2-tone input signal (Setup 1). All this can be done simply by applying the simulation inside the loop and sources are controlled by the index of the loop. This technique is functional also in complicated parameter sweeps. In such a case the coefficients are fitted for every HB cycle and stored in the file, where from they are restored for the detailed distortion analysis. A similar setup can be used also if the input related coefficients of 2-dimensional nonlinearity are fitted separately from the output and cross-terms.

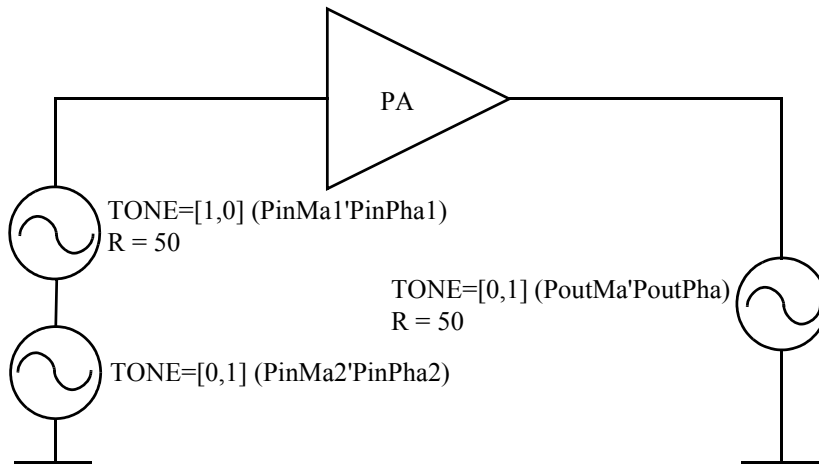


Fig. 22. Test bench for different test setups for the distortion simulation that combines coefficient characterization and detailed distortion analysis.

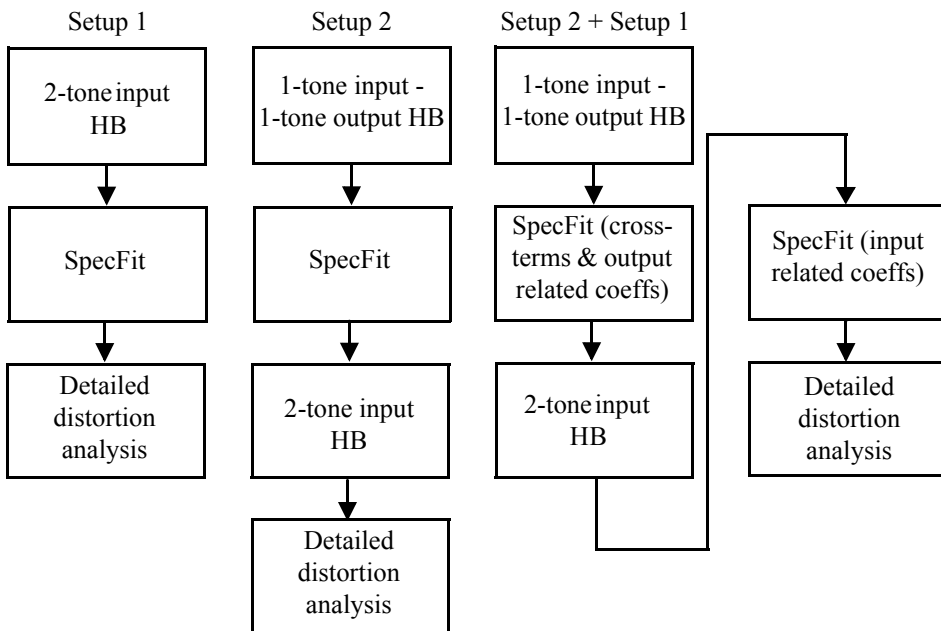


Fig. 23. Flowchart of the simulation procedure using 2-tone input setup (Setup 1), 1-tone input - 1-tone output setup (Setup 2) and Setup 2 for cross-terms and output related coefficients and Setup 1 for input related coefficients (Setup 2 + Setup 1).

Setup 1 can be successfully used if the spectra are strongly distorted. As an example the HBT PA based on the VBIC model can be reliably fitted using this setup, as the input-output correlation is quite modest. The situation is quite different with LDMOS PA based

on the MET model. Due to the high linearity the strongly correlating controlling voltages of I_{DS} - V_{GS} - V_{DS} current source easily result in non-physically large cross-terms if Setup 1 is used. Setup 2 can be used instead, but now the problem is the pdf of the 1-tone input signal. More reliable results are obtained by decreasing the input amplitude by 20-30%. However, the most accurate fitting by using the MET model is obtained by combining Setup 2 and Setup 1. First, Setup 2 is applied to fit the coefficients and then cross-terms and output related terms are used with Setup 1 to fit input related terms with a more realistic 2-tone input signal according to (23).

6 Simplified Volterra analysis method

The Volterra series is widely used for detailed distortion analysis especially as it is not an iterative method but a simple recursion, where linear analysis is repeatedly applied to calculate the response of distortion currents. In the literature two methods, harmonic input method and nonlinear current method also known as direct method, have been proposed for nonlinear circuit analysis using the Volterra series [8], [11], [12], [47], [70]. The harmonic input method is based on the calculation of the system's response to the harmonic inputs also known as Volterra kernels. The direct method is preferred when the system's response to a certain distortion tone using a certain input signal (usually non-distorted 2-tone signal) is evaluated. What is in common to both is that for n th-order analysis n th-degree transfer functions need to be obtained by solving n times the linear circuit. The drawback of these methods is that they do not automatically provide the coefficients for the polynomial nonlinearities, but are obtained either by differentiating the I-V or Q-V functions in the bias point, or by directly fitting a polynomial to these functions over a given amplitude range, as discussed in Section 4.3. In addition, some effects like self-bias drift cannot be simulated unless the coefficients are updated during the calculation.

Instead of the classical methods a rather straightforward method of calculating all the distortion contributions of the selected tone is used in this thesis. It differs from the existing methods in three important aspects. First, while normal Volterra analysis is performed as repeated AC analysis in a given operating point, here a nonlinear steady-state analysis is directly employed. Second, here the polynomial nonlinearities are fitted using actual large-signal spectra so that the DC bias point and amplitude range are automatically correct. Third, normal Volterra analysis starts from a linear response and adds new nonlinearities to it order by order. Here, the complete distorted spectrum is obtained from harmonic balance simulation, and Volterra analysis is used only to calculate how the total distortion is built up from different nonlinearities and mixing mechanisms from other harmonic bands. The proposed distortion analysis technique called a simplified Volterra method is presented in this chapter.

6.1 Simplified Volterra method

The fitting of a polynomial model of each nonlinear I-V and Q-V source of the device was presented in Chapter 5. These nonlinear sources are modelled using VCCS elements and therefore real-valued coefficients are fitted using the controlling voltage spectra and the output current of the source. The controlling voltage spectrum needs to be convolved in order to obtain higher-order terms in the polynomial. Convolved higher-order spectra and the fitted coefficients are then needed also for the simplified Volterra method. In fact, the output current spectrum of the I-V nonlinearity fitted using the spectral based fitting technique can be calculated using matrix equation (20), which can also be presented in the frequency domain polynomial form by

$$I(f) = K_1 \cdot V_1(f) + K_2 \cdot \{V_1(f) \otimes V_1(f)\} + K_3 \cdot \{V_1(f) \otimes V_1(f) \otimes V_1(f)\} + \dots, \quad (24)$$

where $I(f)$ is the output current spectrum, K_n the n th-degree coefficients, $V_1(f)$ the controlling voltage spectrum and \otimes defines the convolution. This frequency domain polynomial is considered a Volterra series expansion as the spectra contain the phase information as well.

As a result of (20) and (24) the entire current spectrum is obtained. Different distortion tones can be calculated simply by picking a line from (20) or by selecting a frequency in (24), and the obtained result is actually the sum of distortion contributions. As an example, the total IM3 current of nonlinear I-V source can be calculated as a sum by

$$I(f_{IM3}) = K_1 \cdot V_1(f_{IM3}) + K_2 \cdot V_2(f_{IM3}) + K_3 \cdot V_3(f_{IM3}) + \dots, \quad (25)$$

in which each term is an IM3 contribution. These contributions can be presented, for example, in a real-imaginary plane in which each contribution starts from the origin. In this way the cancelling effects can be visualised as discussed in Section 2.2.2. Higher-order voltage spectra needed for calculating the distortion contributions are available from the fitting process. Thus a similar presentation can be obtained for any other tone.

6.1.1 Memory effects and simplified Volterra method

Calculating the contributions of the distortion tone is quite a simple task, as presented in the previous section. However, in (25) IM3 contributions caused by mixing the envelope and 2nd harmonic tones with the fundamental tones in 2nd-degree nonlinearity are not separated but included in $K_2 \cdot V_2(f_{IM3})$ term. These IM3 contributions depend on the impedances of the envelope and 2nd harmonic bands, which often are frequency dependent and thus the main cause of bandwidth dependent memory effects as discussed in Sections 2.2.2 and 2.2.4. Therefore, it is important to separate these contributions.

In order to separate the 2nd-order bandwidth dependent distortion, the controlling voltage spectrum $V_1(f)$ can be masked by removing everything but the tones from either the envelope $V_1(f_{ENV})$ or 2nd harmonic band $V_1(f_{H2})$. Then these are convolved separately with the fundamental band $V_1(f_{FU})$ in order to obtain 2nd-degree voltage spectra $V_{ENV}(f)$

and $V_{H2}(f)$. This technique is used in [49] and is also illustrated in Fig. 24 in which the separated voltage spectra masked from the controlling voltage spectrum are shown as well as the 2nd-degree spectra that result from the convolution. The x-axes of the figures are not linear but plotted as a function of vector index for better separation of frequency bands and tones within the frequency bands. DC and envelope bands are in the middle of the spectra followed by the fundamental, 2nd, 3rd, 4th and 5th harmonic bands, respectively.

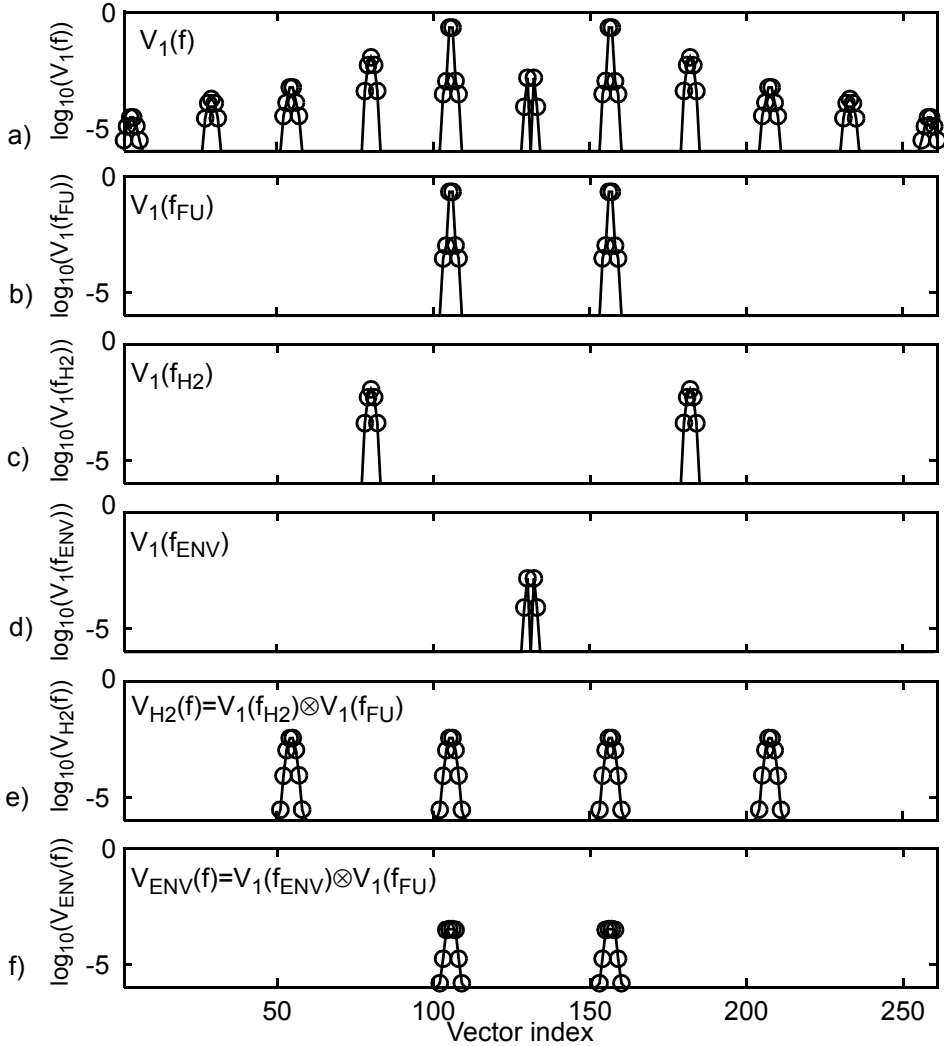


Fig. 24. a) Controlling voltage spectrum $V_1(f)$, b) masked fundamental band from $V_1(f)$, c) masked 2nd-harmonic band from $V_1(f)$, d) masked envelope from $V_1(f)$, e) convolved 2nd-degree voltage spectrum $V_{H2}(f)$ and f) convolved 2nd-degree voltage spectrum $V_{ENV}(f)$.

Now (25) can be easily extended to include the 2nd-degree IM3 distortion mixed from envelope and 2nd harmonic by

$$I(f_{IM3}) = K_1 \cdot V_1(f_{IM3}) + 2K_2 \cdot V_{ENV}(f_{IM3}) + 2K_2 \cdot V_{H2}(f_{IM3}) + K_3 \cdot V_3(f_{IM3}) \dots \quad (26)$$

Also the IM3 contributions of a 1-dimensional Q-V nonlinearity can be calculated by

$$I_Q(f_{IM3}) = j2\pi f_{IM3} \cdot \{ K_1 \cdot V_1(f_{IM3}) + 2K_2 \cdot V_{ENV}(f_{IM3}) + 2K_2 \cdot V_{H2}(f_{IM3}) + K_3 \cdot V_3(f_{IM3}) + \dots \} \quad (27)$$

which is similar to (26), but the contributions need to be multiplied by $j2\pi f_{IM3}$. In the case of 2-dimensional nonlinearity the distortion mixed to IM3 from the envelope and 2nd harmonic can be separated from both controlling voltages. As an example the IM3 contributions of a 2-dimensional I-V source can be calculated by

$$I(f_{IM3}) = K_{10} \cdot V_{10}(f_{IM3}) + 2K_{20} \cdot V_{ENV}(f_{IM3}) + 2K_{20} \cdot V_{H2}(f_{IM3}) + K_{30} \cdot V_{30}(f_{IM3}) + \dots + K_{01} \cdot V_{01}(f_{IM3}) + 2K_{02} \cdot V_{ENV}(f_{IM3}) + 2K_{02} \cdot V_{H2}(f_{IM3}) + K_{03} \cdot V_{03}(f_{IM3}) + \dots + K_{11} \cdot V_{11}(f_{IM3}) + K_{21} \cdot V_{21}(f_{IM3}) + K_{12} \cdot V_{12}(f_{IM3}) + \dots \quad (28)$$

The calculation of the IM3 current contributions presented above apply only in the output current of the corresponding nonlinear source. Hence, the interactions of distortion between different nonlinear sources cannot be analysed directly at the output (or input) of the device. Distortion currents, however, can be summed only at the nearest node. Fortunately, in case the structure of the simulation model is quite simple like in the MET model shown in Fig. 11 the output current of the I_{DS} - V_{GS} - V_{DS} I-V source and C_{DS} - V_{DS} and C_{GD} - V_{GD} Q-V sources can be summed at the intrinsic drain terminal. However, the effect of the C_{GS} - V_{GS} Q-V source cannot be seen directly at the same node, but the distortion is lumped into the controlling voltages of the C_{GD} and g_m -element and is furthermore amplified by the linear portion of the corresponding sources. This approach has been used to calculate the IM3 current contributions using the MET model in Papers II-VII.

6.1.2 Calculating distortion voltage contributions

The major drawback of the simplified Volterra method presented in the previous section is that the effect of all the nonlinear sources cannot be analysed in the same node but the effect of some sources is lumped in the linear terms of other sources. In addition, it is impossible to distinguish which part of the distortion seen at the controlling voltages is caused by the feedback and which by other nonlinear sources. Therefore, the analysis becomes a bit clumsy. With the use of more complex models this approach becomes impractical or even

impossible. This is the case, for example, in the VBIC model presented in Fig. 12. Therefore, the response of each nonlinearity needs to be analysed directly to the input or output node. This calls for building transimpedance transfer functions from each nonlinear source to the input and output.

Such transimpedance transfer functions can be obtained by building an equivalent network of the circuit and lumping all external circuitry into the terminal impedances. The equivalent circuit of the FET amplifier using the MET model is shown in Fig. 25.

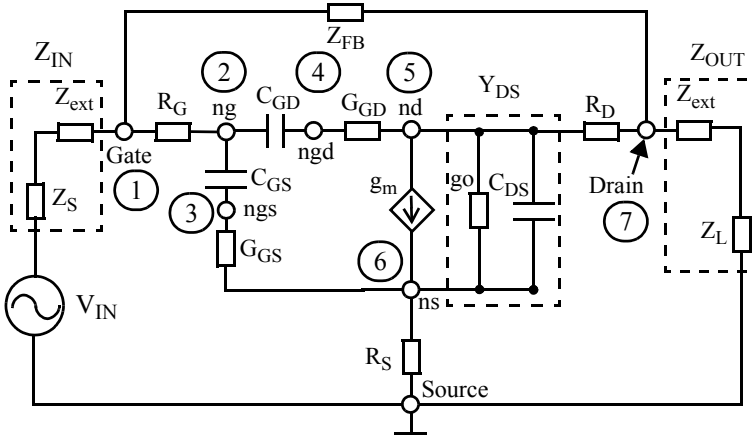


Fig. 25. Linearized circuit of the FET amplifier using a simplified MET model.

External circuitry including matching networks outside the device and internal matching network etc. are included in the terminal impedances Z_{IN} , Z_{OUT} and Z_S . The MET model is used to model an internally matched RF device and thus the package is included to the test bench. Therefore there is an additional feedback route denoted as Z_{FB} between the gate and drain nodes. The external circuitry and feedback can be characterized simply by removing the internal device and simulating Y-parameters of the external network, as shown in Fig. 26. Now the external circuitry can be solved by

$$\begin{bmatrix} Y_{IN}(f_{IM3}) + Y_{FB}(f_{IM3}) & -Y_{FB} \\ -Y_{FB}(f_{IM3}) & Y_{OUT}(f_{IM3}) + Y_{FB}(f_{IM3}) \end{bmatrix} = \begin{bmatrix} Y_{11}(f_{IM3}) & Y_{12}(f_{IM3}) \\ Y_{21}(f_{IM3}) & Y_{22}(f_{IM3}) \end{bmatrix} \quad (29)$$

$$\Rightarrow \begin{cases} Y_{FB}(f_{IM3}) = -Y_{12}(f_{IM3}) \\ Y_{IN}(f_{IM3}) = Y_{11}(f_{IM3}) + Y_{12}(f_{IM3}) \\ Y_{OUT}(f_{IM3}) = Y_{22}(f_{IM3}) + Y_{12}(f_{IM3}) \end{cases}$$

If the external feedback Z_{FB} does not exist then Z_{IN} and Z_{OUT} can be calculated by using the input and output currents and voltages at IM3 frequency. Some of the linear parameters (G_{GS} , G_{GD} , R_G , R_D and R_S) needed for building the transimpedance transfer functions can be calculated with the use of the simulated spectra except for the time delay that needs to

obtained from the model parameters. The rest are obtained as a linear part of the large-signal fitting of the nonlinear sources (g_m , g_o , C_{DS} , C_{GD} , C_{GS}).

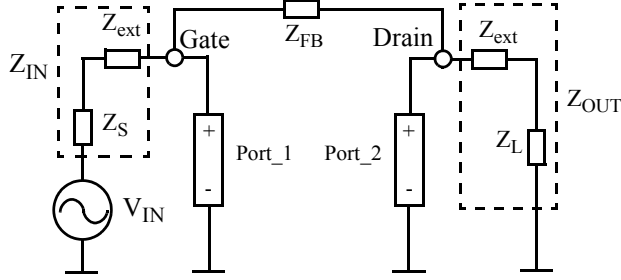


Fig. 26. Setup for characterising external circuitry for the transfer functions.

Based on the equivalent circuit of Fig. 25 and using the following shorthand notations

$$\begin{aligned}
 Y_{DS}(j2\pi f) &= g_o + j2\pi f_{IM3} \cdot C_{DS} \\
 Y_{Qgs}(j2\pi f) &= j2\pi f_{IM3} \cdot C_{GS} \\
 Y_{Qgd}(j2\pi f) &= j2\pi f_{IM3} \cdot C_{GD} \\
 \phi &= 2\pi f_{IM3} \cdot \tau
 \end{aligned} \tag{30}$$

the transimpedance matrix (32) can be set up by changing all the impedances in Fig. 25 to admittances and applying Kirchhoff's current law at nodes 1 to 7.

Now, the effect of each nonlinear source in each node can be calculated simply by solving the group of node equations by $V=Y^{-1} \cdot I$, where V is the vector of node voltages, Y is the transimpedance matrix and I contains the nonlinear current contributions calculated using the simplified Volterra method. One way to calculate the voltage response of the distortion contributions to the selected node is to initialize nonlinear current contributions separately in vector I while leaving the rest of the vector to zero and then calculating the matrix product. However, this means that the matrix product needs to be calculated for each nonlinear current contribution. As an example, the IM3 voltage in each of the seven nodes of the 3rd-degree nonlinear current of I_{DS} current source can be calculated by

$$\begin{bmatrix} Gate \\ ng \\ ngs \\ ngd \\ nd \\ ns \\ Drain \end{bmatrix} = Y^{-1} \cdot \begin{bmatrix} 0 \\ 0 \\ 0 \\ 0 \\ -(K_3 \cdot V_3(f_{IM3})) \\ K_3 \cdot V_3(f_{IM3}) \\ 0 \end{bmatrix}. \tag{31}$$

$$Y = \begin{bmatrix}
 Y_{IN} + G_G + Y_{FB} & -G_G & 0 & 0 & 0 & -Y_{FB} \\
 -G_G & G_G + Y_{Qgs} + Y_{Qgd} & -Y_{Qgs} & -Y_{Qgd} & 0 & 0 \\
 0 & -Y_{Qgs} & Y_{Qgs} + G_{GS} & 0 & 0 & -G_{GS} \\
 0 & -Y_{Qgd} & 0 & Y_{Qgd} + G_{GD} & -G_{GD} & 0 \\
 0 & g_m \cdot e^{-j\phi} & -g_m \cdot e^{-j\phi} & -G_{GD} & G_D + G_{GD} + Y_{DS} & G_D \\
 0 & -g_m \cdot e^{-j\phi} & g_m \cdot e^{-j\phi} - G_{GS} & 0 & -Y_{DS} & 0 \\
 -Y_{FB} & 0 & 0 & 0 & -G_G & Y_{OUT} + G_D + Y_{FB}
 \end{bmatrix}$$

(32)

So far the method is functional within a single nonlinear device only. In order to analyse more complex circuit topologies with several nonlinear devices, transfer functions of the complete circuit are needed as well as the simultaneous Volterra calculation between different devices. As the proposed method is based on the use of existing simulation models, the access to the internal model as well as to the device parameters is needed. These limit the use of the proposed method to the circuit simulator environment only. Despite these limitations the proposed technique is very illustrative, versatile and flexible for detailed distortion analysis as shown in chapter 7.

A Volterra study using the direct method for a similar test bench shown here has been applied for hand calculations based on real measured data in [71], and using a numerical Volterra simulator in [72]. In both studies the polynomial models of the nonlinear sources are characterized using small-signal S-parameters. These studies can be used to directly compare the proposed method with the direct method.

6.2 Comparison of the Volterra methods

In this section two presented approaches of detailed distortion analysis using the simplified Volterra method are compared. The first approach is based on simply summing the nonlinear current contributions of the sources to the nearest node and lumping all the rest to the controlling voltages of those sources. The other calculates the response of all the nonlinear current contributions to voltages in each node. A test bench modelling the LDMOS PA based on MRF21030 power transistor [73] presented in Section 7.1.1 is used. For HB analysis the centre frequency of the 2-tone test is $f_0 = 2140$ MHz with 2 MHz tone spacing. The device is biased in deep class AB ($I_{DQ} = 100$ mA) and the input amplitude is set to $P_{IN} = 15$ dBm/tone.

The polynomial models for each nonlinear source of the MET model are fitted based on the method presented in Chapter 5. Then the IM3 contributions are calculated as presented in this chapter and plotted as phasors in Fig. 27 similar to Fig. 7. The smallest contributions are not shown. In the analysis the contributions are denoted generally as $K_n \cdot V_n$, where K_n is the nth degree coefficient and V_n are the corresponding convolved spectra. The generated IM3 is summed and separated from linearly conducted IM3 current and denoted as gen_{IM3} and $K_1 \cdot V_1$, respectively.

In Fig. 27a) the vector plot of IM3 current contributions of the most dominant $I_{DS}-V_{GS}-V_{DS}$ source is presented. It can be seen that the 3rd-degree input nonlinearity generates most of the IM3. The 5th-degree nonlinearity is at the opposite direction causing cancellation with the 2nd-degree nonlinearity mixed to IM3 from the 2nd harmonic. The controlling voltage V_{GS} of $I_{DS}-V_{GS}-V_{DS}$ source contains also some IM3 and it is amplified by the linear portion (g_m or K_{10}) of the source. The IM3 voltage contributions at the intrinsic drain node presented in Fig. 27b) are calculated from the IM3 current contributions shown in Fig. 27a) by the use of the transimpedance transfer functions presented in Section 6.1.2. The presentations between Fig. 27a) and b) are basically the same. The phasors have been rotated in the opposite direction due to the transfer function. The main difference is the absence of the linear terms that cannot be distinguished any more.

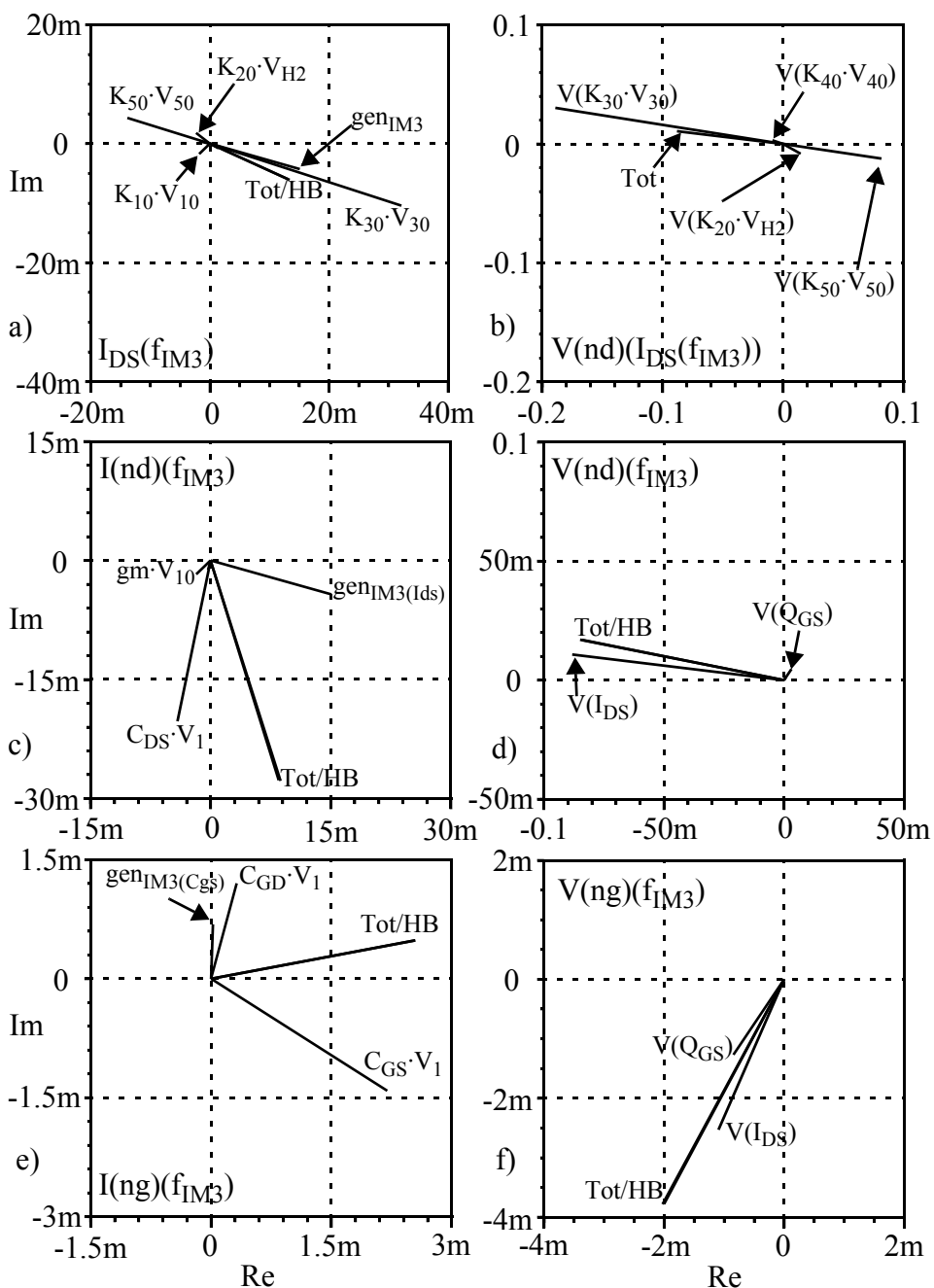


Fig. 27. Vector plot of a) IM3 current contributions of $I_{DS} \cdot V_{GS} \cdot V_{DS}$ source, b) IM3 voltage contribution of $I_{DS} \cdot V_{GS} \cdot V_{DS}$ source at the drain, c) total IM3 currents summed at the drain, d) total IM3 voltage contributions at the drain, e) total IM3 currents summed at the gate and f) total IM3 voltage contributions at the gate.

In Fig. 27c) the total IM3 currents from the $I_{DS-V_{GS}-V_{DS}}$, $C_{DS-V_{DS}}$ and $C_{GD-V_{GD}}$ sources are summed at the intrinsic output node. The IM3 generated by the sources are separated from the linearly amplified terms. It can be seen that the $I_{DS-V_{GS}-V_{DS}}$ source is generating most of the IM3 current. However, a large portion of IM3 is shifted or amplified by the linear term of $I_{DS-V_{GS}-V_{DS}}$ (g_m) and surprisingly large $C_{DS-V_{DS}}$. This results from the fact that $C_{DS-V_{DS}}$ source is part of the output match and only shifts the IM3 seen at the drain. The presentation is quite different when calculating the IM3 voltage response of each nonlinear source to the intrinsic output node. This is shown in Fig. 27d). Now the total IM3 is caused mainly by the $I_{DS-V_{GS}-V_{DS}}$ source and only a small amount of IM3 is caused by the $C_{GS-V_{GS}}$ source while the other Q-V sources are almost linear.

A similar analysis of the intrinsic input node is presented in Fig. 27e) and f). As a result of summing the IM3 currents of the nonlinear sources seen at the input ($Q_{GS-V_{GS}}$ and $Q_{GD-V_{GD}}$) large linear terms of $C_{GD-V_{GD}}$ and $C_{GS-V_{GS}}$ sources can be seen. These are amplifying the IM3 present at the corresponding controlling voltages. A considerable amount of IM3 is generated only by the $C_{GS-V_{GS}}$. The analysis is quite different when calculating the voltage response of IM3 contributions of each nonlinear source at the input. The total IM3 is generated mainly by the $Q_{GS-V_{GS}}$ source and $I_{DS-V_{GS}-V_{DS}}$ source, which is surprisingly large. In fact, the IM3 caused by the $I_{DS-V_{GS}-V_{DS}}$ source is actually fed back to the input and dominates the IM3 in both the input and output of the device.

7 Test cases

In this chapter the spectral based fitting technique and the simplified Volterra analysis implemented in the APLAC circuit simulator is applied for detailed distortion analysis. In APLAC quite flexible simulations can be made and hence the proposed technique is able to provide very interesting information about the nonlinear behaviour of the RF PAs. Two different test benches are used, one being 30 W LDMOS PA based on the MET model that models MRF21030 RF power transistor and the other 1 W HBT PA based on the VBIC model that models the InGap HBT power IC device. After introducing the test benches the extension of the spectral based fitting technique to include the thermal effects is discussed. Then, detailed distortion analysis is used to analyse the causes of IMD sweet spot in LDMOS PA as well as the AM-AM and AM-PM. Furthermore, the detailed distortion analysis of HBT PA for bandwidth dependent memory effects is discussed and finally impedance optimization of the corresponding PA is performed and analysed in detail.

7.1 Test benches

7.1.1 30W LDMOS PA based on MET model

A test bench for a complete amplifier using Freescale's MET model that corresponds the MRF21030 LDMOS power transistor was constructed in APLAC based on the schematic shown in [73]. The corresponding PA is designed for an output stage of WCDMA base station. The picture of the amplifier is shown in Fig. 28 and the schematic of the corresponding PA used in APLAC is presented in Appendix 1.

MRF21030 is an internally matched device and the internal matching is included to the simulation model. Fortunately, in APLAC the intrinsic MET model and the package including the internal matching can be separated as shown in Appendix 1. It is then possible to access the internal model shown in Fig. 11 by knowing the names of internal nodes and branches. However, these are not documented but can be obtained from the APLAC support. Also, transit time under the gate of the model is needed for successfully calculating

the 2-dimensional g_m -element. Therefore access to the model parameters is required. However, device parameters of the MET model are encrypted, but, fortunately, the device parameters of the MRF21030 transistor model were obtained directly from Freescale.

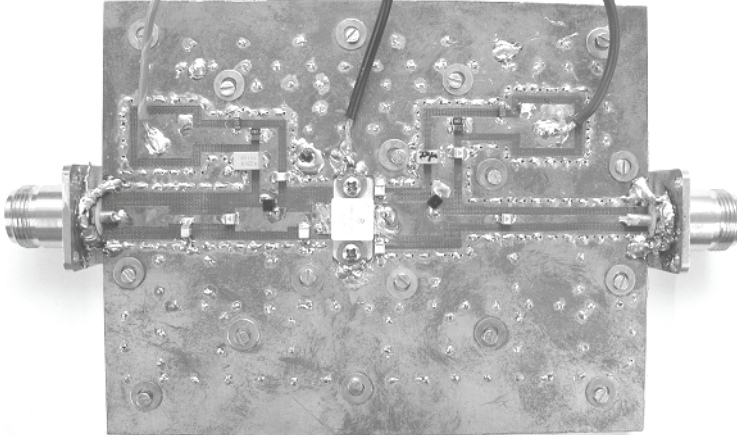


Fig. 28. Test board of 30 W LDMOS PA based on MRF21030.

7.1.2 HBT PA based on VBIC model

The test bench of HBT amplifier was designed to obtain a reasonably wideband response at 2 GHz. The input and output matching network and the bias lines of the amplifier are designed on a 50 ohm microstrip using discrete components. The input has a T-matching network and the output has two grounded capacitors in parallel and a DC-block. Large capacitors are used to block RF at the bias lines and 39 nH inductors are used to connect the bias lines to the matching networks. A 500 ohm series resistor at the base bias is used to reduce the $V_{BEQ} - I_{CQ}$ sensitivity. The HBT device itself is bonded to PWC and is a Global Communication Semiconductors' power InGaP HBT P1 process [74] consisting of four parallel HBTs with base ballast circuits. The amplifier is shown in Fig. 29 and the corresponding test bench used in APLAC is presented in Appendix 2.

Modelling InGaP HBT devices using the VBIC model has been addressed in [75], where several simplifications are suggested. First, the npn HBT does not contain a parasitic pnp transistor, which allows R_S , I_{BCP} , I_{CCP} , I_{BEO} and Q_{BCP} to be removed from the complete VBIC model shown in Fig. 12. Second, due to a low value of R_B the base of the HBT can be considered non-distributed and therefore Q_{BEX} and I_{BEX} can be dropped out. Third, there are no direct methods to extract R_C and Q_{BCX} and also the calculation of R_{C1} and Q_{BCX} does not take into account the so-called push-out effect. Therefore Q_{BCX} is dropped. The VBIC model for a HBT device is presented in Fig. 30 in which the non-modelled elements are shown in grey. Of the remaining elements, R_{C1} , C_{BCO} , C_{BEO} and I_{EPI} are considered linear, while the rest are considered nonlinear.

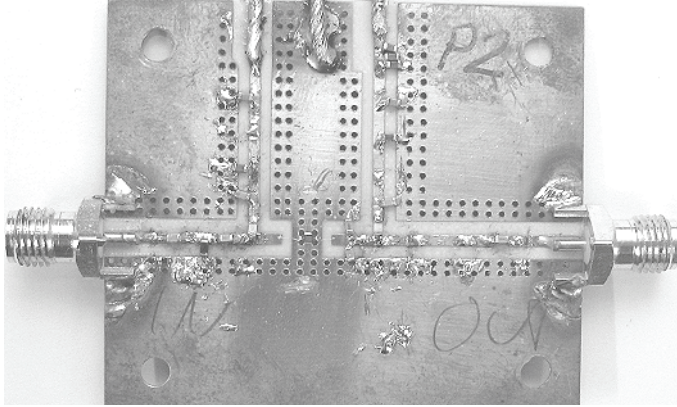


Fig. 29. Test board of HBT PA.

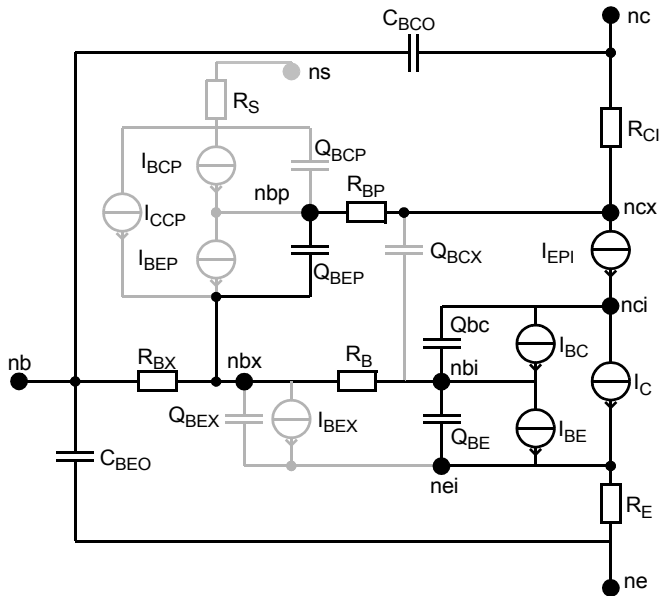


Fig. 30. Equivalent circuit of the VBIC model for a HBT device.

Since the spectral fitting is based on the large-signal controlling voltage and output current spectra of each nonlinear source, we need to have access to the internal nodes and branches of the VBIC model. These are by default not available, but AWR-APLAC kindly offered a revised version of the model with access to the internal nodes and branches. The model parameters for InGap HBT were obtained from the manufacturer with the actual devices from P1 and P2 processes. As mentioned above, the original model contains four parallel devices including the base ballasting networks. These were lumped together for simulation purposes into a single device with a parallel R-C ballast network.

The VBIC model has two 2-dimensional sources as mentioned in Section 3.2.1: the I_C -

$V_{BE}-V_{BC}$ I-V source and $Q_{BE}-V_{BE}-V_{BC}$ Q-V source. 2-dimensional Q_{BE} depends strongly on V_{BC} , which is due to the fact that V_{BC} is a strong function of large base transit time. It is important to note that unlike to AC analysis DC analysis does not take transit time into account, which results in different C_{BE} values. This might cause confusion and result in fitting difficulties if the matter is not recognized. The nature of Q_{BE} is discussed in detail in Paper VIII. Also the modelling of HBT using the VBIC model is discussed there.

7.2 Extending the spectral based fitting to cope with thermal effects

As mentioned in Section 2.2.5, self-heating may cause memory effects. Therefore thermal effects need to be taken into account in the spectral based fitting as well. The junction temperature t_j , which is time varying, is caused by self heating. The spectrum of the temperature variations can be calculated by

$$T_j(f) = P_{DISS}(f) \cdot Z_{TH}(f) , \quad (33)$$

where Z_{TH} is the thermal impedance described in Section 2.2.5 and P_{DISS} is the dissipated power. In the MET model the complete form of $P_{DISS}(f)$ can be described by

$$\begin{aligned} P_{DISS}(f) = & V_{DS}(f) \otimes I_{DS}(f) + V_{RG}(f) \otimes I_G(f) \\ & + V_{RD}(f) \otimes I_D(f) + V_{RS}(f) \otimes I_S(f) , \end{aligned} \quad (34)$$

where V_{RX} is the spectrum of the voltages across the terminal resistances. Since two 1st-order signals are convolved together P_{DISS} always includes 2nd-order components [20].

The access to the thermal node $T_j(f)$ of the MET model was directly available. Therefore, the thermal effects can be included to the fitted model simply by adding the corresponding temperature related terms of (4) shown in Section 4.2 to the frequency domain polynomial model. The temperature effects are included only in the 2-dimensional g_m -element and hence the complete model can be written by

$$\begin{aligned} I(f) = & K_{100} \cdot V_{10}(f) + 2K_{200} \cdot V_{ENV}(f) + 2K_{200} \cdot V_{H2}(f) \\ & + K_{300} \cdot V_{30}(f) + \dots \\ & + K_{010} \cdot V_{01}(f) + 2K_{020} \cdot V_{ENV}(f) + 2K_{020} \cdot V_{H2}(f) \\ & + K_{030} \cdot V_{03}(f_{IM3}) + \dots \\ & + K_{110} \cdot V_{11}(f) + K_{210} \cdot V_{21}(f) + K_{120} \cdot V_{12}(f) + \dots \\ & + K_{001} \cdot T(f) + K_{101} \cdot T(f) \otimes V_{10}(f) + K_{011} \cdot T(f) \otimes V_{01}(f) + \dots \end{aligned} \quad (35)$$

The higher order temperature related terms are obtained by convolving $T_j(f)$ with the corresponding controlling voltages. This is also presented in Paper IV.

As shown in Fig. 11 the thermal circuit of the MET model consists of a parallel resistor (RTH) and a large capacitor (CTH) constituting a large time constant ($\tau \sim 15 - 20$ s). In Paper IV it is shown that by using the default values of the thermal circuit the MET model is capable of modelling the correct DC temperature but the other thermal effects are negligible as the large CTH shorts everything but DC. Therefore, when including temperature related terms to the spectral fitting the fitting matrix becomes singular as $T_j(f) \otimes V_{10}(f) \sim V_{10}(f)$, for example. If τ is decreased from 15 s to 15 ns, the temperature effects seen at IM3 are still relatively small.

However, it is well known that FET devices exhibit quite small temperature effects, but only one and very large time constant is not enough for accurate modelling of the self-heating effects. Unfortunately, simulation models usually contain only one time constant. Such a simple thermal model is usually preferred in the simulation models since self-heating introduces a nonlinear feedback loop that can ruin numerical convergence [76], [77]. Since simulated self-heating effects in both MET model and VBIC model are negligible they are excluded from the fitting procedure in this thesis except for the simulation examples shown in Paper IV.

7.3 IMD sweet spot analysis

One way to improve the linearity of RF PAs has been to exploit the so-called sweet spots, where the linearity is better than in their immediate vicinity. Sweet spots occur at certain input amplitudes and bias points. In general, sweet spots are localized by a 2-tone test but as it is shown in [18], even a multi-tone signal is capable of predicting sweet spots, which is an important result for practical high efficiency and linear PA designs.

The causes of sweet spots have been studied already by several authors [59], [78]-[80]. These papers are mostly based on symbolic Volterra analysis and utilize different ways to derive the nonlinearity coefficients. However, they all share the following simplifications: First, most papers discuss only the nonlinearities caused by the input voltage. Second, none of the papers addresses the effects of nonlinear capacitances. Third, all the papers assume a non-distorted input signal. These simplifications are necessary for hand analysis, but unfortunately they also affect the conclusions that can be drawn from the analysis.

The detailed analysis of sweet spots is presented in Paper VII in which it is shown that IMD sweet spot in LDMOS PA is a result of a vector sum of several cancelling mechanisms. However, a couple of remarks should be pointed out from the analysis shown in Paper VII. First, the analysis is based on the simplified Volterra analysis in which the currents from the sources seen at the output are summed. Thus the effect of $Q_{GS}-V_{GS}$ for example, cannot be seen directly but is lumped in the linearly transmitted portion of the nonlinear sources seen at the output. Due to the selected presentation the linear term of $Q_{DS}-V_{DS}$, for example, is significant. Second, in the analysis presented in Paper VII the 3rd-degree cross-terms are removed from the model of $I_{DS}-V_{GS}-V_{DS}$ source to reliably fit the model using a normal 2-tone input signal. However, by using more reliable characterization techniques that also enable cross-terms reliably fitted they seem to have a significant impact on the IM3 at the sweet spot. Altogether, the detailed analysis of IMD sweet spots of LDMOS PA is repeated here but for a different sweet spot and in more detail.

7.3.1 Locating the sweet spot

The sweet spots are found by simulating a normal 2-tone power sweep with different DC bias currents (I_{DQ}). In Fig. 31 the simulated IM3L as a function of input power with different I_{DQ} values are shown. It can be seen that, first, the linearity increases (i.e., IM3 decreases) by increasing the bias current I_{DQ} but then linearity starts to decrease when I_{DQ} is greater than 320 mA. One and the most obvious sweet spot occurs at $I_{DQ} = 320$ mA and $P_{IN} = 11$ dBm. Another sweet spot occurs at $I_{DQ} = 300 - 320$ mA and $P_{IN} = 15$ dBm. The analysis of the latter sweet spot is presented in Paper VII. Therefore the detailed analysis of the sweet spot at $P_{IN} = 11$ dBm is presented here.

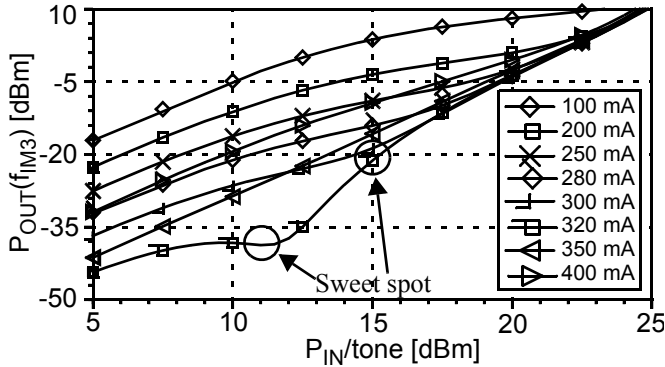


Fig. 31. IM3L as a function of P_{IN} with different DC bias currents (I_{DQ}).

7.3.2 Detailed distortion analysis of the sweet spot

Now a detailed analysis of IM3 behaviour of the sweet spot is presented. The IM3 generated by the nonlinear sources are calculated as IM3 voltages to the terminal nodes. In the analysis the I_{DS} - V_{GS} - V_{DS} source and Q_{GS} - V_{GS} source is analysed in detail. In addition, the overall distortion at the gate and drain node is analysed from which also the effect of the rest of the Q-V sources (Q_{GD} - V_{GD} and Q_{GS} - V_{GS}) can be studied. The IM3 contributions of the nonlinear sources are denoted similarly as in Section 6.2. The general form is $V(K_n \cdot V_n)$, which indicates the voltage of the corresponding IM3 contribution. K_n denotes the coefficient of nth-degree nonlinearity, and V_n denotes the corresponding convolved voltage. For example, the 3rd-degree term of the I_{DS} - V_{GS} nonlinearity is denoted as $K_{30} \cdot V_{i3}$, corresponding to cubic nonlinear term $K_{30} \cdot V_{GS}^3$.

7.3.2.1 I_{DQ} sweep

The IM3 contributions at the gate node as a function of I_{DQ} are presented in Fig. 32a). It can be seen that the total IM3 from the Q-V sources, denoted as $V(Q_{DS})$, $V(Q_{GS})$ and

$V(Q_{GD})$ are not strongly bias dependent. The IM3 mainly caused by the I_{DS} - V_{GS} - V_{DS} source ($V(I_{DS})$) is fed back to the gate and is highly bias dependent and shows a sweet spot at $I_{DQ} = 325$ mA. $V(I_{DS})$ is clearly dominating the IM3 at the gate but when $V(I_{DS})$ shows a dip at $I_{DQ} = 325$ mA $V(Q_{GS})$ becomes larger than $V(I_{DS})$. These two sources dominate the IM3 at the gate while $V(Q_{DS})$ and $V(Q_{GD})$ remain small. Tot is the sum of the contributions and matches well with the data simulated using HB. It is interesting to note that the total IM3 at the gate does not follow the shape of $V(I_{DS})$. Instead, at the gate the sweet spot appears at $I_{DQ} = 360$ mA, which is caused by the cancellation between $V(I_{DS})$ and $V(Q_{GS})$.

In Fig. 32b) a similar presentation is shown for the drain node. Again, it can be seen that the IM3 generated by the I_{DS} - V_{GS} - V_{DS} source ($V(I_{DS})$) is bias dependent and produces a steep minimum at $I_{DQ} = 325$ mA, and is therefore the main contributor to the sweet spot. However, at the sweet spot the total IM3 at the drain (Tot) is steeper and occurs also at $I_{DQ} = 325$ mA. The sweet spot is, in fact, caused by the cancellation between $V(I_{DS})$, $V(Q_{GS})$ and also $V(Q_{DS})$, as will be shown later on.

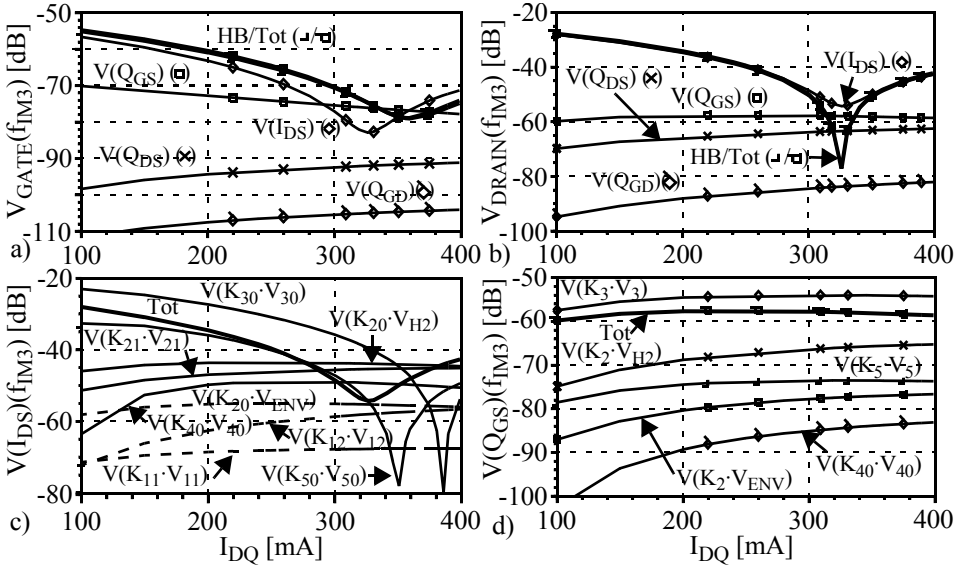


Fig. 32. Total IM3 at the a) gate and b) drain node vs. I_{DQ} . IM3 contributions of c) I_{DS} - V_{GS} - V_{DS} and d) Q_{GS} - V_{GS} sources at the drain node vs. I_{DQ} .

A more detailed insight of the IM3 of I_{DS} - V_{GS} - V_{DS} and Q_{GS} - V_{GS} sources is presented in Fig. 32c) and d), respectively. The least significant terms in Fig. 32c) are removed or shown as dashed lines.

At low I_{DQ} values the 3rd-degree nonlinear term $V(K_{30} \cdot V_{30})$ in Fig. 32c) is dominating the total IM3 of the I_{DS} - V_{GS} - V_{DS} source. Also the 5th-degree term $V(K_{50} \cdot V_{50})$ is large. However, these odd-degree terms are highly bias dependent and decrease dramatically as the I_{DQ} increases while the even-order terms do not depend strongly on I_{DQ} . $V(K_{50} \cdot V_{50})$ and $V(K_{30} \cdot V_{30})$ produce steep minima at $I_{DQ} = 350$ mA and $I_{DQ} = 385$ mA, respectively.

These minima occur when coefficients K_{30} and K_{50} change sign. However, it is interesting to note that the sweet spot caused by the $I_{DS}-V_{GS}-V_{DS}$ source is located at $I_{DQ} = 325$ mA, and not where K_{30} is zero nor where 3rd and 5th-degree nonlinear terms $V(K_{50} \cdot V_{50})$ and $V(K_{30} \cdot V_{30})$ cancel one another at $I_{DQ} = 375$ mA. In fact, the contributions $V(K_{20} \cdot V_{H2})$ (which is mixed down to IM3 from the 2nd harmonic band) and the 3rd-degree cross-term $V(K_{21} \cdot V_{21})$ become as big as $V(K_{30} \cdot V_{30})$ but their phases are opposite to $V(K_{30} \cdot V_{30})$, which causes cancellation. Also $V(K_{50} \cdot V_{50})$ and $V(K_{40} \cdot V_{40})$ are big enough to affect the cancellation. Cancelling mechanisms mentioned in this presentation are easier to see from a vector plot, as will be shown in the next section.

The IM3 contributions of $Q_{GS}-V_{GS}$ source as functions of I_{DQ} at the drain node are presented in Fig. 32d). It can be seen that the IM3 contributions are not strongly bias dependent but increase steadily as a function of I_{DQ} . 3rd-degree nonlinearity $V(K_3 \cdot V_3)$ is dominating the total IM3 of $V(Q_{GS})$. 2nd-degree nonlinearity $V(K_{20} \cdot V_{H2})$ that is mixed down to IM3 from the 2nd harmonic band has the opposite phase to $V(K_3 \cdot V_3)$ but its magnitude is not large enough to affect the IM3 significantly.

7.3.2.2 Phasor presentation

In this section the sweet spot is analysed using the phasor presentation. The vector plot of the contributions of IM3 voltage at the gate and drain node as well as the IM3 contributions of $I_{DS}-V_{GS}-V_{DS}$ and $Q_{GS}-V_{GS}$ source at the drain node are presented in Fig. 33a) - d), respectively. This analysis is performed at the sweet spot, i.e. $P_{IN} = 11$ dBm and $I_{DQ} = 325$ mA. In Fig. 33 the same contributions can be seen as in Fig. 32. The only difference is that now the contributions are presented as vectors enabling the cancelling mechanisms to be visualized. Insignificant contributions are not shown. The result vectors (Tot) at the gate and drain nodes in Fig. 33a) and b) match well with the simulations using HB. This indicates that the vector sum is correct.

The vector plot at the gate node is shown in Fig. 33a). As mentioned above, $V(I_{DS})$ and $V(Q_{GS})$ are controlling the IM3 at the gate. Also $V(Q_{DS})$ is noticeable and affects the IM3. The total IM3 voltage at the gate is caused by the vector sum of these sources. It was noted above that the sweet spot is not seen simultaneously at the gate and drain, and as it can be seen, there is no such strong cancellation at the gate that would cause sweet spot at $I_{DQ} = 325$ mA.

In the drain node shown in Fig. 33b) the IM3 caused by $V(I_{DS})$ is large and in opposite direction than the IM3 caused by $V(Q_{GS})$ and $V(Q_{DS})$. These three total IM3 contributions cancel each other almost completely resulting in a small total IM3. The reason for such a large $V(Q_{GS})$ and especially $V(Q_{DS})$ is because $V(I_{DS})$ is small in the sweet spot region and thus $V(Q_{GS})$ and $V(Q_{DS})$ become more dominating. At the drain the effect of $V(Q_{GD})$ is negligible and therefore not shown.

The vector plot of $I_{DS}-V_{GS}-V_{DS}$ source at the drain node is shown in Fig. 33c) where it can be seen that the result vector (Tot) is small compared with the magnitudes of other vectors. $V(K_{30} \cdot V_{30})$ is large as well as $V(K_{20} \cdot V_{H2})$ and $V(K_{21} \cdot V_{21})$. However, the phases of $V(K_{20} \cdot V_{H2})$ and $V(K_{21} \cdot V_{21})$ are opposite to $V(K_{30} \cdot V_{30})$, which results in cancellation. This is the reason that causes the sweet spot at this bias. Also $V(K_{50} \cdot V_{50})$, $V(K_{40} \cdot V_{40})$,

$V(K_{12} \cdot V_{12})$ and $V(K_{20} \cdot V_{2ENV})$ cause cancellation. As a result, at the sweet spot the total IM3 voltage of the $I_{DS} \cdot V_{GS} \cdot V_{DS}$ source is small. Without this kind of phasor presentation the cancellation cannot be seen.

The cancelling $V(K_{20} \cdot V_{H2})$ term is mixed down to IM3 from the 2nd harmonic band at the gate. $V(K_{20} \cdot V_{H2})$ depends on the impedances of the matching network at the second harmonic, and hence is sensitive to frequency variations. As the sweet spot is caused by such a strong cancellation, small changes in the 2nd harmonic impedances have a strong effect to the total IMD at the sweet spot.

The 3rd-degree nonlinear term $V(K_3 \cdot V_3)$ is dominating the IM3 of $Q_{GS} \cdot V_{GS}$ source seen at the drain in Fig. 33d). $V(K_2 \cdot V_{H2})$ and $V(K_5 \cdot V_5)$ are rather small compared with $V(K_3 \cdot V_3)$ but still cause little cancellation. These three contributions dominate the IM3 of this source.

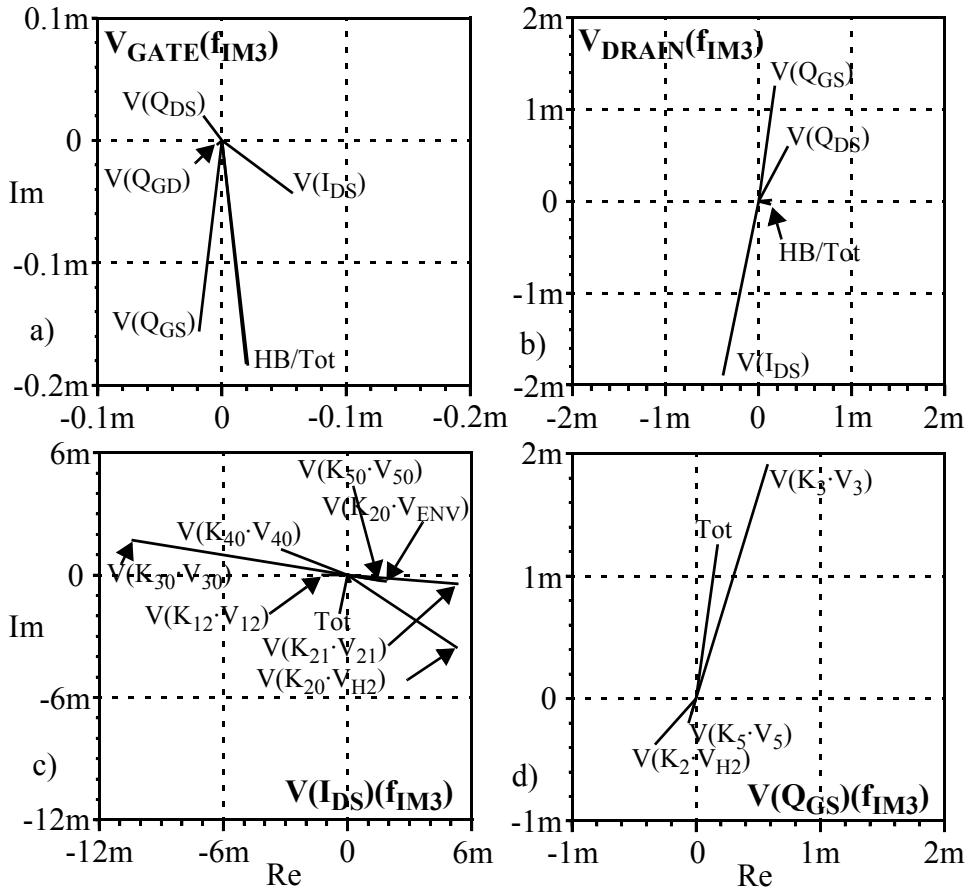


Fig. 33. Phasor presentation of the total IM3 contributions at the a) gate and b) drain node and IM3 contributions of c) $I_{DS} \cdot V_{GS} \cdot V_{DS}$ and d) $Q_{GS} \cdot V_{GS}$ sources at the drain node.

7.4 AM-AM and AM-PM analysis

In this section the AM-AM and AM-PM of the LDMOS PA is analysed in detail. The main motivation of the analysis presented here is to show that the spectral based fitting and simplified Volterra analysis method can easily be extended for detailed distortion analysis of the fundamental tone. As explained in Section 2.1.2, the AM-AM and AM-PM are characterized by applying a 1-tone signal with varying amplitude to the PA and observing the amplitude and phase response of the fundamental tone at the output. However, since the spectral fitting and detailed distortion analysis are implemented for a 2-tone test signal, the easiest way for 1-tone analysis using the proposed technique is to decrease the other tone by, for example, 40 dB and perform the detailed analysis using the other tone. The LDMOS PA is biased in class AB ($I_{DQ} = 300$ mA), in which the fundamental tone contains only little distortion. The measured frequency for 1-tone measurements were chosen at the centre of the pass band, $f_0 = 2.14$ GHz.

7.4.1 Measured results

The measured results of AM-AM and AM-PM of the corresponding PA are already presented in Fig. 3. However, the analysis shown here cannot be performed with as high input amplitude level as measured in Fig. 3 for a couple of reasons. First, the spectral fitting is applied only up to the 5th-degree and at high amplitudes higher-degree nonlinearities should be taken into account as well. Second, at high amplitudes the spectral fitting of $I_{DS} - V_{GS} - V_{DS}$ source results in large but mutually cancelling 2nd- and 3rd-degree cross-terms that cause non-physical curvature in the I-V curves, as explained in Paper V. Third, AM-PM was measured with NWA with CW mode enabling steady state for each power level. In addition, the measurement setup was calibrated for each power level. However, this setup could not be applied for high amplitudes due to the limited input power and DC current of the test system. As a result the AM-AM and AM-PM analysis presented here is limited below $P_{IN} = 25$ dBm.

The measured results were compared with the HB simulations and are presented in Fig. 34. It can be seen that the measured and simulated AM-AM match within 0.5 dB, which is a good result. The fundamental tone does not reach the compression but remains in the linear region. From Fig. 3 it can be seen that the 1 dB compression point of the LDMOS PA biased in class AB is around $P_{IN} = 30$ dBm. The AM-AM presented in Fig. 34 was measured with a spectrum analyser using a normal power sweep.

The measured and simulated AM-PM, however, do not agree as well as AM-AM. Nevertheless, measured and simulated AM-PM have similar shape and match well up to $P_{IN} = 20$ dBm. At a low input power the AM-PM is negligible and the output phase begins to deviate after $P_{IN} = 15$ dBm. As a result of the power sweep measurements show AM-PM of around 9 degrees while the simulations predict AM-PM to be less than 4 degrees. Therefore it seems that the MET model is not capable of predicting AM-PM very accurately.

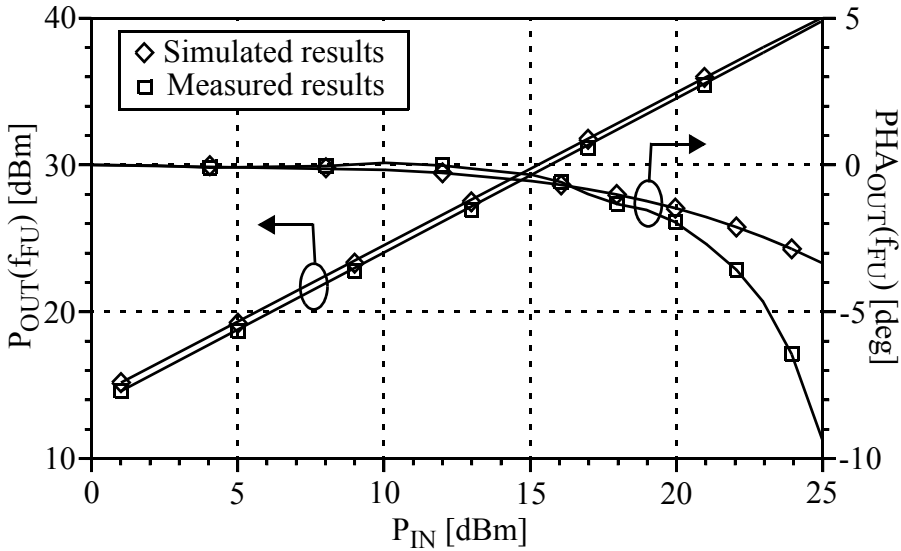


Fig. 34. Measured and simulated AM-AM and AM-PM of LDMOS PA.

7.4.2 Detailed analysis of AM-AM and AM-PM

In this section the detailed analysis of AM-AM and AM-PM is performed using the simulation test bench of the LDMOS PA. The polynomial model is characterized by first using 1-tone input - 1-tone output setup and fitting I_{DS} - V_{GS} - V_{DS} source and then using a normal 2-tone setup and fitting the Q-V sources and calculating the simplified Volterra analysis. The difference is that now the fundamental tone is analysed and the other tone is decreased by 40 dB.

The fundamental tone at the output is mainly linearly amplified since the PA is biased in moderate class AB and thus little affected by the nonlinearities of the device. This results in some difficulties in analysing the fundamental tone. If the distortion contributions are plotted as currents, the effect of input nonlinearities like Q_{GS} - V_{GS} , for example, cannot be seen at the output. In addition, the linear contributions of the sources are substantial and able to hide the distortion contributions. On the other hand, if the nonlinear currents are calculated as voltages to the selected node, only distortion contributions are obtained but not the linear ones. Fortunately, the total fundamental tone is obtained from the HB simulation for reference. In addition, now all the sources can be included to the analysis and the distortion at the fundamental tone is more illustrative. Both analysis techniques were tested and as a result the latter technique seemed to be more suitable for the analysis.

7.4.2.1 Power sweep

In this section the magnitude and phase of the distortion contributions of the fundamental tone as a function of input amplitude is analysed. The simulation results are presented in Fig. 35. The phase of the input signal was set to zero at the gate at the beginning of the sweep and spectral fitting and detailed analysis is calculated for each power level. Contributions are denoted similarly as in Section 7.3. It can be seen in Fig. 35 that the detailed analysis provides a lot of information. Therefore only the essential pieces of information are analysed.

The magnitude of the distortion contributions of the total fundamental tone at the gate node is presented in Fig. 35a). It can be seen that the total distortion (Tot) has little effect to the total fundamental tone (HB) since Tot is almost 50 dB smaller than HB. At small power levels the distortion caused by the I_{DS} - V_{GS} - V_{DS} source ($V(I_{DS})$) that is fed back from the drain to the gate dominates the distortion at the gate. However, as the input power increases, $V(I_{DS})$ clearly decreases and the distortion caused by the Q_{GS} - V_{GS} source ($V(Q_{GS})$) becomes dominant. The total distortion also slightly decreases at high amplitudes due to the decrease of $V(I_{DS})$. The phases of the corresponding contributions at the gate are shown in Fig. 35b), where only small AM-PM (~ 2 degrees) can be seen in the total fundamental tone (HB). The total AM-PM of the distortion contributions are also quite small and mainly caused by the $V(Q_{GS})$ and $V(I_{DS})$. The phase of the $V(I_{DS})$ changes by almost 100 degrees from $P_{IN} = 15$ dBm to $P_{IN} = 25$ dBm but its effect to total AM-PM is small since a larger magnitude $V(Q_{GS})$ compensates the effect of $V(I_{DS})$.

A similar presentation for the magnitude and phase of the distortion contributions at the drain node is presented in Fig. 35b) and c), respectively. At the drain $V(I_{DS})$ is more dominant but again as the input power increases, $V(I_{DS})$ decreases. $V(Q_{GS})$ is surprisingly large at the drain and it becomes dominant as $V(I_{DS})$ decreases. The magnitudes of $V(I_{DS})$ and $V(Q_{GS})$ are equal around $P_{IN} = 20$ dBm but their phases are the opposite and thus cancel one another. Due to this cancellation the total distortion (Tot) of the fundamental tone shows a sweet spot at $P_{IN} = 19.5$ dBm. It can also be seen from Fig. 35d) that the total AM-PM at the drain (HB) is less than 4 degrees but the AM-PM of the total distortion (Tot) is more than 130 degrees. However, since Tot is more than 40 dB smaller than HB, it is able to cause a small AM-PM to the total fundamental tone only. As noted above, the phase of $V(I_{DS})$ is changing by almost 100 degrees and it seems at this point that it is the main cause of AM-PM.

A more detailed insight of the distortion of the fundamental tone caused by I_{DS} - V_{GS} - V_{DS} source at the drain node is presented Fig. 35e) and f) for magnitude and phase, respectively. It can be seen that the distortion is dominated by the 3rd-degree nonlinearity ($V(K_{30} \cdot V_{30})$). As the amplitude increases, $V(K_{20} \cdot V_{H2})$ and $V(K_{21} \cdot V_{21})$ become more dominant while $V(K_{30} \cdot V_{30})$ slightly compresses. As a result the total distortion begins to decrease above $P_{IN} = 15$ dBm where also the total phase begins to deviate. However, there is no direct reason for the large phase and magnitude change of the total distortion since the distortion contributions and therefore also coefficients are not strongly amplitude dependent. Such a result is clearly caused by the sum of small changes in the distortion contributions of the I_{DS} - V_{GS} - V_{DS} source. For this reason the distortion behaviour is analysed next using phasor presentation with different power levels.

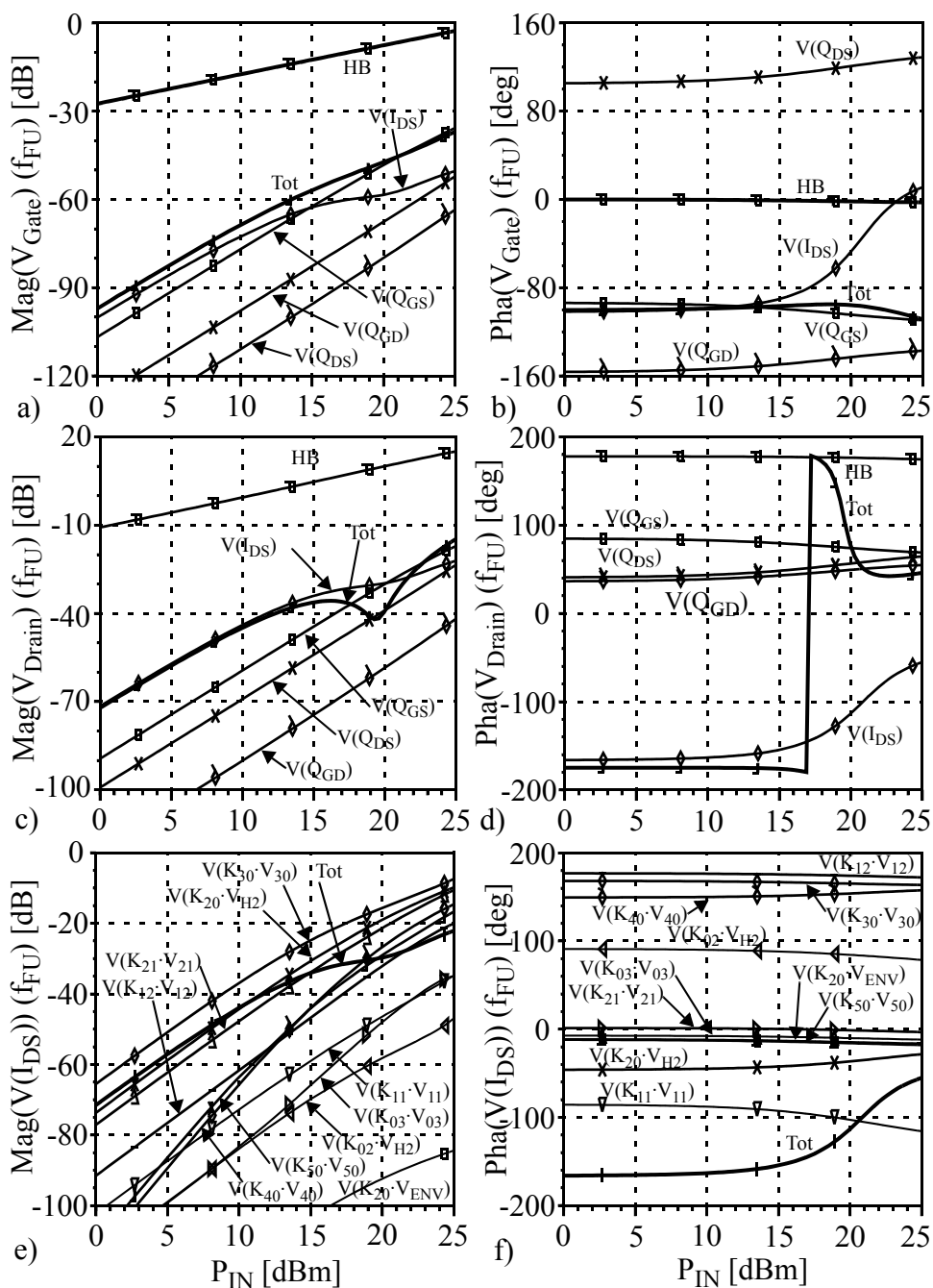


Fig. 35. a) Magnitude and b) phase of the fundamental tone at the gate, c) magnitude and d) phase at the drain and e) magnitude and f) phase of the distortion contributions of the I_{DS} - V_{GS} - V_{DS} source of the fundamental tone at the drain vs. P_{IN} .

7.4.2.2 Phasor presentation

It is difficult to draw conclusions based on the presentation shown in the previous section that is not very illustrative. Therefore, in this section the distortion contributions of the fundamental tone are presented as a vector sum at the drain node for total distortion as well as the distortion caused by the I_{DS} - V_{GS} - V_{DS} source. The analysis is performed for three different power levels: $P_{IN} = 15$ dBm, $P_{IN} = 19.5$ dBm and $P_{IN} = 25$ dBm and the results are shown in Fig. 36.

Fig. 36a), c) and e) show the total distortion of the fundamental tone at the drain with different power levels. They have been scaled for better insight to the distortion contributions. Therefore the magnitude of the total fundamental tone (HB) is not seen but, what is more important, the direction of HB is. It can be seen from Fig. 36a) that at $P_{IN} = 15$ dBm $V(Q_{GS})$ is perpendicular to HB and is, in fact, causing the total AM-PM. However, $V(I_{DS})$ is also large and as a result of the vector sum of $V(Q_{GS})$ and $V(I_{DS})$ the result vector (Tot) is causing expansion to the fundamental tone. At $P_{IN} = 19.5$ dBm shown in Fig. 36c) the $V(Q_{GS})$ is in the same direction as in Fig. 36a) but now the $V(I_{DS})$ is at the opposite direction to $V(Q_{GS})$, which results in strong cancellation. This is the main reason for the sweet spot seen in Fig. 35c). The total distortion (Tot) of the fundamental tone is almost perpendicular to HB and thus causes only AM-PM. However, the AM-PM caused by $V(Q_{GS})$ would be larger but due to the cancellation this effect is minimized. At $P_{IN} = 25$ dBm shown in Fig. 36e) the phase of $V(I_{DS})$ is rotated by almost 100 degrees from $P_{IN} = 15$ dBm while the rest of the contributions are more or less in the same direction. The total distortion is still dominated by $V(I_{DS})$ and $V(Q_{GS})$ but now the cancellation is not so strong as $V(I_{DS})$ is rotated. As a result the total distortion (Tot) of the fundamental tone causes not only AM-PM but also gain compression to the total fundamental tone. The behaviour presented above is mainly caused by the rotating $V(I_{DS})$, as noted in the previous section.

A more detailed vector plot of the I_{DS} - V_{GS} - V_{DS} source at the drain node is presented in Fig. 36b), d) and f) for $P_{IN} = 15$ dBm, $P_{IN} = 19.5$ dBm and $P_{IN} = 25$ dBm, respectively. As noted above, $V(K_{30} \cdot V_{30})$ is dominating the distortion of the source but $V(K_{20} \cdot V_{H2})$ and $V(K_{21} \cdot V_{21})$ are also large. However, as it can be seen, they are in the opposite phase and cause cancellation. This cancellation results in small total distortion compared with the magnitudes of the distortion contributions. It can be seen from Fig. 36b), d) and f) that the directions of the distortion contributions do not change much at different power levels indicating that the coefficients are not strongly amplitude dependent. However, the phase of the total distortion is changed by almost 100 degrees from $P_{IN} = 15$ dBm to $P_{IN} = 25$ dBm. The reason for this is that cancelling vectors $V(K_{20} \cdot V_{H2})$ and $V(K_{21} \cdot V_{21})$ become larger than $V(K_{30} \cdot V_{30})$ above $P_{IN} = 20$ dBm. In addition, the $V(K_{20} \cdot V_{H2})$ shows a phase shift of 15 degrees which also causes better cancellation and thus AM-PM to the total distortion of $V(I_{DS})$. $V(K_{20} \cdot V_{H2})$ is the second degree nonlinear term that is mixed to the fundamental tone from the 2nd harmonic band. Therefore it is dependent on the transfer function of the second harmonic which, in fact, exhibits also 15 degrees of phase shift as a function of input amplitude. Therefore the AM-PM of the fundamental tone is also affected by the AM-PM of the second harmonic.

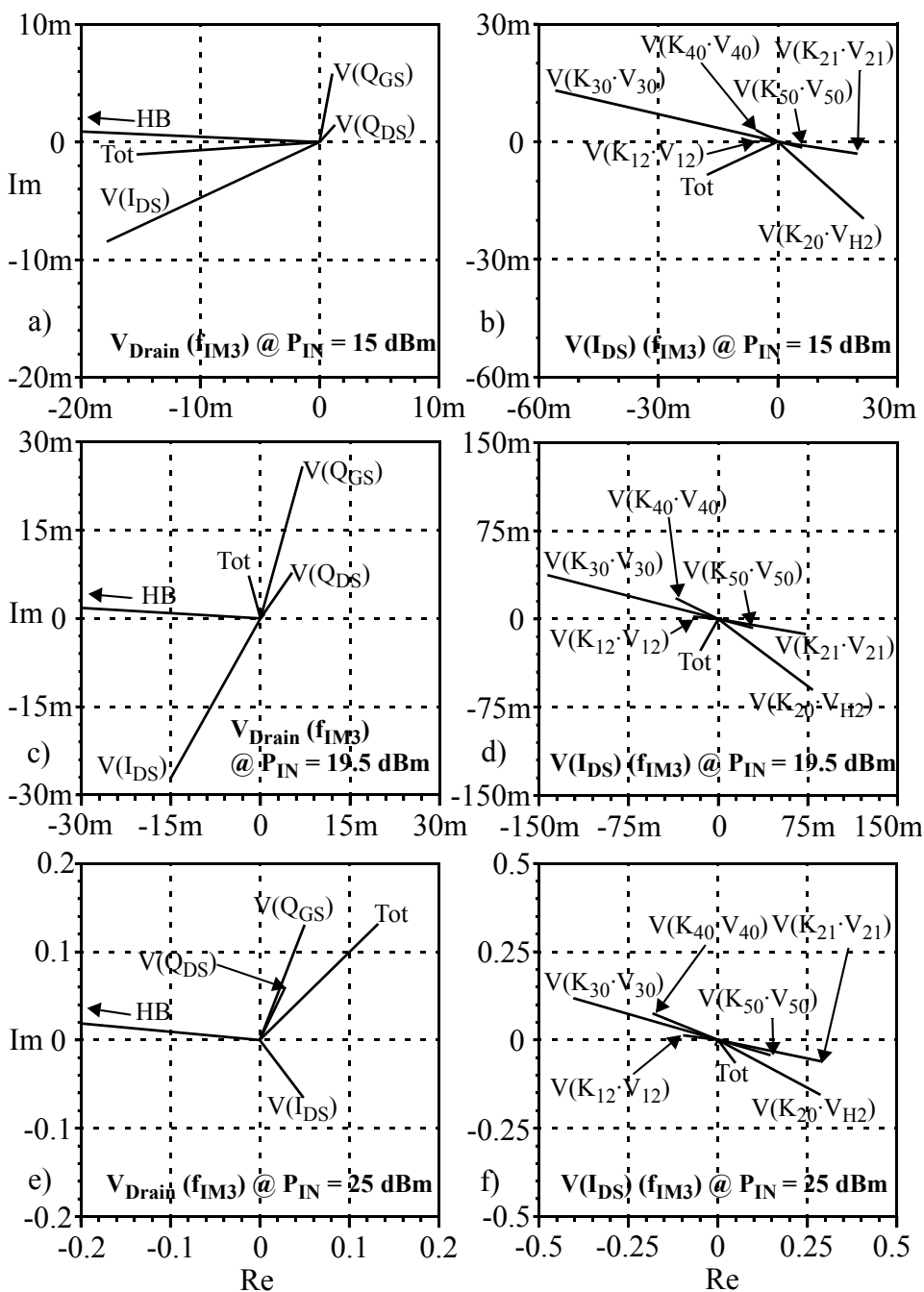


Fig. 36. Phasor presentation of the total distortion of the fundamental tone at the drain and distortion contributions at the drain node of the I_{DS} - V_{GS} - V_{DS} source at three different power levels ($P_{IN} = 15$ dBm, $P_{IN} = 19.5$ dBm and $P_{IN} = 25$ dBm).

7.5 Analysing the bandwidth dependent memory effects

The next step to evaluate the spectral based fitting and simplified Volterra analysis method is to study the bandwidth dependent memory effects. The principle of this analysis is discussed in Section 2.2. The bandwidth dependent memory effects are characterized using a 2-tone test with varying tone spacing (Δf) as it can simulate the broadband signal and reveal bandwidth dependencies such as low-frequency resonances that can cause memory effects to IM3 by mixing up to IM3 via 2nd-degree nonlinearity.

The analysis is performed by using HBT PA presented in Section 7.1.2 and the detailed analysis of the corresponding PA is, in fact, presented in Paper VIII. Therefore the results are not repeated here. Simulated IM3 as a function of Δf of the corresponding HBT PA is also presented in Fig. 9 in Section 2.2.4. The corresponding IM3 response is different than the results shown in Paper VIII due to a different power level and bias point, but, shows similar behaviour, nonetheless.

As seen in the measured and simulated results in Paper VIII and in Section 2.2.4 the IM3 drops significantly between $\Delta f = 10 \text{ kHz} - 100 \text{ kHz}$. It can be seen in Fig. 8 that the simulated envelope base impedance drops accordingly. The HBT has a large input impedance due to the ballasting network and therefore it is also expected that the envelope has a strong effect to the total IM3. However, in addition to the base ballasting the base bias network also shows large impedance at low Δf , which is caused by a 500 ohm series resistor parallel with large capacitors. The reason for a large series resistor in the base bias is to reduce the $V_{BEQ} - I_{CQ}$ sensitivity. However, this results in Δf -dependent base impedance as seen in Fig. 8 which, in addition, causes bias shift in the PA. At low Δf the bias R-LC network does filter the envelope signal causing it to be rectified again in the nonlinear base impedance and resulting in Δf -dependent bias shift. This phenomenon is interesting as all the IM3 contributions also change similarly, which indicates that the coefficients change and are thus Δf -dependent. Fortunately the spectral based fitting and detailed distortion analysis is calculated for each Δf and is thus capable of predicting such behaviour. It should be noted that by using the Volterra model with fixed coefficients, for example, such behaviour cannot be seen.

In the more detailed view of the distortion contributions it is shown in Paper VIII that the 2-dimensional I_C and Q_{BE} sources as well as Q_{BEP} are dominating the distortion. The input related odd- and even-degree terms are strong but in opposite phase causing cancellation.

7.6 Impedance optimization

The final step to verify the spectral based fitting technique and simplified Volterra analysis method is to apply the proposed technique in the amplifier design by optimizing the matching impedances. Since the spectral fitting and detailed analysis is implemented in the circuit simulator, it can easily be used as a first step analysis tool for finding optimal matching impedances. An example of such optimization is, in fact, shown in Paper VI for Freescale's MRF21030 device in which the output matching impedances at the 2nd harmonic band were optimized in order to affect $K_{20} \cdot V_{H2}$ so that it cancels $K_{30} \cdot V_{30}$. As a

optimization are presented in Fig. 38b). The simulation test bench is similar to the one shown in Appendix 2 but here the output matching network including the bias network is replaced by the measured S-parameters. It can be seen that the fundamental and IM3 tones match very well before the optimization. After the optimization the measured and simulated fundamental show a good match and the simulated IM3 reduction is only around 5 dB. However, the S-parameters before and after the optimization show a good match. As a result of the optimization the phase of $Z_{OUT}(f_{H2})$ seen by the device is shifted by almost 100 degrees close to a short circuit. However, due to the limitations of the tuner the edge of the Smith chart could not be reached. Altogether, these results are considered accurate enough to perform a detailed distortion analysis.

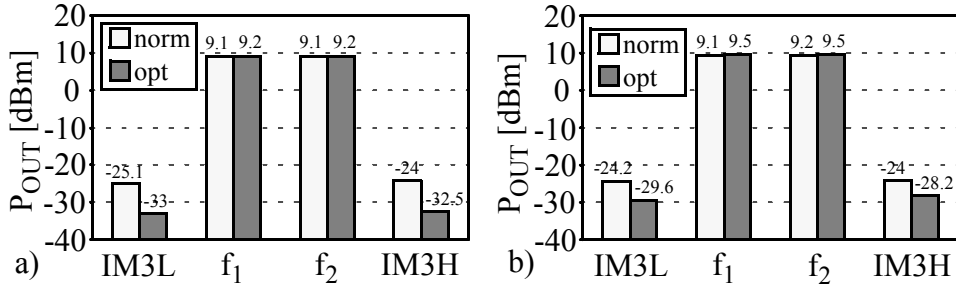


Fig. 38. a) Measured and b) simulated IM3 and fundamental tones before and after impedance optimization.

7.6.3 Detailed distortion analysis

In this section the impedance optimization is analysed using the detailed distortion analysis method. Since the optimization was performed in a single bias point, power level and tone spacing the phasor presentation before and after the tuning is presented. The insignificant contributions are not shown in this analysis.

The IM3 contributions of the total IM3 at the collector node of the VBIC model are presented in Fig. 39. The analysis of the IM3 before the optimization, presented in Fig. 39a) is the same as shown in Paper VIII. The only difference is that here the measured S-parameters of the output matching network are used in the simulations, which is why IM3 contributions are in different directions. However, the relations between the contributions are the same. In short, the IM3 caused by the I_C - V_{BE} - V_{BC} source ($V(I_C)$) is large and cancelled partly by the IM3 caused by the Q_{BE} - V_{BE} - V_{BC} source ($V(Q_{BE})$). The feedback capacitance $V(Q_{BEP})$ has a surprisingly large effect at the selected bias, input power and tone spacing and, in fact, dominates the IM3 with $V(I_C)$.

As a result of the optimization presented in Fig. 39b) a small phase shift can be seen but the relations between the contributions are still almost the same. The magnitudes of the contributions are decreased, which, however, is not the only reason for the total IM3 reduction. In fact, the $V(Q_{BE})$ is relatively larger now and thus causes more cancellation. The total IM3 is still dominated by $V(I_C)$ and $V(Q_{BEP})$ but the total IM3 is now almost 5 dB smaller.

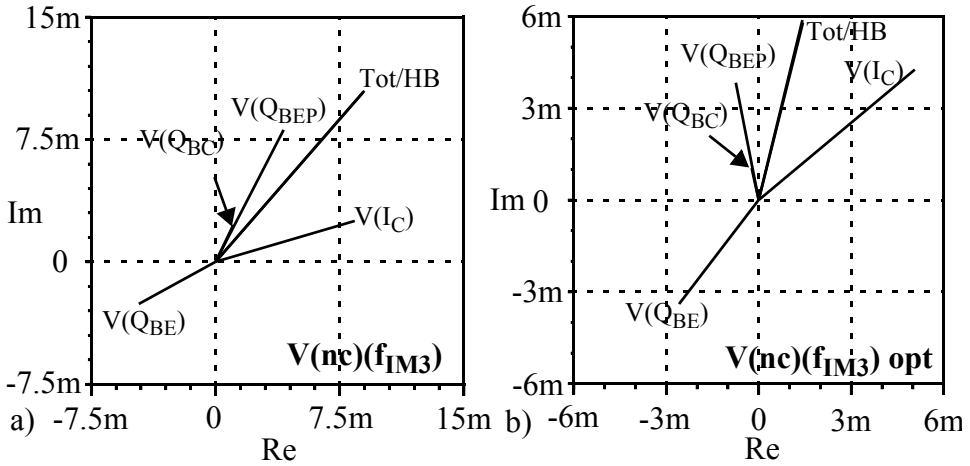


Fig. 39. IM3 contributions of the total IM3 at the collector node before and after the impedance optimization.

A more detailed view of IM3 contributions is shown in Fig. 40 in which the phasor presentation of the most dominant nonlinear sources I_C - V_{BE} - V_{BC} , Q_{BE} - V_{BE} - V_{BC} and Q_{BEP} - V_{BEP} are presented before and after the impedance optimization. Again, the analysis before the optimization is the same as shown in Paper VIII. Cubic nonlinearity $V(K_{30} \cdot V_{30})$ dominates the IM3 in each nonlinear source and it is cancelled by the even-order nonlinear terms, mainly $V(K_{20} \cdot V_{H2})$, that is mixed down to IM3 from the 2nd harmonic band. However, $V(K_{20} \cdot V_{H2})$ is not directly at the opposite phase to $V(K_{30} \cdot V_{30})$ in any of the presented nonlinear sources. Therefore more cancellation could be obtained by fine-tuning the 2nd harmonic impedance.

The vector plot after the optimization of the $V(I_C)$ source at the collector node is shown in Fig. 40b). It can be seen that $V(K_{20} \cdot V_{H2})$ is shifted exactly to the opposite phase to $V(K_{30} \cdot V_{30})$ and now all the contributions are either in the same phase or in the opposite phase. It is interesting to note that the magnitude of $V(K_{30} \cdot V_{30})$ is increased while the magnitude of $V(K_{20} \cdot V_{H2})$ is almost the same. However, $V(K_{40} \cdot V_{40})$ is increased as well and is in the opposite phase of $V(K_{30} \cdot V_{30})$. As a result the total IM3 of $V(I_C)$ is controlled by $V(K_{20} \cdot V_{H2})$ and $V(K_{40} \cdot V_{40})$ that cancel the IM3 caused by $V(K_{30} \cdot V_{30})$, resulting in a small total IM3.

The situation in $V(Q_{BE})$ shown in Fig. 40c) and d) before and after the optimization is similar to $V(I_C)$ since the same controlling voltages are controlling both sources. It can be noted again that the magnitude of $V(K_{30} \cdot V_{30})$ is increased, but since even-order terms $V(K_{20} \cdot V_{H2})$ and $V(K_{40} \cdot V_{40})$ are exactly in the opposite phase, they cancel $V(K_{30} \cdot V_{30})$ and dominate the IM3 of the source. In fact, the IM3 caused by $V(I_C)$ and $V(Q_{BE})$ could be further decreased by increasing $V(K_{30} \cdot V_{30})$ or by decreasing even-order terms.

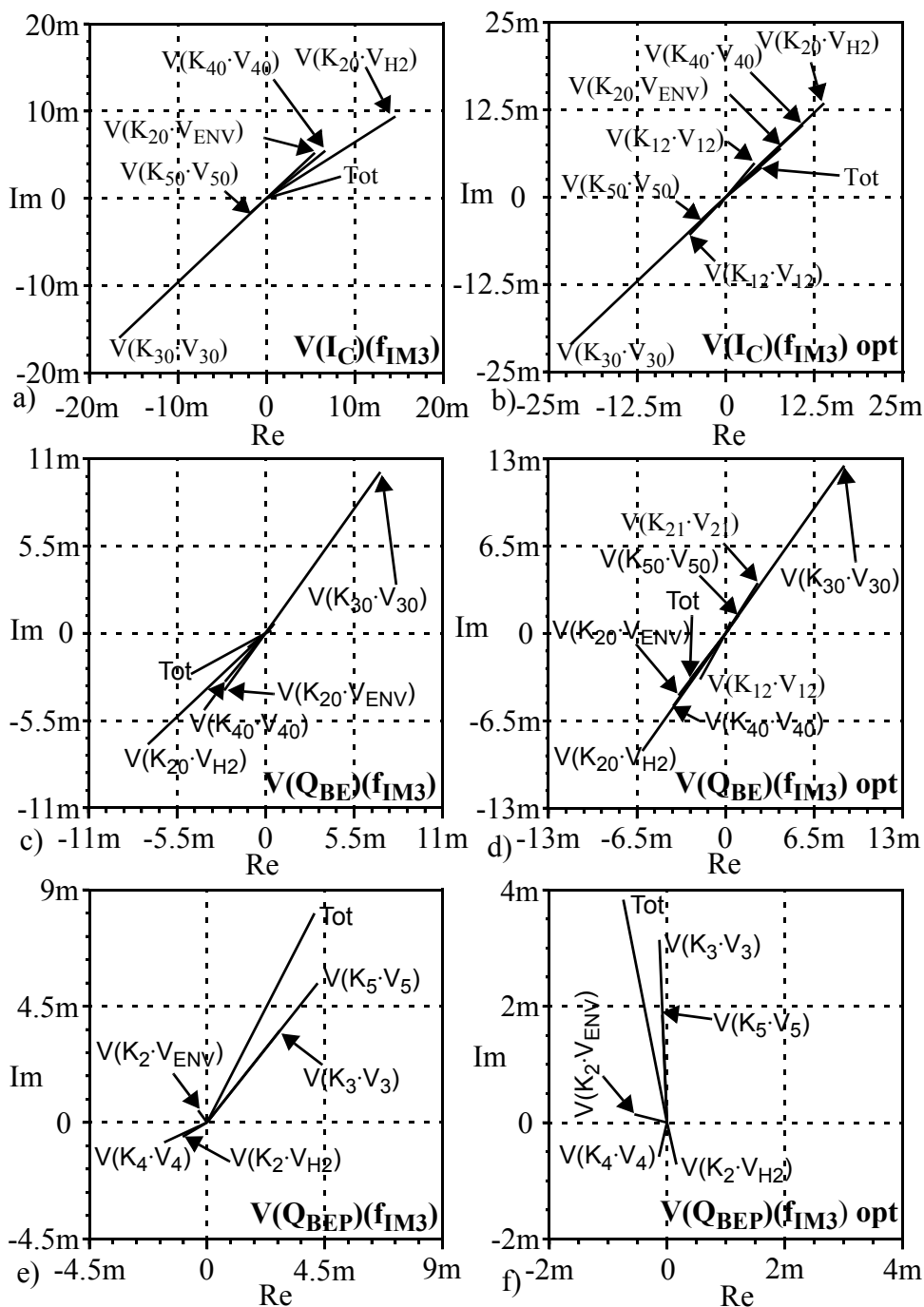


Fig. 40. IM3 contributions of a) & b) $V(I_C)$, c) & d) $V(Q_{BE})$ and e) & f) $V(Q_{BEP})$ at the collector node before and after the impedance optimization.

The detailed analysis of $V(Q_{\text{BEP}})$ presented in Fig. 40e) and f) before and after the optimization is different from $V(I_C)$ and $V(Q_{\text{BE}})$. Before the optimization the surprisingly large 5th-degree nonlinear term $V(K_5 \cdot V_5)$ is dominating the IM3 of $V(Q_{\text{BEP}})$. $V(K_{30} \cdot V_{30})$ is in the same direction as $V(K_5 \cdot V_5)$ but the magnitude is one third of $V(K_5 \cdot V_5)$. Even-order terms are small and thus by phase shifting $V(K_{20} \cdot V_{H2})$ strong cancellation cannot be achieved. As a result of the optimization the magnitudes of the contributions have decreased and thus the total IM3 is smaller. However, it is interesting to note that due to the impedance optimization $V(K_5 \cdot V_5)$ is no longer the largest IM3 contribution of the source but instead $V(K_3 \cdot V_3)$ is now the largest and thus controlling the total IM3 of the source.

8 Discussion

8.1 Building a frequency domain polynomial model

The objective of this work was to find out the componentwise information of the causes of distortion. Detailed analysis is possible using Volterra analysis, which relies on the polynomial models. However, polynomial models are not generally available, but can be easily fitted. The technique to fit the polynomial model presented in this thesis solves several problems of building a polynomial device model for detailed distortion analysis. First, the incapability of polynomial models of modelling only weak nonlinearities are circumvented by fitting a local model around the large-signal bias point and amplitude range. Second, the fitting is performed using the simulated large-signal spectra that automatically contain information about the large-signal bias point and amplitude range that are needed in local polynomial modelling. Third, since the frequency domain approach is used, delay and dispersion effects can be easily compensated. Fourth, in the frequency domain any distortion tone can be pinpointed and analysed in detail.

The main idea of the polynomial modelling in this thesis is to fit the polynomial model of each nonlinearity of the device model by using the simulated large-signal current and corresponding controlling voltage spectra of each nonlinear source. The higher-order voltage spectra needed for fitting are obtained simply by using convolution. The coefficients of the polynomial model are then fitted using the LSE method. The fitting becomes more difficult if nonlinearities are controlled by several voltages that additionally correlate strongly. In strongly nonlinear amplifiers this is usually not a problem, but in linear amplifiers the fitting may easily result in non-physical coefficients. The situation becomes even worse if self-heating effects are included to the fitted model. This is due to the fact that a simple thermal circuit shows almost nothing but DC temperature.

The fitting matrix becomes ill-conditioned if it contains two or more similar columns, which can be a result of at least two different causes. First, the fitting matrix becomes ill-conditioned if it contains significant and negligible data that are further combined. An example of such a case are the cross-terms in 2-dimensional g_m -element with strong input related and weak output related effects. Including negligible self-heating effects to the fitting matrix as discussed above also results in similar columns. Second, the strong input-

output correlation results in similar rows as the input related data is similar to the output related data. This becomes a problem especially in linear PAs.

A very thorough mathematical analysis of ill-conditioned fitting matrix has not been made. Nonetheless, the fitting matrix was made easily more solvable by amplitude and per-equation normalization. Chebychev polynomials or other type of orthogonal polynomials could also be used as suggested in Section 4.3.2. In fact, converting a normal 1-dimensional polynomial into a Chebychev polynomial is quite a simple task and reduces the condition number of the fitting matrix. However, conversion of the cross-terms of 2-dimensional nonlinearity into a Chebychev polynomial has not been considered yet. Altogether, the fact is that orthogonal polynomials can make the fitting matrix more easily solvable but cannot reduce the input-output correlation that is the main problem of the fitting. The easiest way to cope with correlated spectra is to reduce the degree of the model by removing insignificant or non-physical contributions. However, there is no guarantee that some of the removed terms actually have a significant effect to the total distortion. Therefore, different characterization setups need to be used. Instead of applying a normal 2-tone signal to the input, a 1-tone signal is applied in both input and output simultaneously. This breaks the correlation and makes the fitting matrix more solvable. Unfortunately, the power density function of the 1-tone input signal weights the peak amplitudes and is different from the 2-tone signal. Hence the input related terms can be fitted separately using a normal 2-tone input signal.

8.2 Componentwise analysis

The componentwise information is obtained in this thesis by using the fitted coefficients and the convolved spectra that are both available after the model is fitted. Distortion contributions can be calculated simply by multiplying the fitted coefficients with the corresponding convolved spectra. As a result the distortion can be presented as a sum of distortion contributions. Moreover, the mixing between frequency bands can be calculated. Especially the distortion that is mixed up and down to the fundamental band from envelope and 2nd harmonic band is under interest since those are the main causes of memory effects.

As a result, contributions of a distortion tone at the output of each nonlinear source is obtained. In order to analyse the effect of each nonlinearity to the total distortion in the terminal nodes (input and output of the device) the current contributions of the nearest sources can be summed at the terminal nodes if a simple device model was used. However, the effect of the input nonlinearities cannot be seen directly as they are lumped into the linear terms of the output nonlinearities. This calls for the linear transfer functions of the circuit that are used to calculate each distortion contribution in the input and the output, where the effect of each nonlinearity to the total distortion can be analysed in detail.

A large number of distortion contributions of the selected tone are obtained from the simplified Volterra calculations. Many of these are negligible, however, and therefore it is important to find the dominant distortion contributions easily. Hence the information needs to be compressed somehow. It is recommended that first the sum of the distortion tone of each nonlinear source is analysed at the selected terminal. The sum of these contributions is, in fact, the total distortion of the device. Then, the most dominant nonlinear sources can be analysed individually in detail.

The most illustrative way of presenting the contributions is to plot them as phasors as it enables the cancelling effects to be visualised. The real and imaginary axes need to be equally long as unequal scale easily gives a wrong view of the directions and magnitudes of the vectors. The smallest contributions should not be plotted as they only make the analysis more difficult. In addition, this presentation becomes too messy if parameter sweep is performed. In such a case it is more illustrative to show magnitudes and phases individually as a function of the sweeping variable. Then the most interesting points can be analysed using the phasor presentation as shown in this thesis. The phases of the input signals should also be shifted to zero at the input of the device before the analysis especially in the parameter sweep. This disables unwanted variation of the input signal and gives us a more illustrative view of the phase shift of the device.

8.3 APLAC implementation

The proposed technique is implemented in an APLAC circuit simulator with about 2000 lines of code using only APLAC's command language. The implementation has been made to be suitable and flexible for different simulations as shown in this thesis. However, the simulation time is rather short bearing in mind the quite extensive SpecFit procedures.

The comparison of the simulation time of different simulations is shown in Table 5. Normal HB simulation is compared with two different SpecFit simulations. In one SpecFit simulation a normal 2-tone input signal (Setup 1) is applied while in the other first a 1-tone input - 1-tone output setup is applied (Setup 2) for a more reliable fitting and then Setup 1 is used for fitting the Q-V nonlinearities and the input related terms of a 2-dimensional g_m . The simulations are performed using IBM ThinkPad T42 with 1.8 GHz Pentium M processor and one gigabyte of memory. In the parameter sweep simulations 20 simulation steps are used, in each of which the polynomial models are fitted and distortion contributions are calculated. The analysis is performed using the test bench of LDMOS PA.

Table 5. Comparison of the simulation times between HB and Spectral based fitting.

Simulation	HB	SpecFit: Setup 1	SpecFit: Setup 2 & 1
Steady state	7.25 s	9.74 s	12.24 s
Amplitude sweep	21.30 s	73s	119 s
I_{DQ} sweep	20.63 s	59.49 s	94 s
Δf sweep	20.07 s	59.17 s	91 s

It can be seen from Table 5 that steady state HB simulation is not more than 2.5 s faster than SpecFit simulation using Setup 1. The combined Setup 2 & 1 takes another 2.5 seconds. In amplitude, I_{DQ} and Δf sweep analysis the simulation times in different techniques are somewhat the same. However, the simulation times using SpecFit simulations are not as long as the steady state simulation would predict. The simulation time could easily be reduced by optimizing and removing all the extra calculations and operations as well as by reorganizing the SpecFit procedure.

8.4 Results of the test cases

The main restriction of the technique is that it relies on the existing device models. As it is shown, the access of the simulation models is not a problem, and the difficulty lies in verifying the results from the detailed distortion analysis instead. This is due to the fact that the corresponding data used for building a polynomial device model cannot be measured from real devices. This also means that the accuracy of the fitted model can only be as accurate as the particular simulation model. However, as the simulation models improve, more accurate and truthful results are obtained.

In this thesis two different simulation models, MET and VBIC models were studied. A simple structured MET model is used for modelling linear class AB RF power amplifiers. The difficulty in fitting a reliable polynomial model using the simulated data from the MET model is the strong input-output correlation in the 2-dimensional g_m . HBT PA modelled using the VBIC model shows stronger nonlinearities, which results in easier fitting. In fact, despite the VBIC model has multi-dimensional charge and current sources, the controlling voltages do not correlate strongly. The difficulty in the VBIC model is in the detailed analysis as it is rather complex and needs linear transfer functions in order to analyse the total distortion. Also the characteristics of the 2-dimensional $Q_{BE}-V_{BE}-V_{BC}$ source of the VBIC model is interesting mainly due to the surprisingly large output related effects that caused a great deal of confusion. The delays in 2-dimensional g_m -elements of both MET and VBIC models are implemented differently. In the MET model the input voltage was delayed while in the VBIC model the output current is delayed. Self-heating effects in both models are almost negligible and cannot show any thermal based distortion due to the Z_{TH} that contains only one and large time constant. Thermal models are often tricky since they might result in convergence problems as the temperature could explode towards infinity. For this reason, for example, a temperature limiter is implemented in the MET model. Hence, the thermal effects need to be considered more carefully in the future.

Since the detailed distortion analysis cannot be verified with real measurements, the total distortion was measured and compared with the corresponding simulated results. It was shown that the simulations and measurements match well in general. However, for example, the measured AM-PM of LDMOS PA showed only modest match with the use of the MET model. This could be related to the insufficient modelling of the capacitor models in the MET model. This is suggested in [82], in which it is presented that the nonlinear $Q_{D_S}-V_{D_S}$ source is a function of V_{D_S} but also V_{G_S} . In fact, similar results were obtained for each Q-V source of the MET model by fitting the polynomial model of Q-V sources based on the measured data obtained from the manufacturer. Since accurate results could not be achieved by using a 1-dimensional polynomial model, a 2-dimensional polynomial model had to be used. In addition, it can be noted from Fig. 34 and Fig. 35 presented in Section 7.4 that the mismatch between simulated and measured AM-PM begins after the Q_{G_S} becomes dominant over I_{D_S} . Therefore, it is indeed possible that poor modelling of AM-PM is caused by insufficient Q-V models.

Despite some modelling incapacities simulation models provide a decent estimate of the real mechanisms of the causes of the distortion. The detailed analysis is able to give a lot of new information and reveal interesting phenomena.

8.5 Future work

In order to improve and further develop the spectral based fitting technique and simplified Volterra analysis for general use several matters need to be considered. First, the technique needs to be functional with any simulation model. The correct controlling voltages and output currents of each nonlinear source need to be located. Second, the reliability of the fitting results needs to be improved. As presented in this thesis, the fitting of the polynomial models can easily result in non-physical coefficients and still show accurate total results. Therefore, the use of input-output driven characterization setups are mandatory in highly linear devices. However, this could be too demanding for an average user. Third, the spectral based fitting technique and detailed distortion analysis technique need to be applied for different circuit topologies that contain several devices. Fourth, automatic calculation of the transfer functions is needed. These could be obtained, for example, by applying a test current to each node one at a time and measure the response in each of them. This method, however, could be difficult to implement. Altogether, there are a number of issues that need to be considered before the technique is suitable for general use but these issues can be solved in one way or the other.

Before adopting the proposed technique for general use it should be studied if it were possible to obtain the componentwise information directly from HB. In fact, the distortion mixing between frequency bands and different nodes are stored in the Jacobian matrix and so different contributions could be obtained directly from there. However, in circuit simulators the distortion is usually presented as a sum of all contributions and hence cannot be pinpointed. Nonetheless, it could be worthwhile to study the possibility of reimplementing the Jacobian matrix so that the detailed information could be obtained. At least the Jacobian matrix could be used for obtaining the linear transfer functions of the circuit.

The technique could be extended also by adopting it to cope with more realistic multitone signals. At least the tones need to be equally spaced for successful convolution. The main concern, however, are conceivable fitting problems due to the fact that many different IM and mixing products appear at the same tone, many of which happen to be the fundamental multitone. Therefore, the degree of the model is not enough to show reliably the componentwise information of such a large amount of different contributions. A considerable amount of terms needs to be added to the model, which on the other hand easily results in fitting difficulties. Moreover, if different input signals could be used, the effect of the power density function of the input signal needs careful consideration.

The applicability of using the proposed method in a real circuit design is unquestionably one of the main future tasks. The main aim of the technique for a circuit designer is the information how to reduce the distortion most effectively. The optimization test benches that can reveal efficient circuit level linearization schemes need to be built. The best verification method of the technique in this sense would be to exploit the information obtained from the detailed optimization in actual circuit designs.

In conclusion, the further development of the technique depends on the interest of the industry and simulator software developers. Thus far, the SpecFit technique will be further developed as a research tool based on the personal interest of the author.

9 Summary

The general objective of this work was to develop an analysis technique that can give componentwise information of the causes of the distortion. Volterra analysis is capable of giving such information but it relies on the polynomial models. In this thesis a frequency domain polynomial model fitting technique was introduced in which each nonlinear source of the existing device model is fitted based on the simulated large-signal output current spectra and the corresponding controlling voltage spectra of each nonlinear source. The higher-degree voltage spectra needed for fitting are obtained by using convolution, which is a simple matrix multiplication.

The use of large-signal spectra provides a couple of advantages. First, the large-signal data contains the information about the large-signal bias point and the correct amplitude range that are needed in local polynomial modelling. Second, an accurate estimate of the fitted spectrum, i.e. distortion tones, are obtained instead of imitating a shape of the I-V curve, for example. Third, in the frequency domain it is much easier to compensate delay and dispersion effects. Fourth, the detailed distortion analysis can be applied to any tone of the fitted spectrum.

Fitting of the polynomial model of 1- and 2-dimensional nonlinear sources was presented, of which the fitting of the latter is difficult if the controlling voltages correlate strongly. This was the case especially with the MET model. The correlation was reduced by applying a 1-tone signal to the input and another tone to the output instead of a normal 2-tone input signal. The solvability of the fitting matrix was further improved by numerical operations and by reducing the degree of the model.

The distortion contributions were calculated by using the fitted coefficients and the corresponding convolved voltage spectra. In simple models such as the MET model the total distortion could be analysed by summing the distortion contributions of the nearest sources of the output. Using this approach the effect of input nonlinearities was not seen directly. Such an approach was not applicable in a complex structured VBIC model. Therefore, all the distortion contributions of each nonlinear source were further calculated as voltages to the terminal nodes by the use of the linear transfer functions of the circuit.

Since large-signal spectra from the intrinsic nodes and branches cannot be measured in practice, the data used for fitting was simulated from the existing device model. In the

APLAC circuit simulator it was possible to access the internal model. Therefore the proposed technique was implemented in APLAC on top of HB simulation with around 2000 lines of code using only the APLAC's command language without touching the source code. The spectral based fitting and detailed analysis technique is calculated in each simulation step and takes only about 2 seconds in each step on top of HB. This approach enables flexible simulations to be performed. Since the technique relies on the available device model, the obtained results are only as accurate as the particular simulation model.

In order to verify the technique, two different test benches were used in which nonlinear behaviour was analysed in detail. One is based on the 30 W LDMOS RF PA that was modelled using Freescale's MET model and the other on the 1 W HBT RF PA that was modelled using the VBIC model. Using these test benches in APLAC several test cases were carried out including AM-AM and AM-PM, IMD sweet spots, bandwidth dependent memory effects and impedance optimization. The detailed results could not be verified with the measurement but instead the total distortion was measured and compared with the simulations, which showed a sufficient match indicating that the obtained detailed results were reliable.

The analysis of the LDMOS PA showed that the IMD sweet spot was the result of the bias dependent g_m that was further cancelled by gate-source capacitance C_{GS} . The bias dependency in the g_m of the MET model was caused by the strong cancellation between 3rd-degree term and 2nd-degree term and 3rd-degree cross-terms. 2nd-degree nonlinear term is caused by the 2nd-degree nonlinearity and is mixed down to IM3 from the second harmonic band, and thus depends on the frequency dependent second harmonic impedance. Due to the strong cancellation the IMD sweet spot is very sensitive to parameter variations. In addition, as the distortion mixed down to IM3 from the 2nd harmonic is large, IM3 can easily be affected by tuning the 2nd harmonic impedance.

AM-AM and AM-PM of the corresponding LDMOS PA were also analysed. This analysis was performed for the fundamental tone. The distortion at the fundamental tone appeared to have an interesting sweet spot that was caused by the cancellation between g_m and C_{GS} . However, the distortion at the selected bias was so small that it had quite a small impact on the total fundamental tone. The AM-PM was mainly caused by the C_{GS} , but its effect was compensated by the g_m , whose phase showed to be strongly amplitude dependent. The phase shift in g_m was partly caused by the AM-PM of the 2nd harmonic via the 2nd-degree terms that was mixed down to IM3 from the 2nd harmonic band.

The detailed analysis of bandwidth dependent memory effects of HBT PA showed an interesting bandwidth dependent bias shift, which caused low gain and large distortion at low tone spacing. This was caused by the large time constant in the bias network that could not filter the envelope signal. The signal was thus rectified and caused a bias shift that appeared to be a strong function of tone spacing. Since bias changes, coefficients change as well. It was possible to observe this phenomenon as the spectral based fitting and detailed distortion analysis is calculated in each step.

Finally, the practical impedance optimization of the HBT PA was performed using a manual stub tuner. Detailed analysis of the optimization showed that by optimizing the 2nd harmonic impedance the 2nd-degree nonlinear term mixed down to IM3 from the 2nd harmonic was shifted to the opposite direction to the dominating 3rd-degree nonlinear term and so resulted in better cancellation.

References

1. Wireless Intelligent [ONLINE]. Available: <https://www.wirelessintelligence.com/index.aspx>
2. 3rd generation partnership project, 3GPP [ONLINE]. Available: <http://www.3gpp.org/>
3. 3rd generation partnership project, 3GPP [ONLINE]. Available: <http://www.3gpp.org/Highlights/LTE/LTE.htm>
4. Wang F, Yang AH, Kimball DF, Larson LE & Asbeck PM (2005) Design of wide-bandwidth envelope-tracking power amplifiers for OFDM applications. *IEEE Transaction on Microwave Theory and Techniques*, 53(4): 1244-1255.
5. Kimball D, Jeong J, Hsia C, Draxler P, Lanfranco S, Nagy W, Linthicum K, Larson L & Asbeck P. (2006) High-Efficiency Envelope-Tracking W-CDMA Base-Station Amplifier Using GaN HFETs. *IEEE Transactions on Microwave Theory and Techniques*, 54(11): 3848-3856.
6. Wang F, Kimball DF, Popp JD, Yang AH, Lie DY, Asbeck PM & Larson LE. (2006) An Improved Power-Added Efficiency 19-dBm Hybrid Envelope Elimination and Restoration Power Amplifier for 802.11g WLAN Applications. *IEEE Transactions on Microwave Theory and Techniques*, 54(12): 4086-4099.
7. Milosevic D, van der Tang J & van Roermund A (2003) On the feasibility of application of class E RF power amplifiers in UMTS. *IEEE MTT-S International Microwave Symposium Digest*, 149-152.
8. Maas S (1988) *Nonlinear microwave circuits*. Artech House.
9. Gripps S (1999) *RF power amplifiers for wireless communications*. Artech House.
10. Kennington PB (2000) *High-linearity RF amplifier design*. Artech House.
11. Vuolevi J & Rahkonen T (2003) *Distortion in power amplifiers*. Artech House.
12. Pedro JC & Carvalho NB (2003) *Intermodulation distortion in microwave and wireless circuits*. Artech House.
13. Jardon AH & Vazquez LH (1995) A novel representation of AM-PM conversion. *IEEE International Symposium on Electromagnetic Compatibility*: 401-405.
14. Rahkonen T & Vuolevi J (1999) Memory effects in analog predistorting linearizing systems. In *proceedings of the Norchip conference*: 114-119.
15. Freescale. MRF21030 LDMOS power transistor data sheet, [ONLINE]. Available: www.freescale.com/files/rf_if/doc/data_sheet/MRF21030.pdf
16. O. Kursu O, Riikola M, Aikio JP & Rahkonen T (2007) Polynomial 2.1 GHz RF predistorter IC with envelope injection output. *Journal on Analog Integrated Circuits and Signal Processing*, 50(1): 113-20.
17. Pedro JC & Maas SA (2005) A comparative overview of microwave and wireless power-amplifier behavioral modeling approaches. *IEEE Transaction on Microwave Theory and Techniques*, 53(4): 1150-1163.

18. Pedro JC & Carvalho NB (2005) Inferring nonlinear distortion performance of power amplifiers subject to telecommunications signals from two-tone measurements. *IEEE MTT-S International Microwave Symposium Digest*: 817-820.
19. Altet J, Rubio A, Schaub E, Dilhaire S & Claeys W (2001) Thermal coupling in integrated circuits: applications to thermal testing. *IEEE Journal of Solid-State Circuits*, 36(1): 81-91.
20. Schurack E, Rupp W, Latzel T & Gottwald A (1992) Analysis and measurement of nonlinear effect in power amplifiers caused by thermal feedback. *IEEE International Symposium on Circuits and Systems*, 2: 758-761.
21. Zhu Y, Twynam JK, Yagura M, Hasegawa M, Hasegawa T, Eguchi Y, Yamada A, Suematsu E, Sakuno K, Sato H & Hashizume N (1998) Analytical model of electrical and thermal transients of self heating semiconductor devices. *IEEE Transaction on Microwave Theory and Techniques*, 46(12,2): 2258-2263.
22. Hopkins T & Tiziani R (1989) Transient thermal impedance considerations in power semiconductor applications. *Automotive Power Electronics*: 89-97.
23. Zweidinger DT, Lee SG & Fox RM (1993) Compact modeling of BJT self heating in SPICE. *IEEE Transaction on Computer Aided Design of Integrated Circuit and Systems*, 12(9): 1368-1375.
24. Le Gallou N, Nebus JM, Ngoya E & Buret H (2001) Analysis of low frequency memory and influence on solid state HPA intermodulation characteristics. *IEEE MTT-S International Microwave Symposium Digest*, 2: 979-982.
25. APLAC circuit simulator documentation [ONLINE]. Available: <http://www.aplac.com>
26. Ku H, McKinley MD & Kenney JS (2002) Quantifying memory effects in RF power amplifiers. *IEEE Transaction on Microwave Theory and Techniques*, 50(12): 2843-2849.
27. Williams DJ, Leckey J & Tasker PJ (2002) A study of the effects of envelope impedance on intermodulation asymmetry using two-tone time domain measurement system. *IEEE MTT-S International Microwave Symposium Digest*, 3: 1841-1844.
28. Dunsmore J & Goldberg D (2003) Novel two-tone intermodulation phase measurement for evaluating amplifier memory effects. *33rd European Microwave Conference Digest*: 235-238.
29. Martins JP, Cabral PM, Borges Carvalho N & Pedro JC (2006) A Metric for the Quantification of Memory Effects in Power Amplifiers *Microwave*. *IEEE Transactions on Theory and Techniques*, 54(12): 4432-4439.
30. SPICE circuit simulator [ONLINE]. Available: <http://bwrc.eecs.berkeley.edu/Classes/IcBook/SPICE/>
31. Kundert K. & Sangiovanni-Vincentelli A. (1986) Simulation of nonlinear circuits in the frequency domain. *IEEE Transactions on Computer-Aided Design of Integrated Circuits and Systems*, 5(4): 521-535.
32. Kundert KS, White JK & Sangiovanni-Vincentelli A (1990) *Steady-state methods for Simulating analog and microwave circuits*. Kluwer Academic Publishers.
33. Rodrigues PJC (1998) *Computer-aided analysis of nonlinear microwave circuits*. Artech House.
34. Rizzoli V, Cecchetti C, Lipparini A & Matri F (1988) General-purpose harmonic balance analysis of nonlinear microwave circuits under multitone excitation. *IEEE Transaction on Microwave Theory and Techniques*, 36(12): 1650-1660.
35. Ngoya E & Larchevêque R (1996) Envelope transient analysis: A new method for the transient and steady state analysis of microwave communications circuits and systems. *IEEE MTT-S International Microwave Symposium Digest*: 1365-1368.
36. Roychowdhury J (2001) Analysing circuits with widely separated time scales using numerical PDE methods. *IEEE Transaction on Circuit and Systems - I: Fundamental theory and applications*, 48(5): 578-594.
37. Pedro JC & Carvalho NB (2002) Simulation of RF circuits driven by modulated signals without bandwidth constraints. *IEEE MTT-S International Microwave Symposium Digest*: 2173-2176
38. Condon M & Sautbegovic E (2003) A novel envelope simulation technique for high-frequency nonlinear circuits. *33rd European Microwave Conference Digest*: 619-622.
39. Carvalho NB, Pedro JC, Jang W & Steer MB (2006) Nonlinear RF circuits and system simulation when driven by several modulated signals. *IEEE Transaction on Microwave Theory and Techniques*, 54(2): 572-579.

40. Agilent Advanced Design System (ADS) [ONLINE]. Available: http://eesof.tm.agilent.com/products/ads_main.html
41. Mentor Graphics's Eldo RF [ONLINE]. Available: http://www.mentor.com/products/ic_nanometer_design/simulation/eldo_rf/index.cfm
42. Chang CR & Steer MB (1990) Frequency-domain nonlinear microwave circuit simulation using the arithmetic operator method. *IEEE Transaction on Microwave Theory and Techniques*, 38(8): 1139-1143.
43. Carvalho NB & Pedro JC (1998) Multi-tone frequency domain simulation of nonlinear circuits in large and small signal regimes. *IEEE Transaction on Microwave Theory and Techniques*, 46(12): 2016-2024.
44. Närhi T (1996) Frequency-domain analysis of strongly nonlinear circuits using a consistent large-signal model. *IEEE Transaction on Microwave Theory and Techniques*, 44(2): 182-192.
45. Narayanan S (1970) Application of Volterra series to intermodulation distortion analysis of transistor feedback amplifiers. *IEEE Transactions on Circuit Theory*, 17(4): 518-527.
46. Schetzen M (1980) *The Volterra and Wiener theories of nonlinear systems*. John Wiley & Sons.
47. Wambacq P & Sansen WMC (1998) *Distortion Analysis of Analog Integrated Circuits*. Kluwer Academic Publisher.
48. Peng L & Pileggi LT (2003) Efficient per-nonlinearity distortion analysis for analog and RF circuit. *IEEE Transaction on Computer Aided Design*, 22(10): 1297-1309.
49. Heiskanen A. & Rahkonen T. (2002) 5th order multi-tone Volterra simulator with component-level output. *IEEE International Symposium on Circuits and Systems, ISCAS 2002*. 3: 591-594.
50. Carvalho NB & Pedro JC (2002) A comprehensive explanation of distortion side band asymmetries. *IEEE Transaction on Microwave Theory and Techniques*, 50(9): 2090 - 2101.
51. Gaddi R (2002) *On the characterization and modelling of silicon RF LDMOS transistors*. Dissertation, University of Wales, Cardiff.
52. Philips MOS models [ONLINE]. Available: http://www.semiconductors.philips.com/Philips_Models/mos_models/index.html
53. Cheng Y & Hu C (1999) *MOSFET modeling & BSIM3 user's guide*. Kluwer academic publishers.
54. MOSFET SPICE model BSIM [ONLINE]. Available: <http://www-device.eecs.berkeley.edu/~bsim3/>
55. De Graaf HC, Kloosterman WJ & Koolen MCAM (1989) Experience with the new compact MEXTRAM model for bipolar transistors. In *proceedings of 1989 Bipolar Circuits and Technology Meeting*, 246-249.
56. McAndrew CC, Seitchik JA, Bowers DF, Dunn M, Foisy M, Getreu I, McSwain M, Moinian S, Parker J, Toulston DJ, Schroter M, van Wijnen P & Wagner LF (1996) VBIC95, the vertical bipolar inter-company model. *IEEE Journal of Solid-State Circuits*, 31(10): 1476-1483.
57. Curtice WR, Pla JA, Bridges D, Liang T & Shumate EE (1999) A new dynamic electro-thermal nonlinear model for silicon RF LDMOS FETs. *IEEE MTT-S International Microwave Symposium Digest*, 2: 419-422.
58. L. Råde & B. Westergren (1990) *Beta: mathematics handbook*. Bromley, U.K, Chartwell-Bratt.
59. Fager C, Pedro JC, Carvalho NB, Zirath H, Fortes F & Rosario MJ (2004) A comprehensive analysis of IMD behaviour in RF CMOS power amplifiers. *IEEE Journal of Solid-State Circuits*, 39(1): 24-34.
60. Press WH, Flannery BP, Teukolsky SA, Vetterling WT (1993) *Numerical recipes in C*. Cambridge University Press, 2nd edition.
61. Rust BW (2001) Fitting nature's basic functions part I: polynomials and linear least squares. *IEEE Computational Science and Engineering*, 3(5): 84 -89.
62. Chi C (1996) Discrete-sample curve fitting using chebyshev polynomials and the approximate determination of optimal trajectories via dynamic programming. *IEEE Transaction on Automatic Control*, 11(1): 116-118.
63. Raich R, Qian H & Zhou G (2004) Orthogonal polynomials for power amplifier modeling and predistorter design. *IEEE Transactions on Vehicular Technology*, 53(5): 1468-1479.

64. Maas S & Crosmun A (1989) Modelling the gate I/V characteristic of a GaAs MESFET for Volterra-series analysis. *IEEE Transaction on Microwave Theory and Techniques*, 37(7): 1134-1136.
65. Pedro JC & Perez J (1994) Accurate simulations of GaAs MESFET's intermodulation distortion using new drain-source current model. *IEEE Transaction on Microwave Theory and techniques*, 42(1): 25-33.
66. Kim Y, Yi J, Yang Y, B. Kim B (2001) A novel extraction method for higher order components of channel current in a GaAs MESFET. *Microwave and optical technology letters*, 29(2).
67. Garcia JA, Mediavilla A, Pedro JC, Carvalho NB, Tazón A, Garcia JL (1998) Characterizing the gate to source nonlinear capacitor role on GaAs FET IMD performance, *IEEE Transaction on Microwave Theory and Techniques*, 46(12): 2344-2355.
68. Rahkonen T, Aikio JP (2005) Methods for building polynomial device model for frequency domain nonlinear analysis. *Proceedings of the European Conference on Circuit Theory and Design (ECCTD'2005)*, Cork, Ireland, 29 Aug. - 2 Sep. 2005, 3: 353-356
69. MATLAB - Language of Technical computing [ONLINE]. Available: <http://www.mathworks.com/>
70. Schetzen M (1980) *The Volterra and Wiener theories on nonlinear systems*. New York: John Wiley and Sons.
71. Vuolevi J, Aikio JP, Rahkonen T (2002) Extraction of a polynomial LDMOS model for distortion simulations using small-signal S-parameters. *IEEE MTT-S International Microwave Symposium Digest*, 3: 2157-2160.
72. Heiskanen A, Aikio JP, Rahkonen T (2003) A 5th order Volterra study of a 30W LDMOS power amplifier. *Proceedings of the IEEE International Symposium of Circuit and Systems*, 4: 616-619.
73. Freescale, Austin, TX, MRF21030 LDMOS power transistor data sheet [ONLINE]. Available: http://www.freescale.com/files/rf_if/doc/data_sheet/MRF21030.pdf.
74. Global Communication Semiconductors, Inc. Power InCap HBT data sheet, [ONLINE], available: <http://www.gcsincorp.com/Technology/InGaPHBT.html>
75. Cherepko SV & Hwang JCM (2000) VBIC model applicability and extraction procedure for InGap/GaAs HBT. *IEEE International Asia-Pacific Microwave Conference Digest*, 2: 716-721.
76. Maas SA (2002) Ill conditioning in self-heating FET models. *IEEE Microwave and Wireless components letters*, (12)3, pp: 88-89.
77. Rudolph M (2004) Uniqueness problems in compact HBT models caused by thermal effects. *IEEE Transactions on Microwave Theory and Techniques*, (52)5: 1399-1403.
78. Carvalho NB & Pedro JC (1999) Large- and small-signal IMD behaviour of microwave power amplifiers. *IEEE Transaction on Microwave Theory and Techniques*, 47(12): 2364-2374.
79. Lee S, Jeon K, Lee Y, Lee K, Jeong Y (2003), The IMD sweet spots varied with gate bias voltage and input powers in RF LDMOS power amplifiers. *IEEE MTT-S International Microwave Symposium Digest*, 3: 1353-1356.
80. B. Toole B, Plett C, Cloutier M (2004) RF circuit implications of moderate inversion enhanced linear region in MOSFETs. *IEEE Transaction on circuit and systems I*, 51(2): 319-328.
81. Maury Microwave corporation, manual stub tuner [ONLINE]. Available: <http://www.maurymw.com/products/rfdfs/mantunrs/mntnrs3/mntnrs3.htm>.
82. Gaddi R, Pla JA, Benedict J & Tasker PJ (2001) LDMOS electro-thermal model validation from large-signal time-domain measurements. *IEEE MTT-S International Microwave Symposium Digest*, 1: 399-402.

Appendix 1

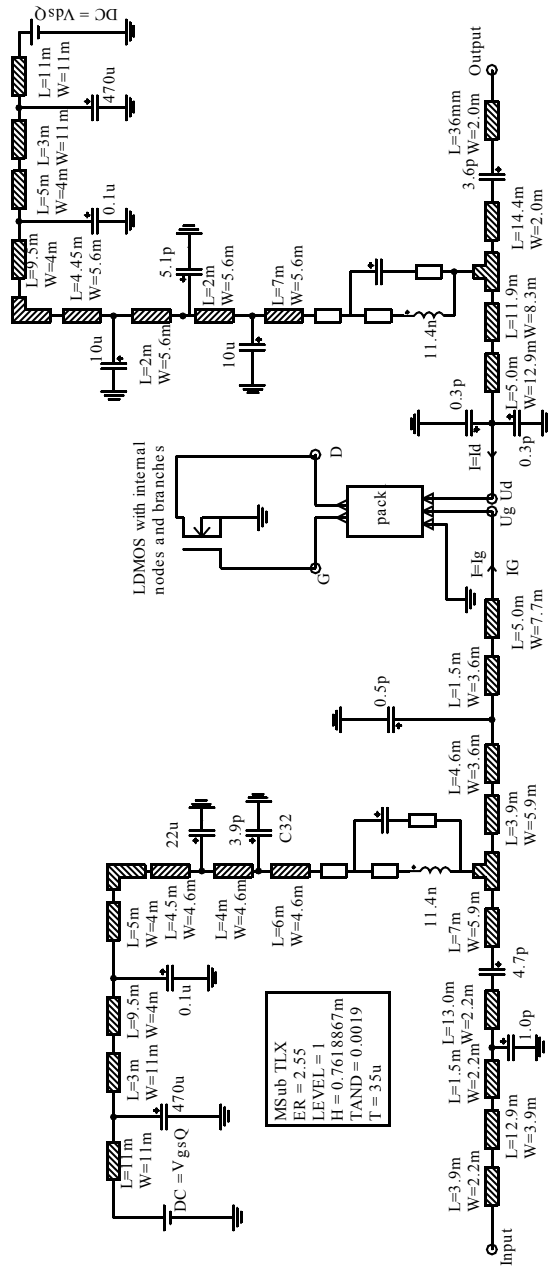


Fig. 41. Test bench for LD MOS PA based on Freescale's MRF21030 device modelled using MET model.

Original publications

- I Aikio JP, Rahkonen T (2003) The effect of fitting techniques on the accuracy of distortion simulations using polynomial device models. Proceedings of the European Conference on Circuit Theory and Design (ECCTD'03), Krakow, Poland, September 1-4, 2003, 3: 325-328. Copyright © 2003 AGH. Reprinted from ECCTD'03 conference Proceedings.
- II Aikio JP, Rahkonen T (2003), Fitting of polynomial device model based on large-signal voltage and current spectra. Proceedings of the 21st Norchip conference, Riga, Latvia, 10-11-Nov. 2003, 72-75. Copyright © 2003 Norchip conference. Reprinted from 21st Norchip conference Proceedings.
- III Aikio JP, Rahkonen T (2004), Fitting of 2-dimensional polynomial device model based on simulated voltage and current spectra. Proceedings of the International Symposium on Circuit and Systems (ISCAS'2004), Vancouver, Canada, 23-26 May 2004, 4: 645-648. Copyright © 2004 IEEE. Reprinted from ISCAS'2004 Conference Proceedings.
- IV Aikio JP, Rahkonen T (2004), Analysis method of nonlinear self-heating effects based on simulated large signal spectra. Proceedings of the 22nd Norchip conference, Oslo, Norway, 8-9 Nov. 2004, 91-94. Copyright © 2004 IEEE. Reprinted from 22nd Norchip conference proceedings.
- V Aikio JP, Rahkonen T (2005), Reliability of polynomial I_{DS} - V_{GS} - V_{DS} model fitted using harmonic balance simulation. Proceedings of the European Conference on Circuit Theory and Design (ECCTD'2005), Cork, Ireland, 29 Aug. - 2 Sep. 2005, 3:89-92. Copyright © 2005 IEEE. Reprinted from ECCTD'2005 conference Proceedings.
- VI Aikio JP, Rahkonen T (2005) Detailed distortion analysis technique based on large-signal voltage and current spectra. IEEE Transaction on Microwave Theory and Techniques, 53(10): 3057-3066. Copyright © 2005 IEEE. Reprinted from IEEE Transaction on Microwave Theory and Techniques.

- VII Aikio JP, Rahkonen T (2005), Detailed Analysis of IMD in an LDMOS RF Power Amplifier. IEEE MTT-S International Microwave Symposium Digest (IMS'2005), Long Beach, USA, 12-17 June 2005, 967-970. Copyright © 2005 IEEE. Reprinted from IMS'2005 conference Digest.
- VIII Aikio JP, Vuolevi J & Rahkonen T (2006), Detailed analysis of IMD of HBT PA using VBIC model. Proceedings of the 1st European Microwave Integrated Circuits Conference, (EuMIC'2006), Manchester, UK, Sept. 2006, 445-448. Copyright © 2006 EuMA. Reprinted from EuMIC'2006 conference Proceedings.

Original publications are not included in the electrical version of the dissertation.

256. Alarousu, Erkki (2006) Low coherence interferometry and optical coherence tomography in paper measurements
257. Leppäkoski, Kimmo (2006) Utilisation of non-linear modelling methods in flue-gas oxygen-content control
258. Juutilainen, Ilmari (2006) Modelling of conditional variance and uncertainty using industrial process data
259. Sorvoja, Hannu (2006) Noninvasive blood pressure pulse detection and blood pressure determination
260. Pirinen, Pekka (2006) Effective capacity evaluation of advanced wideband CDMA and UWB radio networks
261. Huuhtanen, Mika (2006) Zeolite catalysts in the reduction of NO_x in lean automotive exhaust gas conditions. Behaviour of catalysts in activity, DRIFT and TPD studies
262. Rautiainen, Mika (2006) Content-based search and browsing in semantic multimedia retrieval
263. Häkkinen, Jonna (2006) Usability with context-aware mobile applications. Case studies and design guidelines
264. Jari Heikkilä ja Jouni Koiso-Kanttila (toim.) (2007) Patinoituu ja paranee—Moderni puukaupunki -tutkijakoulu 2003–2006
265. Suikki, Raija (2007) Changing business environment—effects of continuous innovations and disruptive technologies
266. Harri Haapasalo & Päivi Iskanius (Eds.) (2007) The 1st Nordic Innovation Research Conference—Finnkampen
267. Pikka, Vesa (2007) A Business Enabling Network. A case study of a high-tech network; its concepts, elements and actors
268. Noora Ervasti, Anna-Elina Pietikäinen, Eva Wiklund, Maarit Hiltunen ja Esa Vesmanen (2007) Yksilölliset toiveet asuntotuotannossa
269. Fabritius, Tapio (2007) Optical method for liquid sorption measurements in paper
270. Miao, Honglei (2007) Channel estimation and positioning for multiple antenna systems

Book orders:
OULU UNIVERSITY PRESS
P.O. Box 8200, FI-90014
University of Oulu, Finland

Distributed by
OULU UNIVERSITY LIBRARY
P.O. Box 7500, FI-90014
University of Oulu, Finland

S E R I E S E D I T O R S

A
SCIENTIAE RERUM NATURALIUM
Professor Mikko Siponen

B
HUMANIORA
Professor Harri Mantila

C
TECHNICA
Professor Juha Kostamovaara

D
MEDICA
Professor Olli Vuolteenaho

E
SCIENTIAE RERUM SOCIALIUM
Senior Assistant Timo Latomaa

E
SCRIPTA ACADEMICA
Communications Officer Elna Stjerna

G
OECONOMICA
Senior Lecturer Seppo Eriksson

EDITOR IN CHIEF
Professor Olli Vuolteenaho

EDITORIAL SECRETARY
Publications Editor Kirsti Nurkkala

ISBN 978-951-42-8419-9 (Paperback)

ISBN 978-951-42-8420-5 (PDF)

ISSN 0355-3213 (Print)

ISSN 1796-2226 (Online)

